University of Strathclyde

Department of Mechanical & Aerospace Engineering

Advances in an Open-Source Direct Simulation Monte Carlo Technique for Hypersonic Rarefied Gas Flows

Abdul Ossman Ahmad

A thesis presented in fulfilment of the requirements

for the degree of Doctor of Philosophy

2013

Declaration of author's rights

This thesis is the result of the author's original research. It has been composed by the author and has not been previously submitted for examination which has led to the award of a degree.

Abdul Ahmad

August 2013

Abstract

Hypersonic vehicles that travel through rarefied gas environments are very expensive to design through experimental methods. In the last few decades major work has been carried out in developing numerical methods to capture these types of flows to a certain degree of accuracy. This accuracy is increased using particle based numerical techniques as opposed to continuum computational fluid dynamics. However, one of the modern problems of particle based techniques is the high computational cost associated with it.

This thesis presents an enhanced open-source particle based technique to capture high speed rarefied gas flows. This particle based technique is called *dsmcFoam* and is based on the direct simulation Monte Carlo technique. As a result of the author's work *dsmcFoam* has become more efficient and accurate.

Benchmark studies of the standard *dsmcFoam* solver will be presented before introducing the main advances. The results of the benchmark investigations are compared with analytical solutions, other DSMC codes and experimental data available in the literature. And excellent agreement is found when good DSMC practice has been followed. The main advances of *dsmcFoam* discussed are a routine for selecting collision pairs called the transient adaptive sub-cell (TASC) method and a dynamic wall temperature model (DWTM). The DWTM relates the wall temperature to the heat flux. In addition, verification and validation studies are undertaken of the DWTM.

Furthermore, the widely used conventional 8 sub-cell method used to select possible collision pairs becomes very cumbersome to employ properly. This is because many mesh refinement stages are required in order to obtain accurate data. Instead of mesh refinement the TASC technique automatically employs more sub-cells, and these sub-cells are based on the number of particles in a cell.

Finally, parallel efficiency tests of *dsmcFoam* are presented in this thesis along with a new domain decomposition technique for parallel processing. This technique splits up the computational domain based on the number of particles, such that each processor has the same number of particles to work with.

Acknowledgements

Firstly, I thank God for everything.

I would like to thank my supervisors Tom Scanlon and Jason Reese for their constant support, guidance, knowledge and expertise throughout my doctorate and for their undergraduate lectures that sparked my interest in fluid dynamics. I would also like to thank Richard Brown and all of the researchers in the James Weir Fluids Laboratory and Centre for Future Air-Space Transportation Technology for many fruitful discussions.

I am grateful to the Faculty of Engineering (University of Strathclyde) for the financial support in the form of the scholarship that has funded me throughout my doctorate.

I would like to thank Iain Boyd for inviting me to spend some time with his research group at the University of Michigan (U.S.A.) and for his support in chapter 5 of this thesis. I would also like to thank Tom Scanlon, Anas Sarwar MP and Nicola Sturgeon MSP for making this visit possible.

I am grateful to ChongSin Gou and K.C. Tseng from the National Chiao Tung University (Taiwan) and National Space Organization (Taiwan), respectively for their support in chapter 4 of this thesis. And I am grateful to Shashi Aithal from Argonne National Laboratory (U.S.A.) for providing some of the results in section 2.3.4.

I would like to thank Ian Taylor, Yonghao Zhang and Andrew Grant for their

support and guidance during my teaching roles in the department of Mechanical and Aerospace Engineering (University of Strathclyde).

I am grateful to Richard Martin for providing support in high performance computers, Graham Macpherson for providing OpenFoam support, Matthew Borg for providing programming support and Aileen Petrie for resolving my reprographic issues.

Finally, I would like to thank my family who have supported me throughout my life.

Contents

List of Figures

List of Tables

Nomenclature

A	Area
Ar	Argon
C_A	Coefficient of axial force
C_D	Coefficient of drag force
C_f	Coefficient of friction
C_h	Coefficient of heat transfer
C_L	Coefficient of lift force
C_m	Coefficient of moment
C_N	Coefficient of normal force
C_p	Coefficient of pressure
c	Instantaneous molecular speed
$\mathbf{c}$	Instantaneous molecular velocity
$\mathbf{c}'$	Thermal speed of a molecule
$\mathbf{c}'$	Thermal velocity of a molecule
$< c' >$	Average speed of a molecule
c'_{mp}	Most probable speed of a molecule
c'_{rms}	Root mean square speed of a molecule
cg	Centre of gravity
cp	Centre of pressure
D_b	Body diameter

d	Molecular diameter
d_{eff}	Effective diameter of molecules
d_n	Expected distance to nearest neighbour
e_{int}	Specific energy of internal modes of a molecule
e_{tra}	Specific energy of translational motion of a molecule
F_{ext}	External force
F_{ij}	Force of molecule j imparted on molecule i
F_{rand}	Random fraction
F_{VSC}	Factor
f	Distribution function
g_{int}	Internal degrees of freedom
H	Hydrogen
He	Helium
h	Heat capacity
J	Collision integral
Kn	Knudsen number
k	Boltzmann constant
$< ke >$	Average kinetic energy of a molecule
k_t	Thermal conductivity
L	Characteristic length-scale of a system
L/D	Lift-to-drag ratio
l	Distance between two points
Ma	Mach number
m	Molecular mass
max	Maximum
min	Minimum

m_r	Reduced mass
N	Number
N_2	Nitrogen
$\dot{N}$	Number flux
N_{DSMC}^{avg}	Average number of DSMC particles
n	Number density
O	Atomic oxygen
O_2	Oxygen
R	Radius
Pr	Prandtl number
p	Scalar pressure
p_{tens}	Pressure tensor
q	Heat transfer
$\dot{q}$	Heat flux
q_{cov}	Change of variable
q_{vec}	Heat flux vector
R	Gas constant
r_{bb}^{cp}	Minimum corner-point of bound-box
r_i	Molecule's position
r_{pp}	Molecule's position
r_{vec}	Position vector
T	Temperature
T_{int}	Internal temperature
T_{ove}	Overall temperature
T_{tra}	Translational temperature
t	Time

t_s	Time-step
$\mathbf{U}$	Macroscopic stream velocity
U	Macroscopic stream speed
V	Volume
v_q	Quantum level
x, y, z	Direction/ axis
Z_{rot}	Rotational relaxation collision number
Z_{vib}	Vibrational relaxation collision number

Greek

Γ^{ψ}	Flux of a particle property
γ	Specific heat ratio
δ_{ij}^{K}	Kronecker delta
ϵ	Emissivity
ζ	Molecular speed-ratio
Θ_{dis}	Characteristic dissociation temperature
Θ_{vib}	Characteristic vibrational temperature
θ	Energy flux
θ_a	Azimuthal angle
θ_e	Elevation angle
θ_n	Angle between U_{inlet} and the boundary unit normal vector
λ	Mean free path
μ	Dynamic viscosity
ρ	Mass density
σ	Stefan-Boltzmann constant
σ_{ccs}	Collision cross-section
σ_{TA}	Thermal-accomodation coefficient
σ_{TMA}	Tangential-momentum-accomodation coefficient
τ	Shear stress
τ_{tens}	Viscous stress tensor
ε_{coll}	Collision energy
ε_{int}	Internal energy of a molecule
ε_{vib}	Vibrational energy of a molecule
ϕ	Mass flux

ψ	Particle property
$d\Omega_{csa}$	Differential collision solid angle
ω	Viscosity index

Superscripts

$*$	Post-collision
loc	Local
net	Net
sc	Sub-cell

Subscripts

0	Total condition
b	Back
bb	Bound-box
BLG	Body-length global
BLL	Body-length local
CTV	Collisions per unit time per unit volume
$cell$	Cell
$c-f$	Cell-face
$cofm$	Centre of mass
$coll$	Collisions
DS	Deep-space
es	Equilibrium state
f	Front
GLL	Gradient-length local
gas	Gas
inc	Incident
$inlet$	Inlet
loc	Local
max	Maximum
$molec$	Molecules
mp	Most probable
net	Net
pic	Particles in cell
$ppsc$	Particles per sub-cell
p,q	Different species

$_{RMDP}$	Real molecules to one DSMC particle
$_{r}$	Relative
$_{ref}$	Reference
$_{rfl}$	Reflected
$_{VHS}$	Variable hard sphere
$_{vib}$	Vibrational
$_{W}$	Wall
$_{\infty}$	Free-stream

Acronyms

$AGARD$	Advisory group for aerospace research and development
ANL	Argonne National Laboratory
$AS1$	Analytical solution 1
$AS2$	Analytical solution 2
$B.E.$	Boltzmann equation
CFD	Computational fluid dynamics
CPU	Central processing unit
DAC	DSMC analysis code
$DSMC$	Direct simulation Monte Carlo
$DWTM$	Dynamic wall temperature model
MD	Molecular Dynamics
MFS	Majorant frequency scheme
NTC	No-time-counter
$PDSC$	Parallel DSMC code
$PPSC$	Particles per sub-cell
RAM	Random-access memory
QK	Quantum-kinetic
SBT	Simplified Bernoulli trials
$SMILE$	Statistical modeling in low-density environment
$TASC$	Transient adaptive sub-cell
TCE	Total collision energy
VHS	Variable hard sphere

Chapter 1

Introduction

Hypersonic vehicles that travel through rarefied gas environments are very expensive to design through experimental methods, however in the last few decades major work has been carried out in developing numerical methods to capture these types of flows to a certain degree of accuracy. This accuracy is increased using particle based numerical techniques as opposed to continuum computational fluid dynamics (CFD) but one of the modern problems of this is the high computational cost associated with it. The key goal of the PhD research was to enhance an open-source particle based technique to capture such flows and as a result of the work this particle based technique, discussed in more detail in the following chapter and based on the direct simulation Monte Carlo (DSMC) method, has become more efficient and accurate.

Despite the high cost associated with the development of very high speed vehicles, the E.U. is funding a ten million Euro long-term advanced propulsion concepts and technologies (LAPCATII) project [6] to find an ecofriendly, hypersonic civilian vehicle. This has already generated three concept vehicles that are undergoing design trials. At altitudes of several tens of kilometres, and speeds in excess of Mach five, the dilute but high-enthalpy gas flow environment in which

these hypersonic vehicles manoeuvre requires simulation techniques, that capture the challenging physics of the bow shock, shock layer radiation, dissociation and ionization, heat generation, surface ablation and recession, flow separation and re-compression in both equilibrium and non-equilibrium gas conditions.

As part of this PhD studies have already been undertaken [7–9] to test the aerodynamic design of one of these aircraft: Skylon, designed by Reaction Engines Ltd, an Oxfordshire-based SME, to be an unpiloted re-usable space-plane powered by hydrogen fuelled, turbine-based combined-cycle engines. This research will impact Reaction Engines Ltd and the Skylon project directly, enhancing its competitiveness against the other designs. The multidisciplinary applications of non-equilibrium flows means this research may also impact the pharmaceutical, manufacturing, mechanical, chemical, environmental and electronics industries: designers, developers and manufacturers will benefit from an enhanced modelling and design capability, for example designing next-generation space systems and microsensors. Governmental and non-governmental agencies will also benefit from this work: for example, the Beagle 2 spacecraft crash [10] may have been avoided if a non-equilibrium aero-thermodynamic instability in its flight through the Martian atmosphere had been properly taken into account. In the longer term, the work contained in this thesis may be incorporated into simulation tools for industries concerned with non-equilibrium transport physics, including modern materials processing, chemical and environmental engineering.

This chapter provides the structure of the thesis and briefly describes the concepts of rarefied gas dynamics and the Boltzmann equation - widely used by the numerical methods found in the literature and is considered as the governing numerical equation of gas dynamics.

1.1 Thesis structure

This thesis presents an introduction to the DSMC method in Chapter two and outlines the main features of the open-source version of DSMC, called *dsmcFoam* which has been used for the investigations in this thesis. This chapter also briefly presents other DSMC codes available around the world. In addition, parallel efficiency studies are presented of this new DSMC code and they were carried out on high performance computers at the University of Strathclyde and Argonne National Laboratory (U.S.) [11]. Also, a new domain decomposition method is presented to increase the efficiency of parallel *dsmcFoam* simulations.

Benchmark studies of *dsmcFoam* are presented in chapter three. The results of the benchmark investigations are compared with analytical solutions, other DSMC codes and experimental data available in the literature.

Chapter four introduces a sub-routine for processing the collisions of particles in *dsmcFoam*. This sub-routine, called the transient adaptive sub-cell (TASC) routine, is used when *dsmcFoam* chooses possible particle collision pairs. The current widely used conventional method becomes very cumbersome to employ properly as a lot of mesh refinement stages are required in order to obtain accurate data. The technique employs more sub-cells instead of mesh refinement.

In most DSMC systems that involve hypersonic gas flows over surfaces the wall temperature is closely related to the heat flux. However, in practice the wall temperature is assumed to be isothermal and fixed to a value over the entire surface. This is not reasonable and is discussed in more detail in chapter five along with an alternative boundary condition called the dynamic wall temperature model (DWTM) which has been introduced into *dsmcFoam*. Verification and validation investigations of the boundary condition are also presented in that chapter.

Finally, in chapter six the research presented in this thesis will be summarised.

1.2 Rarefied gas dynamics

This section outlines the history and the background of kinetic theory and briefly describes the governing equation of gas flows. Also, the Knudsen number is described which is used to define the degree of rarefaction in a gas flow and as a result helps one choose the most appropriate numerical method for a particular system.

1.2.1 Brief history of rarefied gas dynamics

The kinetic approach to gas flows forms the basis of rarefied gas dynamics. Over one-hundred and fifty years ago it was thought that all molecules in a gas move around with the same speed [12], however, this theory was invalid and was superseded in 1859 when Maxwell [13] introduced a statistical approach to describe the gaseous medium, that is Maxwell first presented the velocity distribution function and delivered its interpretation in an equilibrium form. Approximately ten years later Boltzmann [14] determined the kinetic relation that describes the evolution of the distribution function for non-equilibrium systems [12].

In 1909 Knudsen [15] pioneered experiments in rarefied gas dynamics that initiated the development of a new technique based on the kinetic theory of gases to determine this gas phenomena analytically. When conducting experiments and in particular while measuring the flow rate through a tube at a low pressure, Knudsen observed a departure from the Poiseuille expression. This low pressure was not in the continuum regime and the deviation was present as the Poiseuille expression did not apply to non-continuum systems.

A couple of years after these experiments progress had increased by En-

skog [16], Hilbert [17] and Chapman [18] to analytically solve the Boltzmann equation by expanding the distribution function to account for the Knudsen number. However, this proved to be a challenge for the rarefied gas flow community and the findings from the expansion resulted in a complicated relationship between the transport coefficients and intermolecular potential.

Just under sixty years ago, the so-called model equations [19, 20] were introduced which drastically reduced the computational requirements in determining the phenomena in a rarefied gas. Within the next few years since the introduction of the model equations all classical problems of gas dynamics were solved using these equations. Some of these problems included Couette flow, Poiseuille flow, and heat transfer between two plates and these were determined over a wide range of gas rarefactions. The model equations even to this day are used to determine the flow phenomena of a gas, as solving the exact Boltzmann equation analytically is still a challenge for most modern supercomputers.

1.2.2 The kinetic theory

Here a brief history and background of kinetic theory is provided.

Brief history of the kinetic theory

The book *Hydrodynamica* published in 1738 by Daniel Bernoulli, a Swiss physicist and mathematician, developed the foundation of the kinetic theory of gases. This theory of gases describing a number of molecules travelling in all direction is widely used to this day for example the pressure felt on a surface is due to the gas molecules impinging on it and the heat experienced in air is due to the motion of the molecules. At the time the conservation of energy theory (elastic molecule collisions) was not prescribed, therefore the kinetic theory was

not initially accepted by other scientists.

In 1856 a simple gas-kinetic model [21] was introduced, but the molecules were limited to bearing a translational mode only. However, in the following year Clausius [22] had introduced a more advanced model that accounted for the rotational and vibrational modes too. In 1859 the first statistical law related to molecules [23] was presented by Maxwell, this introduced the Maxwell distribution of molecular velocities that indicated a quantity of molecules have a particular velocity in a specific range. Even at the time when these theories were formulated there was still a lot of scepticism that molecules were not physical but hypothetical objects [24]. But the turning point was in 1906 when two papers [25, 26] built on kinetic theory successfully convinced the scientific community of the existence of molecules and this was experimentally verified by Perrin in 1908 to 1923 [27, 28]. Furthermore, Maxwell's theory is now generalised and called the Maxwell-Boltzmann distribution and this is widely used in many modern applications involving rarefied gas flows.

Brief background of kinetic theory

The kinetic theory of gases uses a statistical representation of dilute systems by describing it as a large number of individual molecules that are in random motion and interacting with one another and bounding surfaces. It builds up the macroscopic phenomena from the dynamics of molecules, using probability theory, at a microscopic level. It is important to note that all collisions in kinetic theory are considered as binary as in a dilute gas three or more molecules in one collision is not considered likely [29]. Also, in a dilute system the average distance between molecules is larger than d_{eff}, the effective diameter of molecules, and

Garcia [30] describes this as

$$d_{eff} << \sqrt[3]{\frac{V}{N_{molec}}}, \tag{1.1}$$

in a volume, V, that contains a number of molecules, N_{molec}. As a result Boltzmann's molecular chaos assumption [31], that is the velocities and positions of particles colliding with each other are uncorrelated, is valid since a sufficient separation distance between molecules allow the inter-molecular potentials to be neglected.

Classical mechanics can accurately model the interactions of molecules in a dilute environment. By assuming the molecules interact with each other with a pairwise force relative to the distance that separates them, then the dynamics of molecules in a system can be described by an equation of motion:

$$\frac{d^2}{dt^2} r_i = \frac{1}{m} \sum_{\substack{j=1 \\ j \neq i}}^{N} F_{ij}, \tag{1.2}$$

where F_{ij} is the force of molecule j imparted on molecule i, t is the time-step and m is the mass of a molecule that has a position r_i. By evaluating these ordinary differential equations the future state of a system can be determined and this is the backbone of the *molecular dynamics* (MD) numerical method. MD has been a reliable tool for evaluating micro and nano systems [32, 33]. However, these types of simulations can be very expensive even on modern supercomputers. Garcia explains [30] for a gas simulation of a million molecules occupying a volume of 0.037 μm^3 takes a supercomputer an hour to evolve the system by a few nanoseconds of physical time. One microsecond of water flow [34] in a channel of dimensions 10×20×100 nm requires up to ten years using a modern computer.

The large number of molecules can be used as an advantage in statistical me-

chanics of dilute systems. The instantaneous state of any molecule in a system is ignored in statistical mechanics and probabilities are used and average quantities are computed. Therefore the very large number of molecules in a system are an advantage as the quantities can be averaged over a large sample. Furthermore, dilute systems usually assume that a molecule's energy is in fully kinetic form (ideal gas).

The probability of a molecule in a system with a random or thermal speed between c' and $c' + dc'$, $f(c')dc'$, is

$$f(c')dc' = 4\pi \left(\frac{m}{2\pi kT}\right)^{\frac{3}{2}} (c')^2 e^{-\frac{m(c')^2}{2kT}} dc', \tag{1.3}$$

where k and T represent the Boltzmann constant and temperature, respectively. This distribution is known as the Maxwell-Boltzmann distribution and various quantities can be determined from this. For example, the average speed of a molecule, $< c' >$, is determined as

$$< c' > = \int_0^\infty c' f(c')dc' = \frac{2\sqrt{2}}{\sqrt{\pi}} \sqrt{\frac{kT}{m}}, \tag{1.4}$$

and the root mean square speed, c'_{rms}, of a molecule as

$$c'_{rms} = \sqrt{< (c')^2 >} = \sqrt{\int_0^\infty (c')^2 f(c')dc'} = \sqrt{3}\sqrt{\frac{kT}{m}}. \tag{1.5}$$

Thus, the average kinetic energy, $< ke >$, of a molecule is

$$< ke > = < \frac{1}{2} m(c')^2 > = \frac{3}{2} kT, \tag{1.6}$$

and this satisfies the equipartition theorem [30], that is it relates the temperature of a system with the average energy. Finally, the speed at which $f(c')$ has a

maximum is termed the most probable speed, c'_{mp}, and is computed as

$$\left.\frac{d}{dc'}f(c')\right|_{c'=c'_{mp}} = 0 \tag{1.7}$$

$$\Rightarrow c'_{mps} = \sqrt{2}\sqrt{\frac{kT}{m}}. \tag{1.8}$$

These three velocities are indicated on the Maxwell-Boltzmann distribution, illustrated in figure 1.1, and based on the data of Garcia [30] for Nitrogen at a temperature of 273 K.

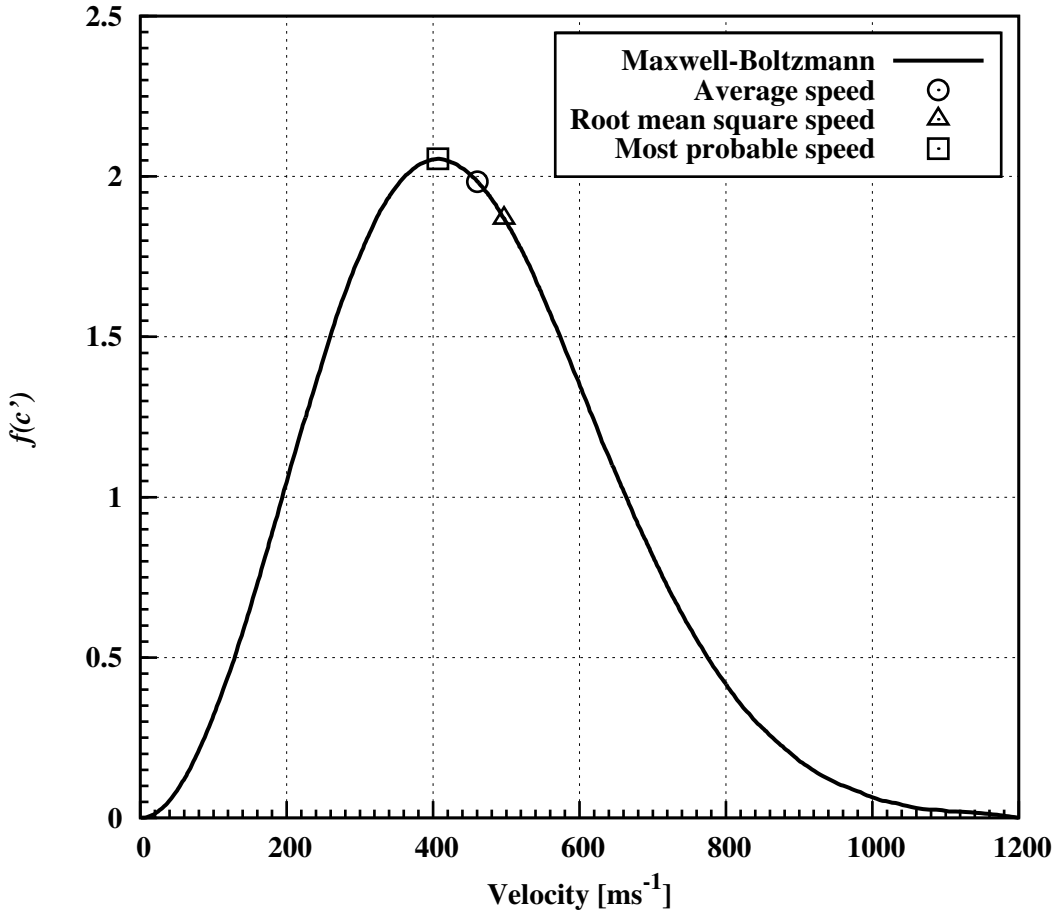

Figure 1.1: The Maxwell-Boltzmann distribution of molecular thermal speeds of Nitrogen at a temperature of 273 K. The average, root mean square and most probable speeds are marked on the graph.

Macroscopic properties are mostly used in designing real engineering applications therefore it is important to determine properties such as density and temperature from molecular information. The following will outline the method to determine the macroscopic properties and they apply for both equilibrium and non-equilibrium systems. For simplicity, they are restricted to a single species gas with energy in the translational and internal modes only. The most basic property to define is the number density, n, and is written as

$$n = \frac{N_{molec}}{V}. \tag{1.9}$$

Using the number density the mass density, ρ, is determined as

$$\rho = nm. \tag{1.10}$$

The other most common macroscopic properties of interest are based on the transport of mass, momentum and energy caused by the motion of the molecules. The thermal velocity, $\boldsymbol{c'}$, is the instantaneous velocity of a molecule relative to the macroscopic stream velocity, $\boldsymbol{U}$,

$$\mathbf{c'} = \mathbf{c} - \mathbf{U}, \tag{1.11}$$

where $\boldsymbol{U}$ is the mean value of the instantaneous molecular velocities, $\boldsymbol{c}$. By considering an element of gas from a reference frame moving with the local macroscopic stream velocity, the macroscopic properties of interest can be characterised as average values taken over the molecules' thermal velocities.

The pressure tensor, p_{tens}, has nine components [4] and in a simple form is written as

$$(p_{tens})_{ij} = \rho\overline{c_i' c_j'}, \tag{1.12}$$

where the subscripts i and j account for three values each and each value represents a component of the vector along the x, y and z directions and they are:

$$c'_1 = c'_x, \tag{1.13}$$

$$c'_2 = c'_y, \tag{1.14}$$

$$\text{and } \; c'_3 = c'_z. \tag{1.15}$$

The average of the three normal components of the pressure tensor defines the scalar pressure, p,

$$p = \frac{1}{3}\rho\left(\overline{(c'_x)^2} + \overline{(c'_y)^2} + \overline{(c'_z)^2}\right) = \frac{1}{3}\rho\overline{(c')^2}, \tag{1.16}$$

and if the gas is in equilibrium all three normal components are equal and the calculation simply becomes the product of the mass density and the mean of the square of any normal component of the thermal velocity.

The viscous stress tensor, τ_{tens}, is defined as

$$\tau_{tens} \equiv \tau_{ij} = -\left(\rho\overline{c'_i c'_j} - \delta^K_{ij}p\right), \tag{1.17}$$

where the Kronecker delta, δ^K_{ij}, has the conditions that if $i = j$ then $\delta^K_{ij} = 1$ or if $i \neq j$ then $\delta^K_{ij} = 0$.

The specific energy related to the translational motion, e_{tra}, of a molecule is

$$e_{tra} = \frac{1}{2}\overline{(c')^2}, \tag{1.18}$$

where the average kinetic energy related to the same motion is equal to the product of the same terms, on the right hand side of the above equation, and the

mass of a molecule. The above equation is combined with equation 1.16 to form,

$$p = \frac{2}{3}\rho e_{tra}, \tag{1.19}$$

and this can be equated to the ideal gas law,

$$p = \rho RT = nkT, \tag{1.20}$$

where R is the gas constant, to form,

$$\frac{3}{2}kT_{tra} = \frac{1}{2}m\overline{(c')^2} = \frac{1}{2}m\left(\overline{(c'_x)^2} + \overline{(c'_y)^2} + \overline{(c'_z)^2}\right) \tag{1.21}$$

$$\text{or} \quad \frac{3}{2}RT_{tra} = e_{tra} = \frac{1}{2}\overline{(c')^2}. \tag{1.22}$$

Even though the thermodynamic temperature is defined as an equilibrium gas property, the above relations suggest the equation of state applies to a dilute gas, whether it is in equilibrium or not, for the translational temperature T_{tra}. Also, this is the only temperature in a monatomic gas but diatomic and polyatomic molecules also have an internal energy that has rotational and/ or vibrational modes. The internal temperature, T_{int}, is defined as

$$\frac{1}{2}g_{int}RT_{int} = e_{int}, \tag{1.23}$$

where g_{int} and e_{int} represent the number of internal degrees of freedom and specific energy related to the internal modes, respectively. Also, this definition is consistent with the definition associated with the translational temperature in equation 1.22. Furthermore, the values of the translational and internal temperatures in an equilibrium system are equal and therefore either can be associated

with the thermodynamic temperature of the gas. However, for non-equilibrium systems an overall temperature, T_{ove}, may be used and is defined as the weighted average of the translational and internal modes:

$$T_{ove} = \frac{3T_{tra} + g_{int}T_{int}}{3 + g_{int}}, \tag{1.24}$$

where the number three represents the number of translational degrees of freedom. In addition, this temperature definition is not applicable to the ideal gas law in a non-equilibrium system [4].

Finally, the heat flux vector, q_{vec}, is calculated as

$$q_{vec} = \frac{1}{2}\rho\overline{(c')^2\mathbf{c'}} + n\overline{\varepsilon_{int}\mathbf{c'}}, \tag{1.25}$$

where ε_{int} is the internal energy of a molecule and is defined as

$$\overline{\varepsilon_{int}} = e_{int}m. \tag{1.26}$$

For clarity, the component of heat flux in the y-direction, q_y, is

$$q_y = \frac{1}{2}\rho\overline{(c')^2c'_y} + n\overline{\varepsilon_{int}c'_y}. \tag{1.27}$$

1.2.3 The Boltzmann equation

For gas flows, the Boltzmann equation describes the evolution in phase space of the velocity distribution function [35]. The phase space is a combination of physical and velocity space. The Boltzmann equation, for a single species and

monatomic gas, is written as [4]

$$\frac{\partial(nf(\mathbf{c}))}{\partial t} + \mathbf{c}\frac{\partial(nf(\mathbf{c}))}{\partial r_{vec}} + F_{ext}\frac{\partial(nf(\mathbf{c}))}{\partial \mathbf{c}} = J\left(f(\mathbf{c}), f^*(\mathbf{c})\right), \tag{1.28}$$

where t, r_{vec} and F_{ext} represent the time, position vector and external force, respectively. $J\left(f(\mathbf{c}), f^*(\mathbf{c})\right)$ is the collision integral that represents binary collisions and is defined as

$$J\left(f(\mathbf{c}), f^*(\mathbf{c})\right) = \int_{-\infty}^{\infty}\int_{0}^{4\pi} n^2\left(f^*(\mathbf{c})f^*(\mathbf{c_1}) - f(\mathbf{c})f(\mathbf{c_1})\right) c_r \sigma_{ccs} d\Omega_{csa} d\mathbf{c_1}, \tag{1.29}$$

where c_r, σ_{ccs} and $d\Omega_{csa}$ represent the relative speed of two colliding molecules, collision cross-section and differential collision solid angle. $\boldsymbol{c_1}$ represents the velocity of the other molecule of the collision pair.

The Boltzmann equation can be used to describe all flow regimes, on the assumptions that binary collisions and molecular chaos are met, however it is very expensive to solve numerically, even in the above form for dilute gases due to the non-linear behaviour of the collision integral.

1.2.4 The Knudsen number

The study of gases numerically is important for all conditions that nature provides, however it is important that the correct method for predicting a particular gas flow is chosen such that it produces accurate phenomena efficiently. The most common methodology adopted in choosing a technique is by defining the Knudsen number (Kn),

$$Kn = \frac{\lambda}{L}, \tag{1.30}$$

where λ represents the molecular mean free path, that is the mean distance a molecule travels before it collides with another molecule, and L represents the

characteristic length scale of a system. In addition, the above definition is also known as the body-length global (BLG) Knudsen number, Kn_{BLG}. By replacing the mean free path, in the above definition, with the local mean free path, λ_{loc}, it is then termed the body-length local (BLL) Knudsen number, Kn_{BLL}. Another definition is called the gradient-length local (GLL) Knudsen number, Kn_{GLL}, and is written as

$$Kn_{GLL} = \frac{\lambda}{\psi}\left|\frac{d\psi}{dl}\right|, \tag{1.31}$$

where ψ is a quantity of interest, for example pressure, density, temperature or velocity magnitude and the derivative represents the maximum gradient and l is some distance between two points in the flowfield. Boyd *et al.* [36] proposed this definition, after carrying out investigations of one-dimensional normal shock waves and two-dimensional bow shocks, as a continuum breakdown parameter.

Figure 1.2 shows all flow regimes, based on [4, 37, 38], and indicates the accuracy and efficiency routes too. At low Knudsen numbers the gas is dominated with molecules colliding with one another and is in thermodynamic equilibrium, however as the Knudsen number increases from 0.1 non-equilibrium effects become important, that is the overall temperature of a gas departs from the temperature caused by the translational and internal modes and the velocity distribution function is not of Maxwell-Boltzmann form. Since molecules colliding with one another and surfaces drives the state to equilibrium non-equilibrium phenomenon in a gas is established due to the scarce number of collisions occurring. Hence, the non-equilibrium phenomenon becomes more important with increasing Knudsen number or rarefaction. Each of the regimes illustrated in figure 1.2 are described next.

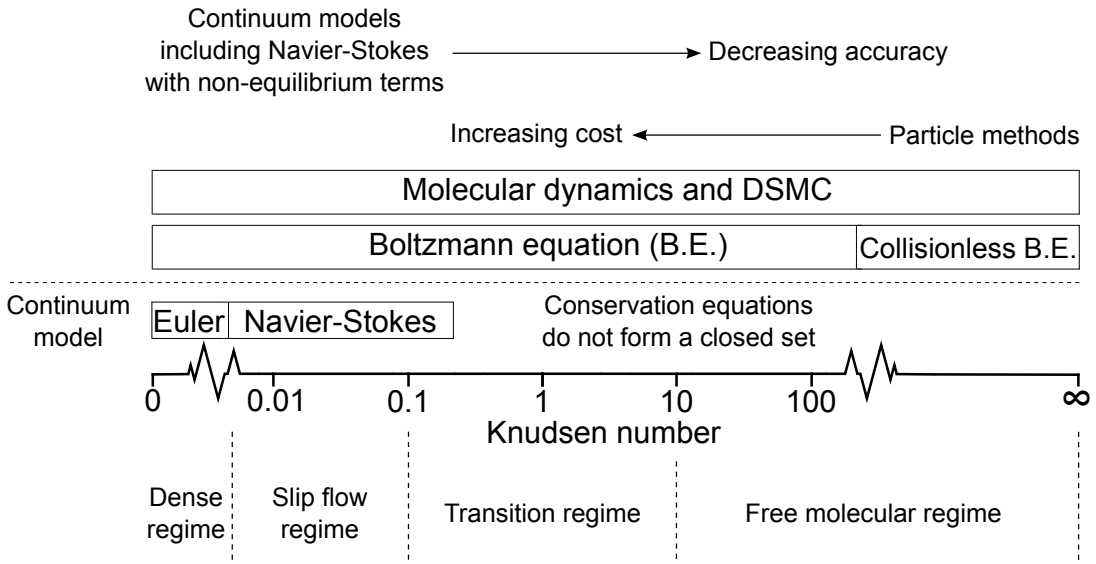

Figure 1.2: The flow regimes and limits on the mathematical models and the accuracy and efficiency routes in calculating the gas flow.

Continuum regime

The continuum regime decribes gas flows that are in equilibrium or very close to it. Such flows are driven to this state due to the molecular collisions with other molecules or surfaces occurring abundantly in a small amount of time in comparison to the macroscopic time scale. The Navier-Stokes equations are predominantly used in this regime as it is very efficient in predicting the flow phenomena. The Navier-Stokes equations can be derived from the Chapman-Enskog expansion of the Boltzmann equation [39] where the Chapman-Enskog solution is a power-series solution of the Boltzmann equation.

Although molecule-based methods can solve the flows in this regime they are not necessary as all the macroscopic properties can be characterised as average values in cells that are larger than the microscopic phenomena of the gas. Furthermore, molecule-based methods are very expensive for large length-scale problems in the continuum regime. Ahmad *et al.* [7] investigated the aerothermodynamics of a full-size re-entry vehicle at many altitudes using a particle-based technique

called *dsmcFoam* and it was found that as the altitude decreased the number of particles required in the simulation increased and as a result increased the computational time. Also, as the Knudsen number becomes close or equal to zero, molecular diffusion can be neglected and the Navier-Stokes equations reduce to the inviscid Euler equations [37].

Slip regime

As stated previously a gas is driven to an equilibrium state due to the abundant number of collisions occurring, however, as the Knudsen number increases there are an insufficient number of collisions to drive the state to equilibrium. As result the gas starts to experience a non-equilibrium behaviour, in particular close to any bounding surface. This phenomenon is observed when the wall temperature and velocity represented as T_W and U_W, respectively, are not the same to the gas temperature and velocity represented as T_{gas} and U_{gas}, respectively. These occurrences are known as the temperature jump and velocity slip. The Navier-Stokes equations can be extended into the slip regime by the addition of Smoluchowski's temperature jump [40] and Maxwell's velocity slip [41] boundary models. For planar surface they are described as [37]

$$T_{gas} - T_W = \frac{2 - \sigma_{TA}}{\sigma_{TA}} \left[\frac{2\gamma}{\gamma + 1} \right] \frac{\lambda}{Pr} \left(\frac{\partial T}{\partial y} \right)_W \tag{1.32}$$

$$\text{and } U_{gas} - U_W = \frac{2 - \sigma_{TMA}}{\sigma_{TMA}} \lambda \left(\frac{\partial U}{\partial y} \right)_W + \frac{3}{4} \frac{\mu}{\rho T_{gas}} \left(\frac{\partial T}{\partial x} \right)_W, \tag{1.33}$$

where x and y are the streamwise and normal directions, respectively. σ_{TA} and σ_{TMA} are the thermal-accommodation coefficient and tangential-momentum-accommodation coefficient, respectively and the reader is referred to [37] on how they are calculated. Also, γ, Pr and μ represent the specific heat ratio, Prandtl

number and dynamic viscosity, respectively.

Transition and free-molecular regimes

The Boltzmann equation can be calculated with less difficulty in the free-molecular regime, as in this regime the collision integral can be set to zero. However, a solution to the Boltzmann equation is difficult to acquire in the transition regime, as molecular collisions are present and they can influence the dynamics of the gas.

Attempts have been made at solving the Boltzmann equation, in the transition regime, with certain assumptions. The first method involves the moments taken of the Boltzmann equation [39, 42], Vincenti and Kruger [35] have shown the Boltzmann equation simplifies when the moment is taken to be the mass, momentum or energy, as the change in the moment of the collision integral is zero. Recent studies [43] have extended the moment method, but it still cannot solve gas flows over complex three-dimensional geometries and is limited to simple problems such as Couette and Poiseuille flows. The other method makes use of the so-called model equations briefly mentioned in section 1.2.1, for example the Bhatnagar-Gross-Krook method [19, 20], this simplifies the collision integral of the Boltzmann equation but is limited to gas systems that involve a small departure from equilibrium. However, the collision integral can be linearised and the Boltzmann equation solved without the need of high performance computers [4].

The DSMC method overcomes the computational and numerical limitations that are present with using the Boltzmann equation directly, model equations or moment methods for simulations over complex three-dimensional geometries in the transition regime. In addition, the DSMC technique prevails over the Navier-Stokes equations at capturing the non-equilibrium phenomenon effectively. The DSMC method, a stochastic particle method that produces a solution to the Boltzmann equation [44], has now become the dominant numerical technique in

solving gas flows in the transition regime and this technique is employed for all investigations considered in this thesis. A thorough investigation of this method is provided in the following chapter.

1.3 Project objectives and key developments

The open source DSMC code, called *dsmcFoam*, was recently written within the framework of the open source computational fluid dynamics (CFD) toolbox OpenFOAM [45] using the underlying principles of the open source molecular dynamics solver created by Macpherson [46], also in the OpenFOAM environment. *dsmcFoam* was developed by OpenCFD Ltd and the University of Strathclyde. This thesis focusses on the benchmarking of this new open source DSMC code and outlines techniques for *dsmcFoam*, introduced by the author, to improve the efficiency and accuracy of simulations. Furthermore, the author has investigated the aero-thermodynamics over re-usable single-stage to orbit space-planes, called Skylon and CFASTT-1. The latter space-plane has been developed by the author and others from the research group called *Centre for Future Air-Space Transportation Technology* at the University of Strathclyde. Due to the length requirements the Skylon and CFASTT-1 investigations have not been considered in this thesis, however for more information on those studies the reader is referred to References [7–9]. The main contributions by the author, that are discussed in this thesis, are:

- Parallel efficiency studies carried out of *dsmcFoam* on high performance computers at the University of Strathclyde and Argonne National Laboratory (U.S.).

- A new domain decomposition method developed to increase the efficiency of

parallel *dsmcFoam* simulations. The domain is split up in a way that each processor has approximately the same number of particles to work with.

- Benchmarking of *dsmcFoam* with analytical solutions, other established DSMC codes and experimental data available in the literature.
- A TASC routine to increase the accuracy, from a microscopic point of view, of *dsmcFoam* simulations without the need to refine the mesh.
- A radiative-based wall boundary model, called the DWTM, introduced into *dsmcFoam* to provide a surface temperature definition related to the heat flux.

The work that has been carried out by the author is building on one of the only open-source DSMC codes available.

1.4 Published papers

The work during the PhD studies has contributed to the following papers:

1. Abdul O. Ahmad, Thomas J. Scanlon and Richard E. Brown. Aerodynamic environment of the Skylon configuration under rarefied flow conditions. *Technical report to the German aerospace center (DLR) and Reaction Engines*, 2010.
2. Abdul O. Ahmad, Thomas J. Scanlon and Jason M. Reese. Capturing shock waves using an open-source, direct simulation Monte Carlo (DSMC) code. *Proceedings of the fourth European conference for aerospace sciences, St. Petersburg, Russia*, 2011.

3. Abdul O. Ahmad, Thomas J. Scanlon and Jason M. Reese. Benchmarking a new, open-source direct simulation Monte Carlo (DSMC) code for hypersonic flows. *Proceedings of the twenty-eighth international symposium on shock waves, Manchester, U.K.*, 2011.

4. Abdul O. Ahmad, Christie Maddock, Thomas J. Scanlon and Richard E. Brown. Prediction of the aerodynamic performance of re-usable single-stage to orbit vehicles. *Proceedings of the first international space access conference, Paris, France*, 2011.

5. Romain Wuilbercq, Abdul O. Ahmad, Thomas J. Scanlon and Richard E. Brown. Towards robust aero-thermodynamic predictions for re-usable single-stage to orbit vehicles. *Proceedings of the eighteenth AIAA/ 3AF international space planes and hypersonic systems and technologies conference, Tours, France*, AIAA Paper 2012-5803, 2012.

Chapter 2

The DSMC technique

The direct simulation Monte Carlo algorithm, a stochastic molecular numerical method, is predominantly used to model dilute flows. Developed over forty years ago by Bird [4] the DSMC technique has over-time incorporated sophisticated features such as virtual sub-cells [47] for nearest neighbour collisions, variable time-steps and mesh refinement/ coarsening [2, 48, 49]. As a result the DSMC technique is now the dominant numerical technique in solving complex and rarefied engineering applications that include re-entry gas flows over spacecraft [7–9, 50–59] to gas flows through micro-channels [60–64]. As discussed in the previous chapter, the Boltzmann equation is also appropriate for modelling these flows but due to its complex collision term, it is challenging to solve numerically. Furthermore, Wagner's proof [44] has shown DSMC to provide a solution to the Boltzmann equation as the ratio of simulated DSMC molecules to real molecules in the gas flow tends towards the true value, that is this ratio tends to one.

This chapter provides an introduction to DSMC and the methodology behind it. It then briefly discusses the established DSMC codes used in the literature, and provides a description of the standard *dsmcFoam* code including its efficiency in parallel setups. A new domain decomposition method for parallel *dsmcFoam*

systems is also introduced that speeds up the simulations in comparison to current methods.

2.1 Introduction

Real gas flows may be modelled using the direct simulation Monte Carlo method by using simulator particles that represent a large number of real atoms or molecules. Earlier DSMC calculations were limited to particles in the order of hundreds due to the computational resources available at that time, for example the first DSMC publication used five-hundred DSMC particles [65], modern computers can simulate several million particles. In addition, with the use of modern high performance computers more than a billion particles may be simulated - parallel efficiency studies of *dsmcFoam* are investigated using up to two billion particles in section 2.3.4.

The DSMC technique allows particles to move and collide using kinetic theory considerations that treat the equilibrium and non-equilibrium gas flow behaviour with sufficient accuracy. DSMC considers molecular collisions using stochastic rather than deterministic procedures - used by MD calculations. The decoupling of particle ballistic motion and particle collisions, over a time-step that is roughly a third of the mean collision time, improves the computational efficiency of DSMC greatly in comparison to systems that employ MD. However, DSMC is still computationally expensive as it needs to track a huge number of particles and process many collisions, and it needs to do this for many time-steps to reduce the statistical scatter to an adequate level.

Furthermore, DSMC requires a computational mesh to process the collisions but more importantly to recover the macroscopic properties. The collision partners can only be chosen in a mesh cell, this promotes particles that are close to

each other to collide, and to ensure this is as realistic as possible the size of the cell has to be a fraction of the local mean free path. However, the size of the cell becomes less important with the use of eight sub-cell [4] or transient adaptive sub-cell [5] methods.

In 1963 Bird presented the first DSMC paper [65] and this dealt with the relaxation to a Maxwellian speed distribution of hard sphere molecules, of which all were initially assigned the same velocity. In addition, the molecule velocities were only stored during the simulation and the collisions were based on the relative velocity of the two randomly selected colliding particles. The foundation of processing these collisions is used in modern DSMC simulations but the theory has been extended to include variable cross-sections, that is the collision cross-section of the two colliding particles is a function of their relative velocity. This method was developed by Bird [4, 66] and is called the variable cross-section hard sphere (VHS) model. In addition, Bird's no-time-counter (NTC) technique built into the DSMC method is used to determine the correct collision rates and this is discussed in the following section.

From 1964 to 1968 shockwave structures were initially investigated by Bird using DSMC in environments that were constrained to single species [67, 68] and gas mixtures [69]. In addition, the theory of a DSMC simulator particle representing more than one real molecule was introduced. In 1970, Bird then investigated the breakdown of translational and rotational equilibrium of diatomic molecules [70]. Soon after, a phenomenological model that redistributed energy between translational and rotational modes was presented [71] and called the Larsen-Borgnakke model [4, 72]. And this has more recently been extended to include the vibrational mode [4, 73] and is used in modern DSMC calculations.

2.2 Methodology

A flowchart of the standard DSMC methodology is illustrated in figure 2.1. After defining the physical extent of the computational domain, for example simulating gas flows over re-entry vehicles or through micro-channels, the first step is to initialise the system by introducing DSMC particles into the computational mesh. The macroscopic density, velocity and temperature is used to determine the amount of DSMC particles required in the system, and the thermal velocities of each particle are based on the Maxwell-Boltzmann distribution at the macroscopic translational temperature. If systems also require internal modes of energy, they can be determined by the macroscopic internal temperatures that are in the rotational or vibrational form. Sampling from the distribution functions are described in detail in Appendix C of Reference [4].

The second step is the movement of the particles, this respectively includes inserting and deleting any particles that move in and out of the computational domain, and processing the interactions with the wall boundaries. The particles are first entered into the system through the inlet boundaries according to the equilibrium Maxwellian distribution function [4], therefore the inlet number flux, $\dot{N}_{inlet}$, is defined as

$$\dot{N}_{inlet} = \frac{n_{inlet}\sqrt{kT_{inlet}}\left[exp\left(-\zeta^2\ cos^2\theta_n\right) + \sqrt{\pi}\zeta\ cos\theta_n\left\{1 + erf\left(\zeta\ cos\theta_n\right)\right\}\right]}{\sqrt{2m\pi}}, \tag{2.1}$$

where n, T, m and k represent the number density, temperature, mass and Boltzmann constant, respectively. Also, the subscript *inlet* indicates the properties at the inlet boundary and using the inlet flow velocity, U_{inlet}, the molecular speed ratio, ζ, is determined as

$$\zeta = \frac{U_{inlet}}{\sqrt{2RT_{inlet}}}, \tag{2.2}$$

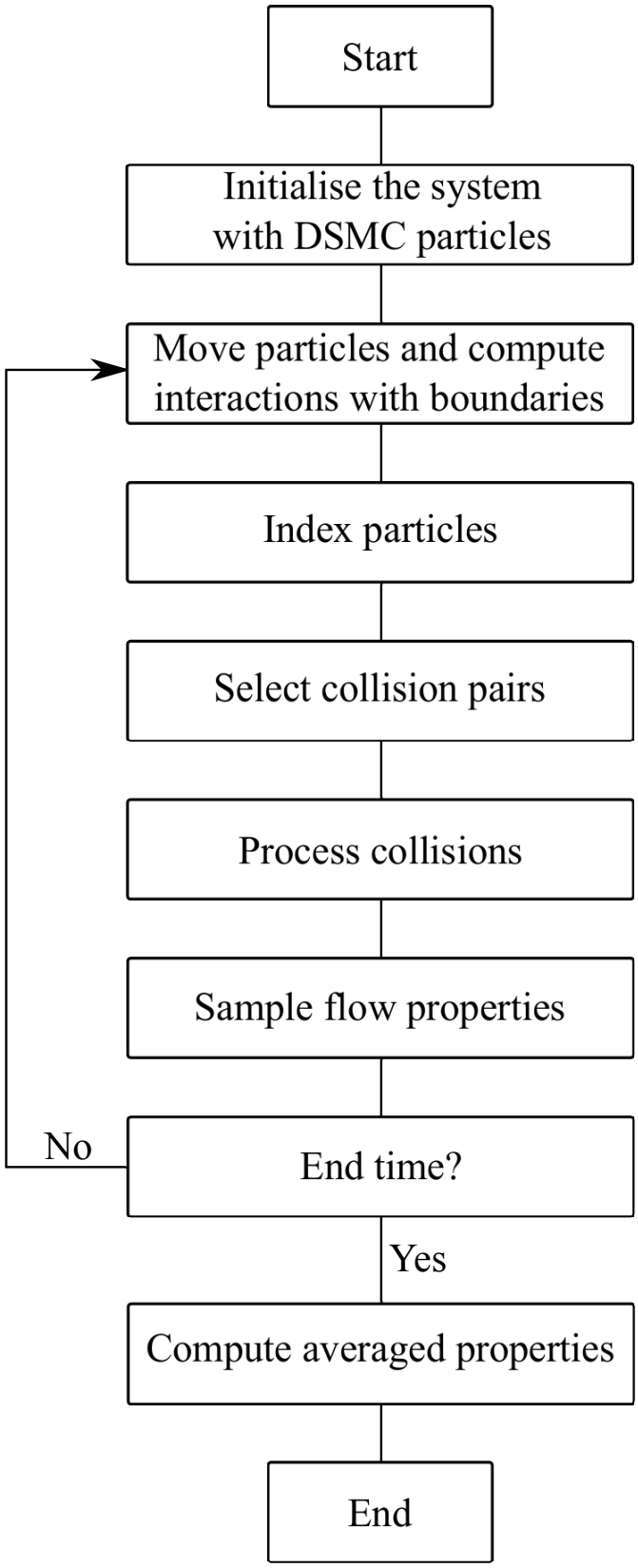

Figure 2.1: Flowchart of the basic DSMC methodology.

where R is the gas constant. In addition, the angle between U_{inlet} and the unit normal vector of the inlet boundary is represented by θ_n.

The movement of the particles is then processed using their respective velocity vectors and the time-step - normally set to be a fraction of the mean collision time. Once the particles are moved they either remain in the same mesh cell or occupy the neighbouring cells, this may include moving into a different processor zone. Furthermore, particles that interact with the wall boundaries are reflected off the wall according to a molecular surface model and the most common models incorporate the specular and/ or Maxwellian diffuse reflections. The specular reflection model simply reverses the perpendicular component of the particle's velocity and diffuse reflections reset the velocity according to the biased-Maxwellian [74] for the normal component and the standard Maxwell-Boltzmann distribution for the parallel components. Wall macroscopic properties are then determined based on the pre- and post-interaction properties, that is momentum or energy, of particles that strike the wall. These macroscopic properties include surface pressure, heat transfer and shear stress. In the third step, the particles are re-indexed to the mesh cells as the following steps performing the collisions and sampling are based on this information.

The fourth step defines the collision pairs that can occur and this is performed in a probabilistic manner to reduce the huge computational effort that is required with deterministic MD calculations. In majority of DSMC simulations a particle can collide with another particle only if they are in the same cell. In addition, to focus collisions in smaller volumes many DSMC codes employ sub-cells normally eight in each cell and only if a cell contains more than one particle. Another technique is to base the sub-cells on the number of particles in each cell [5], therefore in systems with large gradients each cell will have a different number of sub-cells. This method has also been introduced by the author into *dsmcFoam*

and will be discussed in chapter 4.

Furthermore, it is important to ensure the correct number of particle collisions that occur are in accordance with theory. Some methods exist to determine this and they include the simplified Bernoulli trials (SBT) [75] and majorant frequency scheme (MFS) [76] but the most common is the no-time-counter (NTC) scheme [4, 77] introduced by Bird. This section is focussed on the NTC method as this is used in the simulations presented in this thesis, for the other techniques the reader is referred to their respective referenced papers and for a comparison between the NTC and MFS schemes the reader is referred to Reference [78] where it shows the two techniques eventually produce identical results. In addition, the author believes the SBT is a new promising method as it can produce reasonable results with low number of particles [75], but currently it is cumbersome to integrate into arbitrary three-dimensional cells that employ sub-cells. Although this has not been used with complex geometries, it is thought [79] that determining the sub-cell volume within the sampling cell in complex mesh structures might be very computationally expensive.

The number of NTC collision pairs selected from a cell at a time-step t_s are

$$\frac{N_{RMDP} N_{DSMC}^{avg} \left(N_{DSMC}^{avg} - 1\right) t_s \left(\sigma_{ccs} c_r\right)_{max}}{2 V_{cell}} \tag{2.3}$$

where N_{RMDP} and V_{cell} represent number of real molecules one DSMC particle represents and cell volume, respectively. $\left(\sigma_{ccs} c_r\right)_{max}$ is the maximum product of the collision cross section, σ_{ccs}, and relative speed, c_r, of all possible collision pairs and the average number of DSMC particles in the cell, N_{DSMC}^{avg}, is determined as

$$N_{DSMC}^{avg} = \frac{n V_{cell}}{N_{RMDP}}. \tag{2.4}$$

Particles i and j are then randomly chosen from all particles in the cell for a possible collision, using the acceptance-rejection method [4, 30] the collision is accepted if

$$F_{rand} < \frac{(\sigma_{ccs} c_r)_{ij}}{(\sigma_{ccs} c_r)_{max}}, \tag{2.5}$$

where F_{rand} is a random fraction chosen in [0, 1) and the numerator on the right-hand side of this equation represents the product of the collision cross-section and relative speed of particles i and j.

Furthermore, if the collision is accepted then the particles collide and in a DSMC collision the particles' velocities are reset but the position remains the same as prior to the collision. To determine the post-collision velocity of particle i, c_i, and particle j, c_j, in elastic collisions[1] firstly consider the conservation of momentum,

$$\mathbf{c}_{cofm} = \frac{m_i \mathbf{c}_i + m_j \mathbf{c}_j}{m_i + m_j} = \frac{m_i \mathbf{c}_i^* + m_j \mathbf{c}_j^*}{m_i + m_j} = \mathbf{c}_{cofm}^*, \tag{2.6}$$

where m_i and m_j represent the mass of particles i and j, respectively and the superscript $*$ denotes post-collision properties, thus the centre of mass velocity, $\mathbf{c}_{cofm}$, remains unchanged by the collision. And from the conservation of energy,

$$c_r = |\mathbf{c}_i - \mathbf{c}_j| = \left|\mathbf{c}_i^* - \mathbf{c}_j^*\right| = c_r^*, \tag{2.7}$$

the magnitude of the relative velocity of a particle, $\mathbf{c}_r$, is not affected by the collision. To determine $\mathbf{c}_r^*$ equations 2.6 and 2.7 are required along with the azimuthal angle θ_a and elevation angle θ_e. The azimuthal angle is uniformly distributed between 0 and 2π radians, therefore it is determined as

$$\theta_a = 2\pi F_{rand}. \tag{2.8}$$

[1] No rotational or vibrational energy is exchanged in elastic collisions.

The elevation angle is distributed with a probability,

$$f\left(\theta_e\right) d\theta_e = sin\theta_e d\theta_e, \tag{2.9}$$

and using the change of variable q_{cov},

$$q_{cov} = cos\theta_e, \tag{2.10}$$

results in

$$f\left(q_{cov}\right) dq_{cov} = \frac{1}{2} dq_{cov}, \tag{2.11}$$

therefore q_{cov} is uniformly distributed in [-1, 1] [30], thus

$$q_{cov} = 2F_{rand} - 1, \tag{2.12}$$

$$\theta_e = cos^{-1} q_{cov} \tag{2.13}$$

$$\text{and} \;\; sin\theta_e = \sqrt{1 - q_{cov}^2}. \tag{2.14}$$

Finally, the post-collision relative velocity is defined in its three components as

$$\mathbf{c}_r^* = c_r \left| \left(sin\theta_e cos\theta_a\right) \hat{\mathbf{x}} + \left(sin\theta_e sin\theta_a\right) \hat{\mathbf{y}} + cos\theta_e \hat{\mathbf{z}} \right|, \tag{2.15}$$

and the post-collision velocities of both particles are determined as

$$\mathbf{c}_i^* = \mathbf{c}_{cofm}^* + \frac{1}{2} \mathbf{c}_r^*, \tag{2.16}$$

$$\text{and} \;\; \mathbf{c}_j^* = \mathbf{c}_{cofm}^* - \frac{1}{2} \mathbf{c}_r^*. \tag{2.17}$$

In the case of inelastic collisions, energy can also exist in the rotational, vibra-

tional and electronic forms for each particle. Generally, for hypersonic gas flows the electronic modes are ignored [80], and the following will focus on rotational and vibrational forms only however, for further information on the electronic mode the reader is referred to [4] and the use of the electronic energy in the analysis of jet flows is in [81]. Firstly, the dominant DSMC method for exchanging rotational energy is through the phenomenological[2] Larsen-Borgnakke model [71]. Only a certain number of all collisions are treated as inelastic through this model as to maintain a realistic rotational relaxation rate. For a particle that only exchanges energy in the translational and rotational forms the rotational relaxation is first checked when a collision takes place, and a particle is given a rotational energy if

$$F_{rand} < \frac{1}{Z_{rot}}, \tag{2.18}$$

where Z_{rot} is the rotational relaxation collision number and the rotational energy is based on a Boltzmann distribution [4, 80]. Once this energy is determined it is subtracted from the total translational energy available to the collision pair to conserve energy and a new post-collision relative speed is defined as

$$c_r^* = \sqrt{\frac{2\varepsilon_{trans}}{m_r}}, \tag{2.19}$$

where ε_{trans} is the translational energy of the collision pair post rotational relaxation and the reduced mass, m_r, is defined as

$$m_r = \frac{m_i m_j}{m_i + m_j}. \tag{2.20}$$

Using the new post-collision relative speed, the post-collision velocities of particles

[2]Phenomenological models consist of the simplest possible molecular mathematical relations of a process that reproduces necessary effects.

i and j are determined by the process from equations 2.8 to 2.17.

The rotational mode is excited in most DSMC simulations of diatomic particles however, in systems that experience high temperatures the vibrational mode becomes very important and it is essential to include this in the DSMC implementation as it reduces the energy available to the translational and rotational modes. In addition, the number of collisions required for vibrational relaxation is very large in comparison to translational and rotational relaxation, as a result encouraging non-equilibrium in a gas flow. Bergemann and Boyd [82] formulated a quantised vibrational energy exchange model to tackle the vibrational mode in DSMC simulations using the Larsen-Borgnakke approach.

Furthermore, a serial application of the quantum Larsen-Borgnakke model is used in this thesis and the redistribution of vibrational energy is defined using the harmonic oscillator model. In addition, the vibrational energy is redistributed according to the collision energy [73]. First the maximum quantum level, v^q_{max}, of the particle is determined,

$$v^q_{max} = \left\lfloor \frac{\varepsilon_{coll}}{k\Theta_{vib}} \right\rfloor, \tag{2.21}$$

where Θ_{vib} is the characteristic vibrational temperature, that is the energy between quantum levels, and ε_{coll} is the total energy of the relative translational energy of the collision particles and the pre-collision vibrational energy of a particle from the collision pair. The vibrational energy, ε_{vib}, of a particle is initially assigned as

$$\varepsilon_{vib} = v^q k\Theta_{vib}, \tag{2.22}$$

$$\text{where } v^q = \left\lfloor \frac{-ln\left(F_{rand}\right) T_{vib}}{\Theta_{vib}} \right\rfloor \tag{2.23}$$

and T_{vib} is the vibrational temperature. Using equation 2.21 the collision tem-

perature, T_{coll}, is defined as

$$T_{coll} = \frac{v_{max}^{q} \Theta_{vib}}{\frac{7}{2} - \omega}, \tag{2.24}$$

where ω is the viscosity index. The vibrational collision number [83], Z_{vib}, is then determined as

$$Z_{vib} = \left(\frac{\Theta_{dis}}{T_{coll}}\right)^{\omega_{ij}} \left[Z_{ref}\left(\frac{\Theta_{dis}}{\Theta_{vib}}\right)^{-\omega_{ij}}\right]^{\left[\left(\frac{\Theta_{dis}}{T_{coll}}\right)^{\frac{1}{3}}-1\right]/\left[\left(\frac{\Theta_{dis}}{\Theta_{vib}}\right)^{\frac{1}{3}}-1\right]}, \tag{2.25}$$

where Θ_{dis} is the characteristic dissociation temperature and ω_{ij} is calculated as

$$\omega_{ij} = \frac{\omega_i + \omega_j}{2}, \tag{2.26}$$

and

$$Z_{ref} = \left(\frac{C_1}{(\Theta_{vib})^{\omega_{ij}}}\right)^{\omega_{ij}} exp\left(C_2 \left(\Theta_{vib}\right)^{-\frac{1}{3}}\right), \tag{2.27}$$

where C_1 and C_2 are constants based on the data of Millikan and White [84]. The molecular properties including the characteristic temperatures and constants, C_1 and C_2, are in Appendix A of Reference [4].

Subsequently, the particle is tested for vibrational energy exchange and is accepted according to:

$$F_{rand} < \frac{1}{Z_{vib}}, \tag{2.28}$$

and v^{q*}, the post-collision vibrational quantum level, is determined using the acceptance-rejection method of the quantised Larsen-Borgnakke probability distribution function [83]

$$\frac{f}{f_{max}} = \left(1 - \frac{v^{q*} k \Theta_{vib}}{\varepsilon_{coll}}\right)^{\frac{3}{2}-\omega_{ij}}. \tag{2.29}$$

Once the vibrational energy is determined it is subtracted from the translational energy and then experiences rotational relaxation as described before. In addition, some systems encounter chemical reactions and they are energised at very high temperatures, however they are not considered in this thesis as the systems do not reach those high temperatures. The most common method to tackle chemical reactions in DSMC is through the total collision energy (TCE) technique [4] that is a function of the macroscopic temperature, however more recently a quantum-kinetic (QK) model [73, 85, 86] has been developed that does not depend on the macroscopic temperature and is based on the quantum Larsen-Borgnakke method.

The final steps are to sample and compute the average macroscopic properties, this is necessary to physically design real engineering applications. The sampling step follows the same principles as in section 1.2.2, however the amount of real molecules each DSMC particle represents has to be accounted for. For example, the mass density, ρ, in each computational cell with a volume V_{cell}, that has N_{DSMC}^{avg} average number of DSMC particles over a measurement time, is determined as

$$\rho = \frac{N_{RMDP} N_{DSMC}^{avg} m}{V_{cell}}. \tag{2.30}$$

Finally, all CFD calculations are either in steady-state or transient, the same applies to DSMC simulations. For steady-state systems, DSMC is initially simulated and the number of particles are monitored to determine when steady-state has been achieved, during steady-state the properties are measured over a large number of time-steps to adequately reduce the statistical scatter. Figure 2.2 shows a typical graph used by DSMC users to indicate the point of steady-state by monitoring the number of DSMC particles from the beginning to the end of a simulation. In addition, this graph has been truncated at the end, but normally

it is simulated until the properties are resolved - usually run for an extra ten times the number of time-steps a simulation requires to steady-state. And a lot longer for low speed gas flows through micro-channels as the statistical scatter tends to be greater than systems that involve hypersonic gas flows over space vehicles. This is due to the low signal-to-noise ratio in low-speed rarefied gas flows [87]. Furthermore, the focus of this thesis is on steady-state problems but for transient calculations the same simulation needs to be run many times and at each time-step the results are ensemble averaged.

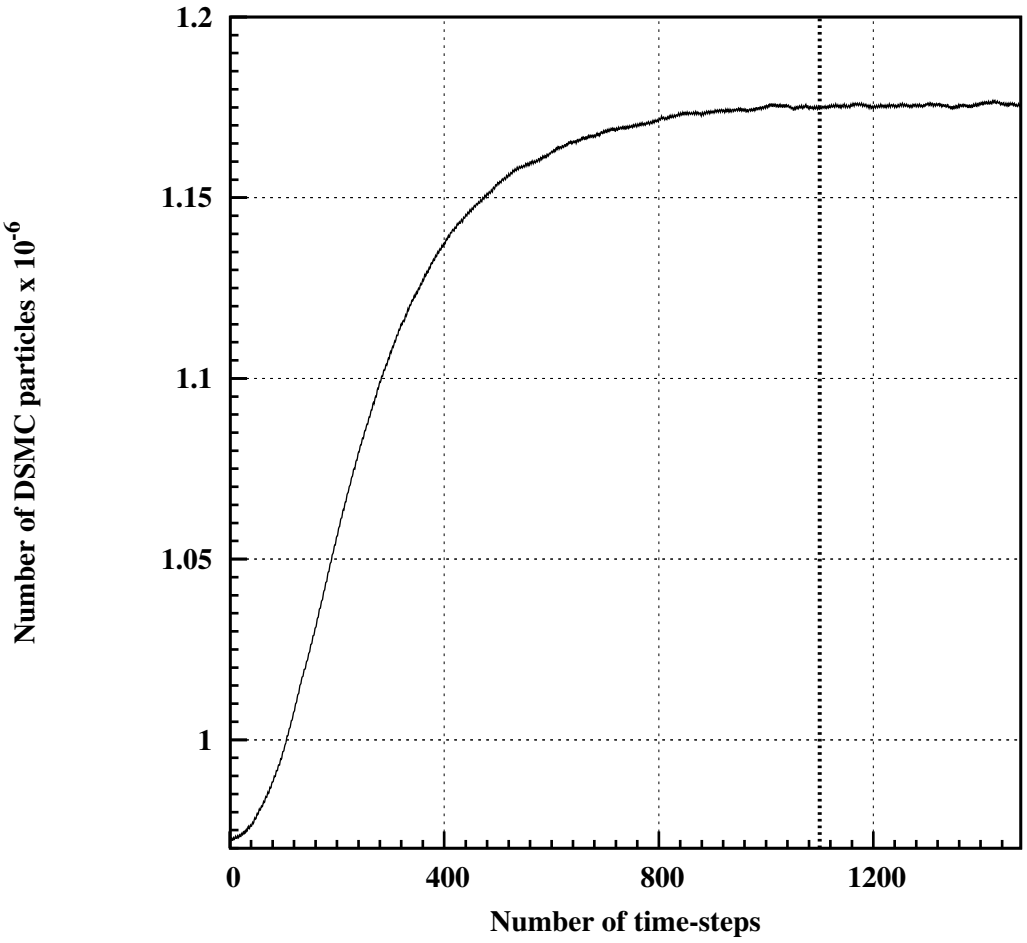

Figure 2.2: A typical graph used by DSMC users to indicate the point of steady-state. The full line represents the number of DSMC particles in the system and the dotted line indicates the point when averaging can commence.

2.3 Established DSMC codes

Most of the established DSMC codes are briefly described in this section. The standard features of the open-source DSMC solver called *dsmcFoam* are listed. In addition, the efficiency of *dsmcFoam* using multiple CPUs are investigated and a new domain decomposition method for parallel processing is briefly outlined.

2.3.1 Bird's DSMC codes

Bird who originally developed the DSMC method has three DSMC codes available on his website [88]. The three DSMC codes are:

- DS1V - a one-dimensional version that supports both steady and transient planar, cylindrical and spherical gas flows.
- DS2V - a two-dimensional version that is of commercial quality and is well established, and it includes a graphical user interface.
- DS3V - a three-dimensional version that has similar capabilities as DS2V.

In addition, all codes are free to download and use however, the source code is not available for DS2V and DS3V. The Fortran source code of DS1V is freely available and primarily used to develop new DSMC routines or models. DS2V is Bird's most advanced code and includes the sophisticated procedures outlined in Reference [2].

2.3.2 SMILE

Statistical Modeling in Low-Density Environment (SMILE) [89] is a parallel DSMC code written using FORTRAN90. It has been developed by the Laboratory of Computational Aerodynamics from the Khristianovich Institute of Theoretical and Applied Mechanics of the Siberian Branch of the Russian Academy

of Sciences. SMILE is developed with a graphical user interface and can simulate multi-species gas flows over arbitrary two- or three-dimensional, or axi-symmetric geometries. The MFS [76] is used to determine the collisions and chemical reactions are simulated using the TCE model [89]. SMILE is mainly used in Russia and not readily distributed, with some exceptions [3, 90].

2.3.3 MONACO

MONACO is a parallel DSMC code that has been in development since 1996 by Boyd [80, 91–93]. MONACO can handle multi-species gas flows over arbitrary two- or three-dimensional geometries within structured or unstructured grids, and chemical reactions are simulated using the TCE model. In addition, MONACO may only be used within the United States and is therefore not available to the wider scientific community outside of the U.S.A.

2.3.4 *dsmcFoam* background

The open-source DSMC code, called dsmcFoam, has been developed at the University of Strathclyde. The code has been written within the framework of the open-source, under the GNU general public licence, CFD toolbox OpenFOAM [45] that can be downloaded freely from www.openfoam.com. Scanlon *et al.* [94] successfully tested this - producing excellent agreement with both analytical solutions and other conventional DSMC codes. The main features of dsmcFoam are its C++ modularity, its unlimited parallel processing capability and its ability to easily handle arbitrary, complex three-dimensional geometries. *dsmcFoam* originated from the core characteristics of a MD code implemented by Macpherson [46] in the OpenFOAM toolbox. The core characteristics of *dsmcFoam* include particle initialisation in arbitrary geometries and particle tracking

in structured or unstructured, arbitrary, polyhedral meshes.

The mesh used in *dsmcFoam* simulations can be constructed with OpenFOAM utilities: *blockMesh* and *snappyHexMesh* [45]. In addition, the mesh can also be imported into OpenFOAM from another software package, for example Gambit [95]. The mesh and the final results can be post-processed using Paraview and this is provided as an optional with the OpenFOAM installation.

Molecular collisions in *dsmcFoam* are simulated using the VHS model and selected according to the NTC method, with the Larsen-Borgnakke phenomenological model governing the energy exchange between kinetic and internal modes. *dsmcFoam* can solve steady and transient problems, using an arbitrary number of gas species and an automatic eight sub-cell generator in each cell that has more than one particle. In addition, *dsmcFoam* can simulate free-stream, symmetry and periodic boundaries as well as surface models that are based on specular or Maxwellian or a mix of both interactions. Furthermore, Scanlon *et al.* [96] are in the process of including QK chemical reactions into *dsmcFoam*.

Once the computational mesh is constructed then to simulate steady-state gas flows through this the following steps are required for *dsmcFoam*:

1. Define boundary conditions (including free-stream and wall), species molecular properties and time-step size.

2. Initialise mesh with DSMC particles using *dsmcInitialise*.

3. Run the simulation using *dsmcFoam*.

4. Begin time averaging when the system is at steady-state.

5. Post-process macroscopic intensive properties[3] from extensive properties[4] using *dsmcFieldsCalc*.

[3]Intensive properties include temperature and velocity.
[4]Extensive properties are mass, momentum and energy.

In the following chapter *dsmcFoam* is benchmarked with analytical solutions, other established DSMC codes and experimental data. This is required as *dsmcFoam* is a new DSMC solver and the accuracy of the code is determined before introducing the advances the author has implemented into *dsmcFoam* and these are outlined in chapters 4 and 5. Also, the following sections discuss the efficiency of *dsmcFoam* and presents a new domain decomposition method for parallel processing that offers an improvement in efficiency for systems that encounter large gradients of flow.

dsmcFoam efficiency

The efficiency is important in all parallel codes as it unveils how well the code has been programmed. This investigation is performed for *dsmcFoam* using a simple periodic box that contains one million cells. This is a suitable case for this study as there are no flow gradients and the number of particles in each cell are approximately the same. Each side of the box has a dimension of 0.05 m and the temperature of the box is at 300 K. Nitrogen and Oxygen particles are simulated with a number density of 0.777×10^{20} m^{-3} and 0.223×10^{20} m^{-3}, respectively. The *simple* decomposition method is used [45] to split up the domain and the parallel scaling factor used to determine the efficiency of this investigation, is calculated as

$$Parallel\ scaling\ factor = \frac{Total\ execution\ time\ of\ a\ parallel\ run}{Total\ execution\ time\ of\ a\ serial\ run}. \qquad (2.31)$$

Figure 2.3 compares the efficiency of *dsmcFoam* against the ideal efficiency for many different parallel configurations, for *dsmcFoam* these configurations employ: 2, 4, 8, 24, 48, 96 and 192 processors. In addition, this study employs ten-million DSMC particles, and a serial configuration is also run to determine the

parallel scaling factor as in equation 2.31 and the starting point of the ideal efficiencies. Figure 2.3 shows that *dsmcFoam* has very good efficiency up to 96 processors and although at 192 processors the efficiency is relatively low in comparison to the ideal it is still better than 96 processors. This graph also shows the efficiency starts to diverge from the ideal from 8 processors and this is due to the communication time increasing between processors, therefore the more the processors the larger the communication time between them hence the largest difference in efficiency with the ideal is noticed at 192 processors. In addition, all *dsmcFoam* efficiency tests considered in this section are run on ARCHIE-WeSt [97], a high performance computer for the West of Scotland and based at the University of Strathclyde. ARCHIE-WeSt has almost 3500 cores for distributed parallel computing that provides almost 38 teraflops peak performance and it also has eight 512GB random-access memory (RAM) large memory nodes, eight GPU servers, two visualisation servers and 150TB of high performance storage. ARCHIE-WeST is compared against the high performance computer available at the Argonne National Laboratory (ANL) [11] using this test case as shown in figure 2.4. This figure shows ARCHIE-WeSt is around 30% faster than ANL's machine and this is because ARCHIE-WeSt employs Intel Xeon X5650 processors and these are better at multi-threaded tasks in comparison to ANL's Intel Xeon X5550 processors [98], also the X5650 processors have a greater cache size as a result storing more instructions as opposed to fetching from the system RAM, the latter process can be very slow.

Furthermore, this *dsmcFoam* efficiency test case is re-run but with one-hundred-million DSMC particles and figure 2.5 compares the new efficiency of *dsmcFoam* against the ideal values that are based on a serial run. An extra efficiency test using 384 processors is also shown in this figure. The efficiency of this test case is very good up to 192 processors and although at 384 processors the efficiency

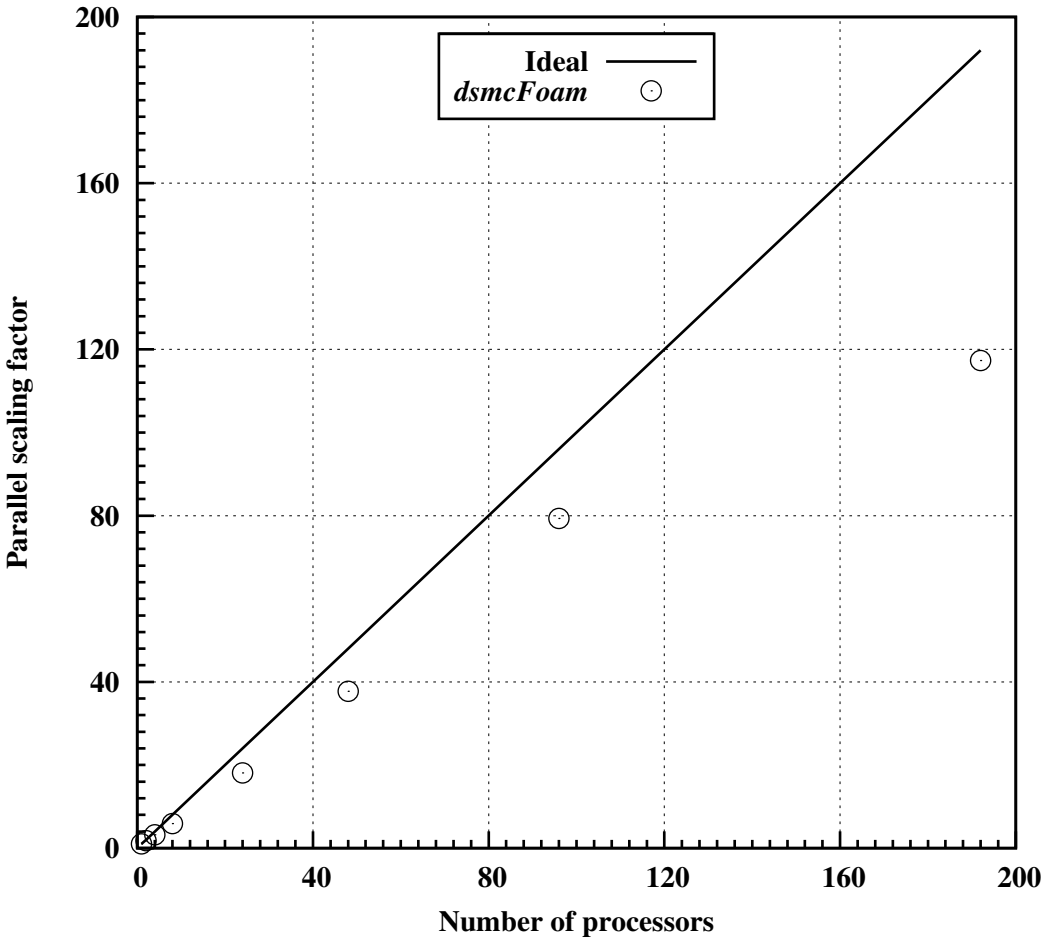

Figure 2.3: Parallel *dsmcFoam* efficiency test using ten-million particles in one-million cells.

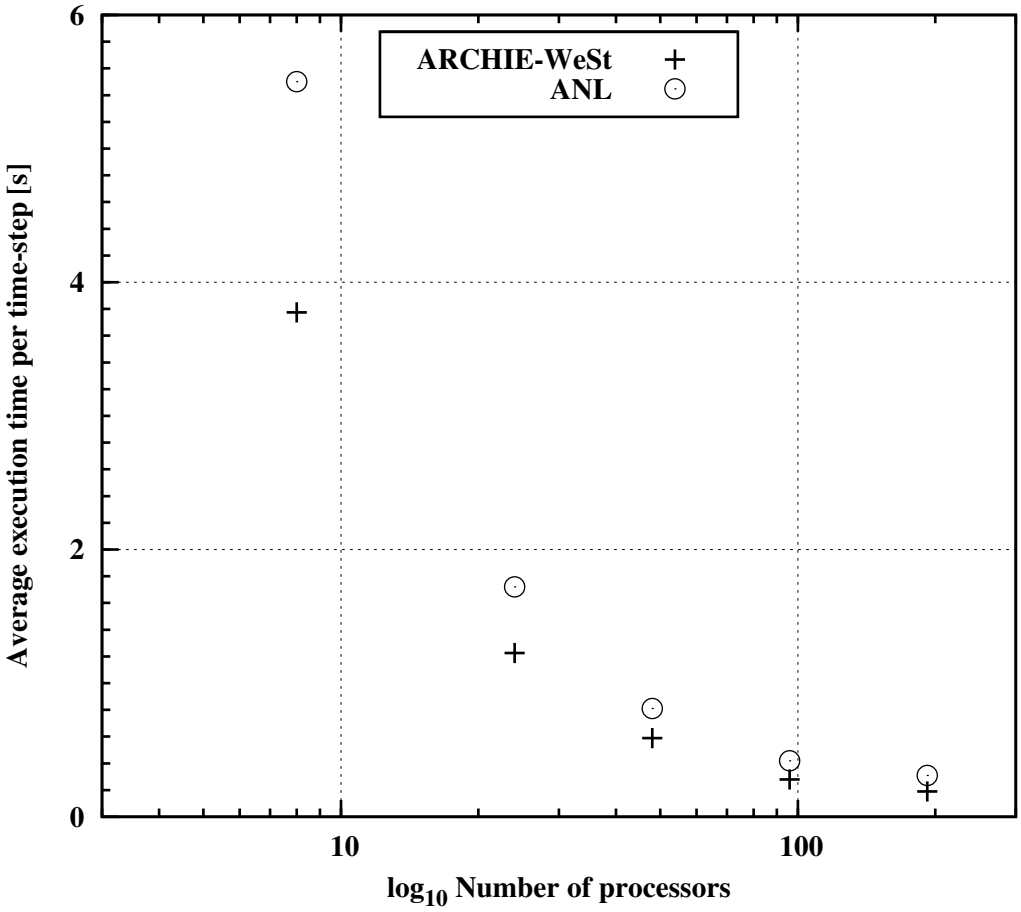

Figure 2.4: Parallel *dsmcFoam* efficiency test using ten-million particles in one-million cells and executed on both ARCHIE-WeST and the high performance computer at ANL.

is low in comparison to the ideal it is still better than 192 processors. In addition, the efficiency of *dsmcFoam* with ten-million particles is very good up to 96 processors and for the test case with one-hundred-million particles the very good efficiency has increased to 192 processors. Therefore, this suggests by increasing the number of DSMC particles in the system the time consumed by moving the particles and processing the collisions becomes larger than the time it takes to move particles from one processor to another, thus by employing more DSMC particles *dsmcFoam* can use more processors but still maintain good efficiency.

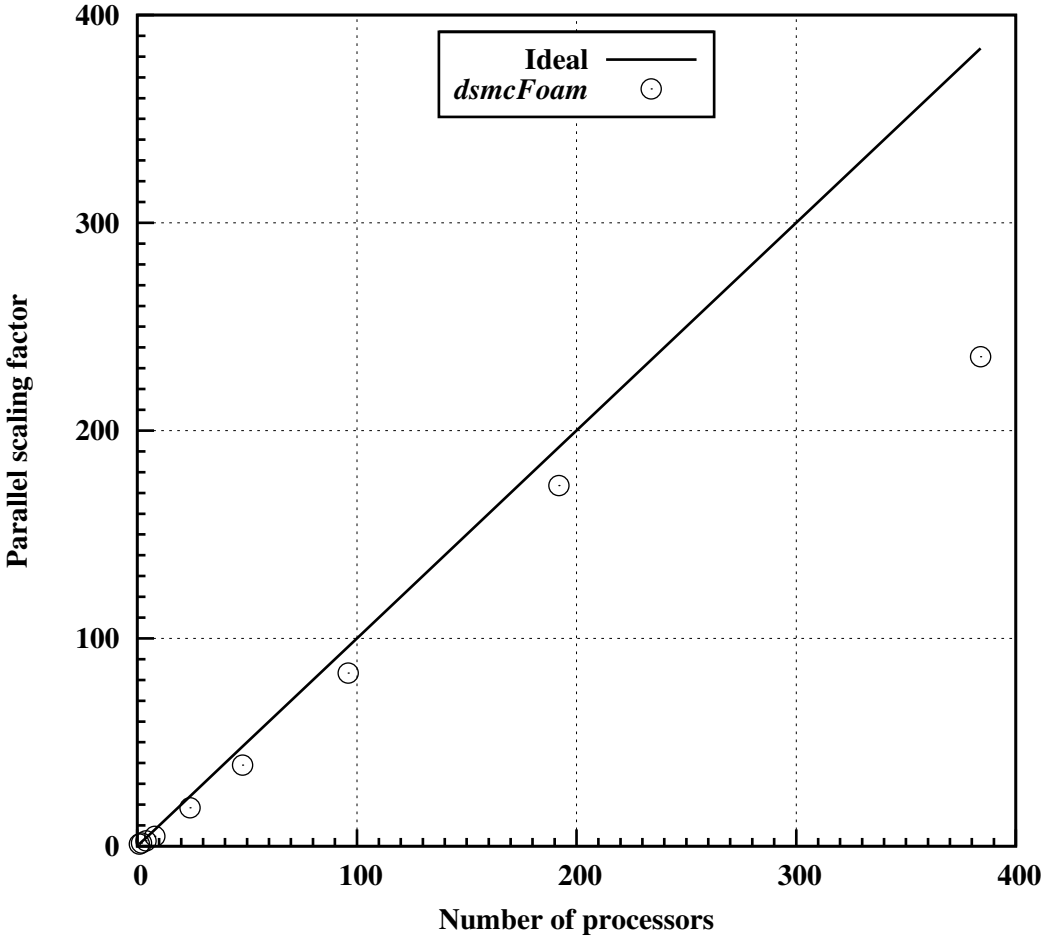

Figure 2.5: Parallel *dsmcFoam* efficiency test using one-hundred-million particles in one-million cells.

Further studies were carried out on the efficiency and they included the same

test case as before but with ten million cells and using one and two billion particles, their execution times are shown in figure 2.6. Also, this figure illustrates that *dsmcFoam* has achieved very good execution times using a large number of processors however, for one-billion particles using 1536 processors the simulation has become relatively inefficient and takes twice as long to execute than using 1000 processors.

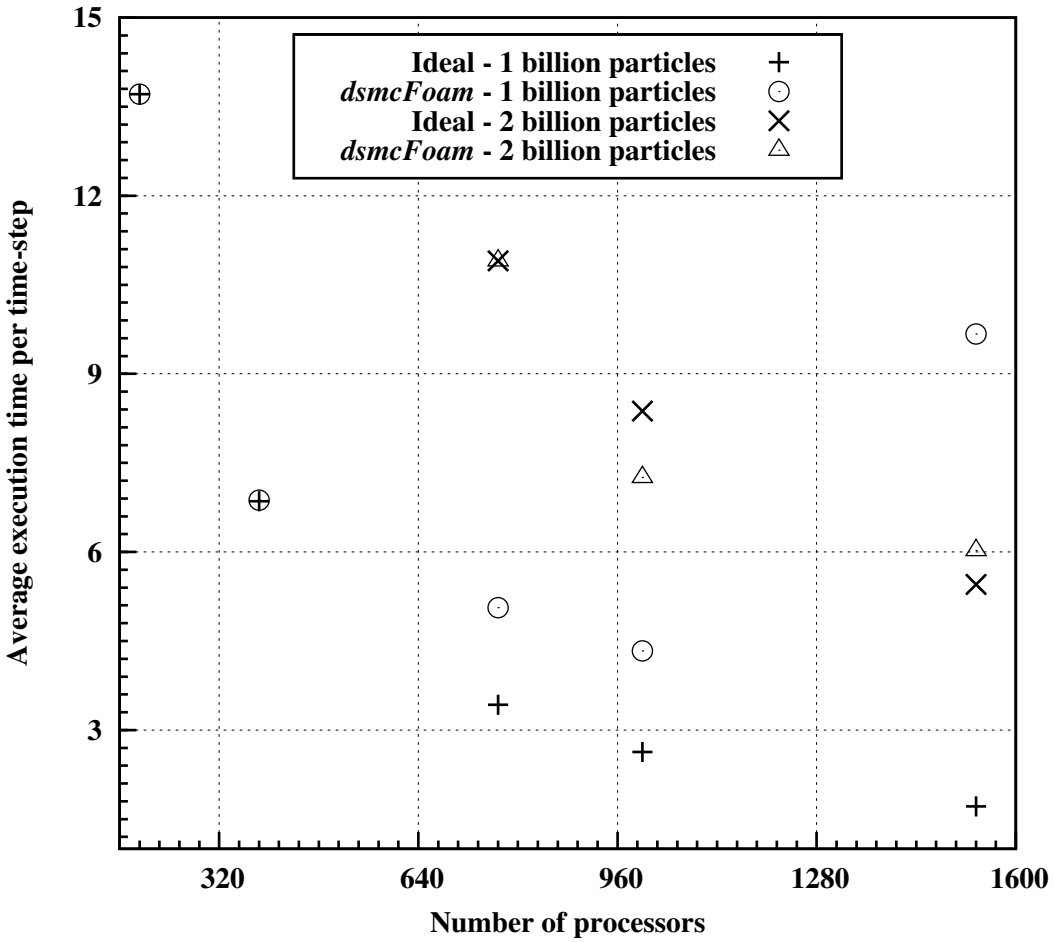

Figure 2.6: Parallel *dsmcFoam* efficiency tests using one-billion and two-billion particles in ten-million cells.

dsmcFoam domain decomposition for parallel processing

Effective computational domain decomposers, for parallel processing, are a vital tool for the efficiency of any solver in particular for computationally demanding techniques such as DSMC. In OpenFOAM [45] a domain decomposer splits up a computational domain into smaller sections. Each section is dealt with a separate processor and contains mesh cells and boundaries. The boundaries can either be between different sections or physical boundaries e.g. wall.

Previous decomposition methods used for *dsmcFoam* were either the *Simple* or *Scotch* techniques, available in OpenFOAM [45]. They are based on splitting the computational domain into sections by direction or by automatic decomposition, respectively. The *Scotch* technique splits the domain so that each processor has the same number of cells to work with whilst minimising processor boundaries and requires no geometric input.

In order to increase the computational efficiency of *dsmcFoam*, the author has developed and tested an extension to the *Scotch* decomposer. This new decomposer splits the domain so that each processor has the same number of particles to work with, meaning that processors are concentrated in regions of high number of particles, for example, in shock waves. To demonstrate this, the hypersonic cylinder shown in figure 2.7 presents the non-dimensionalised number density over the entire computational domain. This shows the number density is concentrated upstream of the cylinder from the bow-shock to the stagnation point, the new *Scotch* method can use information such as this to decompose the domain. This figure also illustrates the standard *Scotch* decomposition of the computational domain for eight processors, and this shows each processor has the same number of cells to work with. Figure 2.8 illustrates the decomposition of the domain with eight and sixteen processors using the new *Scotch* technique, and

for both many of the processors are concentrated close to the stagnation point.

To assess the new *Scotch* technique, which is open-source and available from the latest version of OpenFOAM [45], all three decomposers are tested on the 0° angle-of-attack planetary probe case discussed in the following chapter. The efficiency of all three decomposers, shown on figure 2.9, shows that the new *Scotch* technique has greatly increased the computational saving. Using the new *Scotch* method with 64 processors the computational time is reduced by ∼28% and ∼35% in comparison with the standard *Scotch* and *Simple* techniques, respectively.

2.4 Summary

This chapter has provided an introduction to DSMC and the methodology behind it. It has also briefly discussed the established DSMC codes used in the literature, and provided a description of the standard *dsmcFoam* code including its efficiency in parallel setups up to two-billion DSMC particles and 1536 processors - very good efficiency has been noticed. A new domain decomposition method for parallel *dsmcFoam* simulations was also presented and it was compared against the standard OpenFOAM *Scotch* and *Simple* decomposition techniques using the 0° angle-of-attack planetary probe case. The new decomposition technique reduced the computational time by at least ∼28% in comparison to the standard techniques.

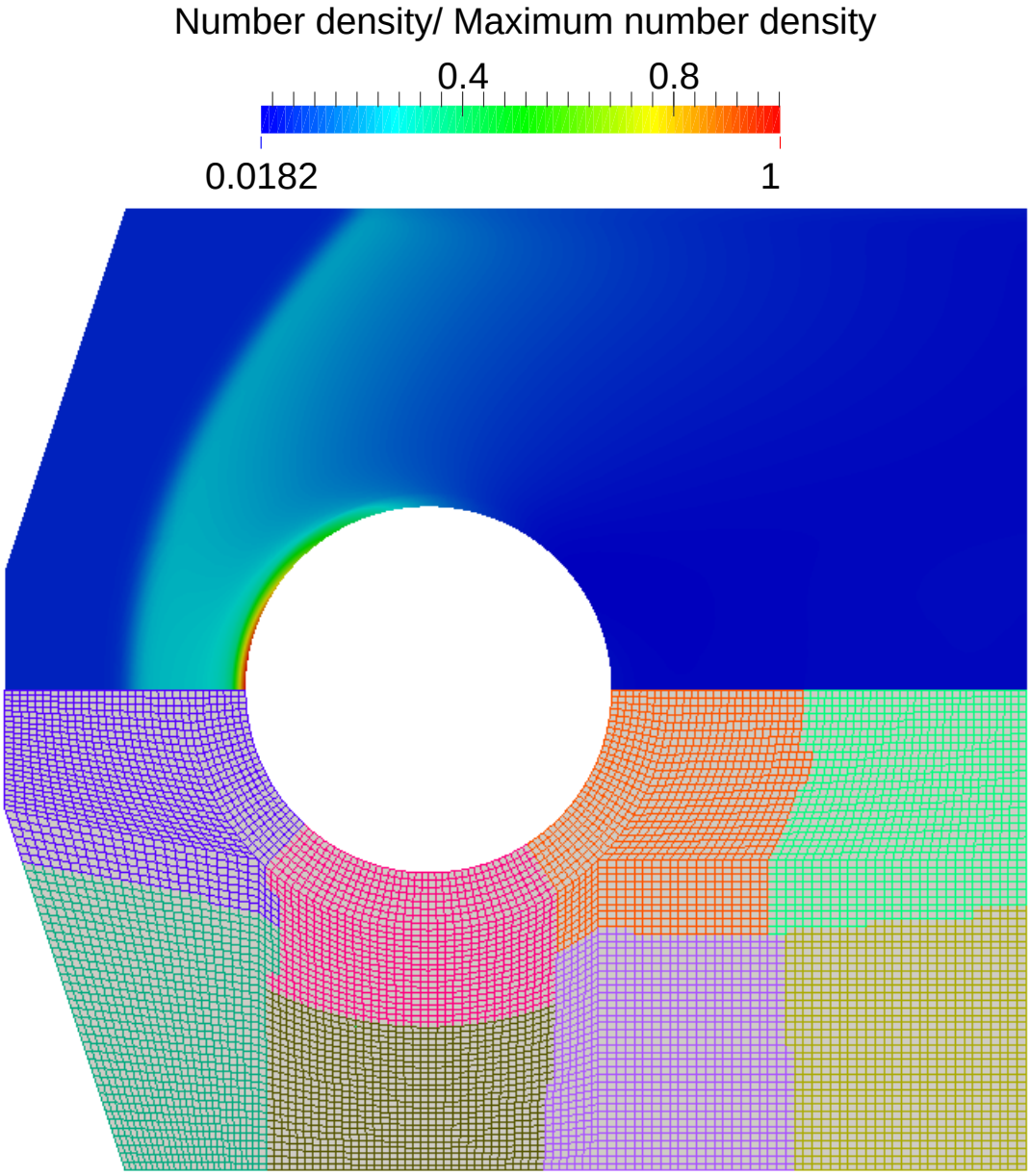

Figure 2.7: Non-dimensionalised number density (top) over the hypersonic cylinder and the domain decomposition (bottom) for eight processors using the standard *Scotch* technique, and each colour represents a different processor.

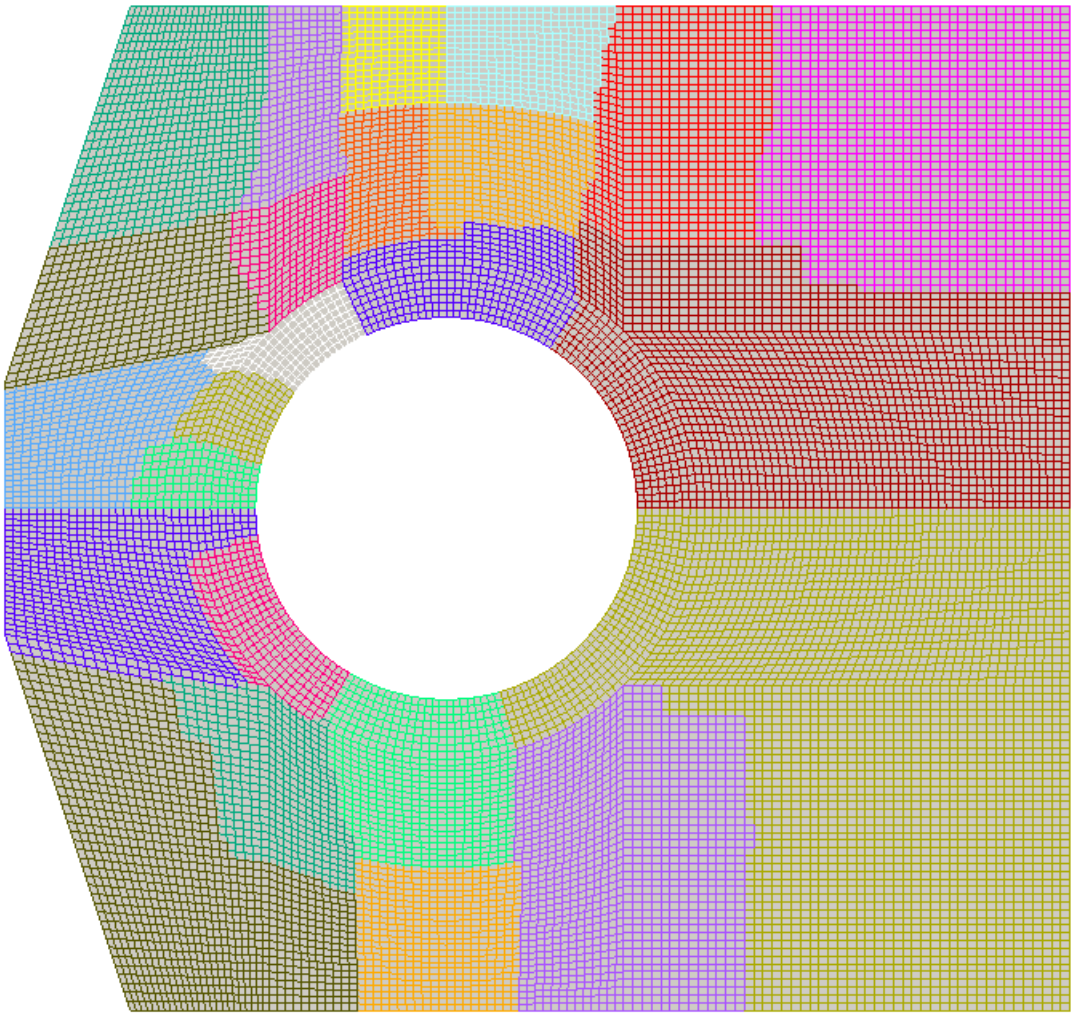

Figure 2.8: Domain decomposition for sixteen (top) and eight (bottom) processors using the new *Scotch* technique, and each colour represents a different processor.

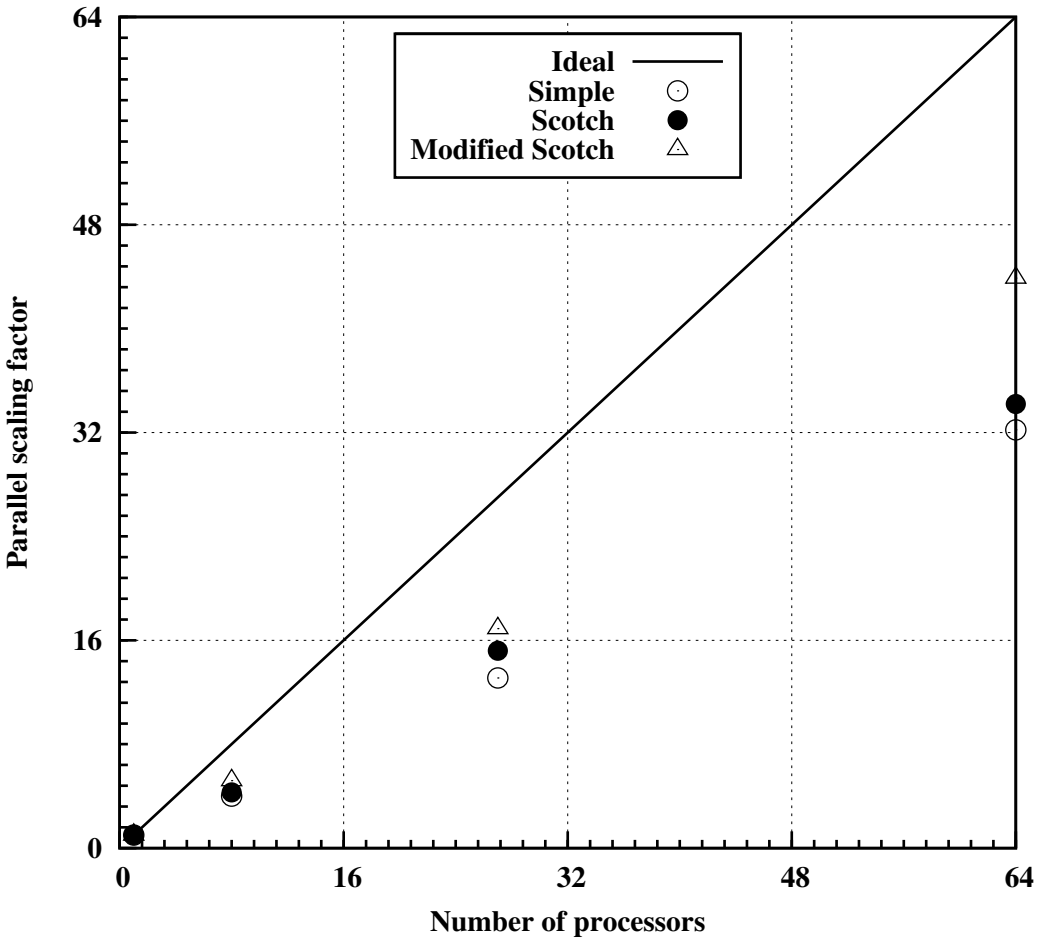

Figure 2.9: Parallel scaling factor comparisons of three decomposition techniques tested on the 0° angle-of-attack planetary probe case.

Chapter 3

Benchmarking *dsmcFoam*

This chapter describes the benchmarking of *dsmcFoam* with another DSMC code and experimental data available in the literature. Results of initial benchmark trials [94] have produced excellent agreement, when good DSMC practice has been followed, with both analytical solutions and other conventional DSMC codes. Appendix A expands on part of these trials but this chapter primarily focusses on benchmarking *dsmcFoam* against experimental data.

Most of the benchmark test cases in this chapter and Appendix A represent a substantial challenge to numerical models as they must capture flow physics including weak and diffuse shocks, boundary layer separation, flow recirculation, rapid expansion and re-compression, and shear layers with steep gradients of velocity, temperature and density. Moreover, numerical models for hypersonic, rarefied gas flows must also have the capability to capture shock-shock and shock-boundary layer interactions.

3.1 Comparisons of *dsmcFoam* with non experimental methods

In this section, *dsmcFoam* has been used to simulate the flow over the Apollo Command Module, and the results have been compared against the data of Moss *et al.* [1] that was produced using the DS3V program of Bird [99].

3.1.1 Hypersonic gas flow over the Apollo capsule

Simulations to investigate the effects of free-stream velocity on the aerodynamic forces over the Apollo Command Module were carried out at an altitude of 105 km and -25° angle-of-attack. Five free-stream velocities, ranging from 7.7 to 15 km/s shown in table 3.1, are used in this study and the highest velocity corresponds to the upper bounds of a Mars return mission. The Apollo capsule is built with a truncated spherical section, followed by a toroidal section, and then a conical section as shown in figure 3.1, while figure 3.2 shows the aerodynamic forces in the pitch plane. The flow parameters at an altitude of 105 km, along with numerical conditions used in the investigation are shown in tables 3.1 and 3.2, and [100]. The wall temperatures in table 3.1 are calculated [1] based on the minimum from either the heat transfer to the stagnation point based on free molecular radiative equilibrium theory or the radiative equilibrium temperature based on the stagnation point heating from the correlation of Sutton [101]. The hard sphere body-length global Knudsen number is 0.081, where the length scale is based on the maximum body diameter (D_b).

dsmcFoam results presented in figures 3.3, 3.4 and 3.5, for the five free-stream velocities, show that the aerodynamic coefficients change with increasing velocity. They change in a similar pattern to those subject to increasing rarefaction,

Velocity	Wall temperature
7680	871
8290	922
9600	1029
10759	1121
15000	1439

Table 3.1: Free-stream velocities and wall temperatures used in the simulations of the Apollo capsule at an altitude of 105 km.

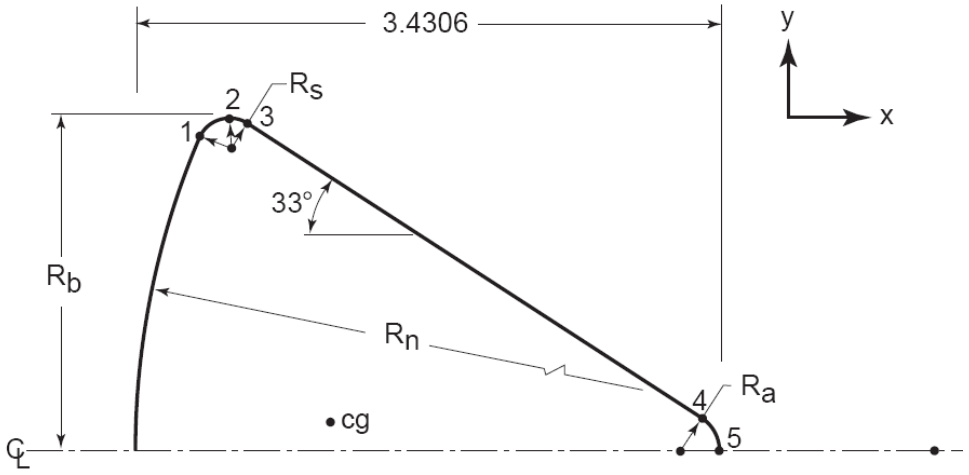

Location	x	y	s
1	0.3743	1.8368	1.8872
2	0.5543	1.9558	2.1158
3	0.6608	1.9242	2.2284
4	3.3254	0.1938	5.4056
5	3.3406	0.0000	5.6355
cg	1.1455	0.1600	-

D_b = 3.9116
R_b = 1.9558
R_n = 4.6939
R_s = 0.1956
R_a = 0.2311

Dimensions in m

Figure 3.1: Apollo Command Module configuration [1]. The center of gravity is denoted by cg.

presented by Moss *et al.* [1]. In other words, the coefficients of lift force and lift-to-drag (L/D) ratio decrease with increasing free-stream velocity and the coefficients of drag, and axial force increase with increasing velocity. Also, presented in figures 3.3, 3.4 and 3.5 are the Apollo capsule aerodynamic coefficients of Moss *et al.* [1], for several free-stream velocities, using the DS3V program of Bird [99]. Between *dsmcFoam* and Moss *et al.* [1], the lift-to-drag ratio and coefficients of

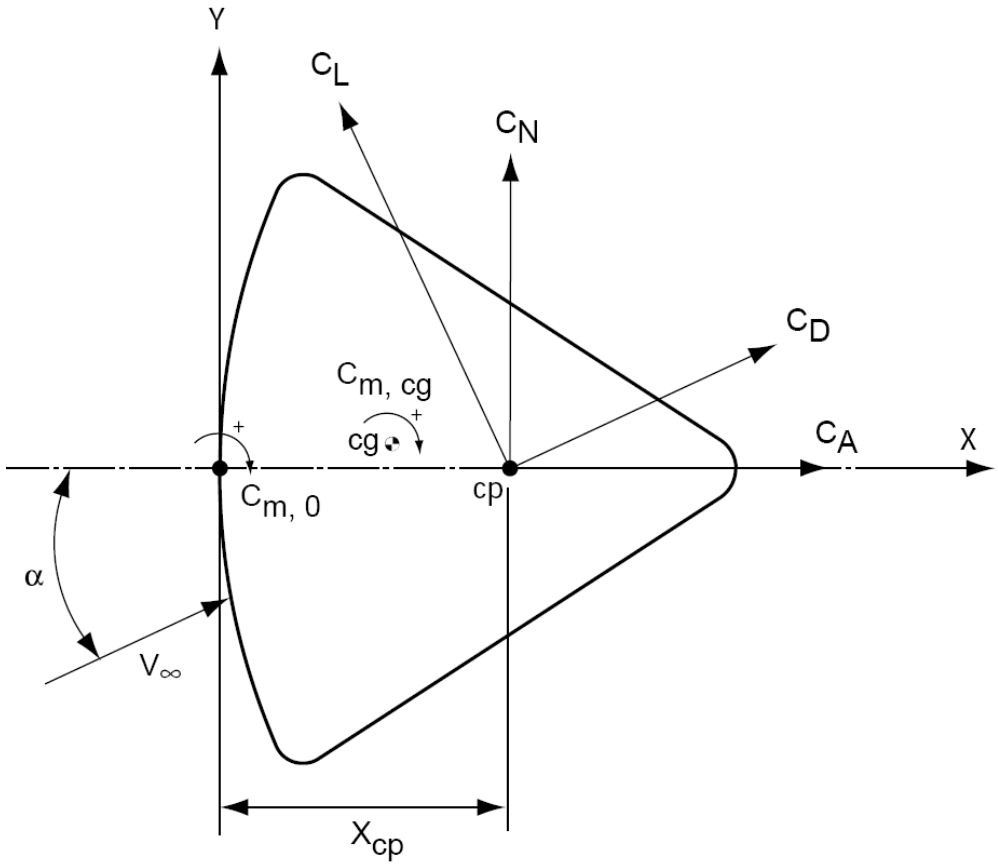

Figure 3.2: Pitch plane aerodynamic forces on the Apollo Command Module [1]. V_∞ only here, in this figure, represents the free-stream velocity.

lift force are in good agreement. The drag and axial force coefficients are also in good agreement, with a maximum difference of approximately four percent. The *dsmcFoam* simulations employed a mesh cell size and time-step of approximately a third of the mean free path and mean collision time, respectively. All *dsmcFoam* systems contained forty-seven million DSMC particles and the run-time was approximately thirty hours using thirty-two processors.

ρ_∞ [kgm^{-3}]	n$_\infty$ [m^{-3}]	T$_\infty$ [K]	O_2	N_2	O
2.364×10^{-7}	5.0947×10^{18}	208	0.15808	0.78319	0.05873

Table 3.2: Atmospheric composition and free-stream condition incurred by the Apollo capsule at an altitude of 105 km.

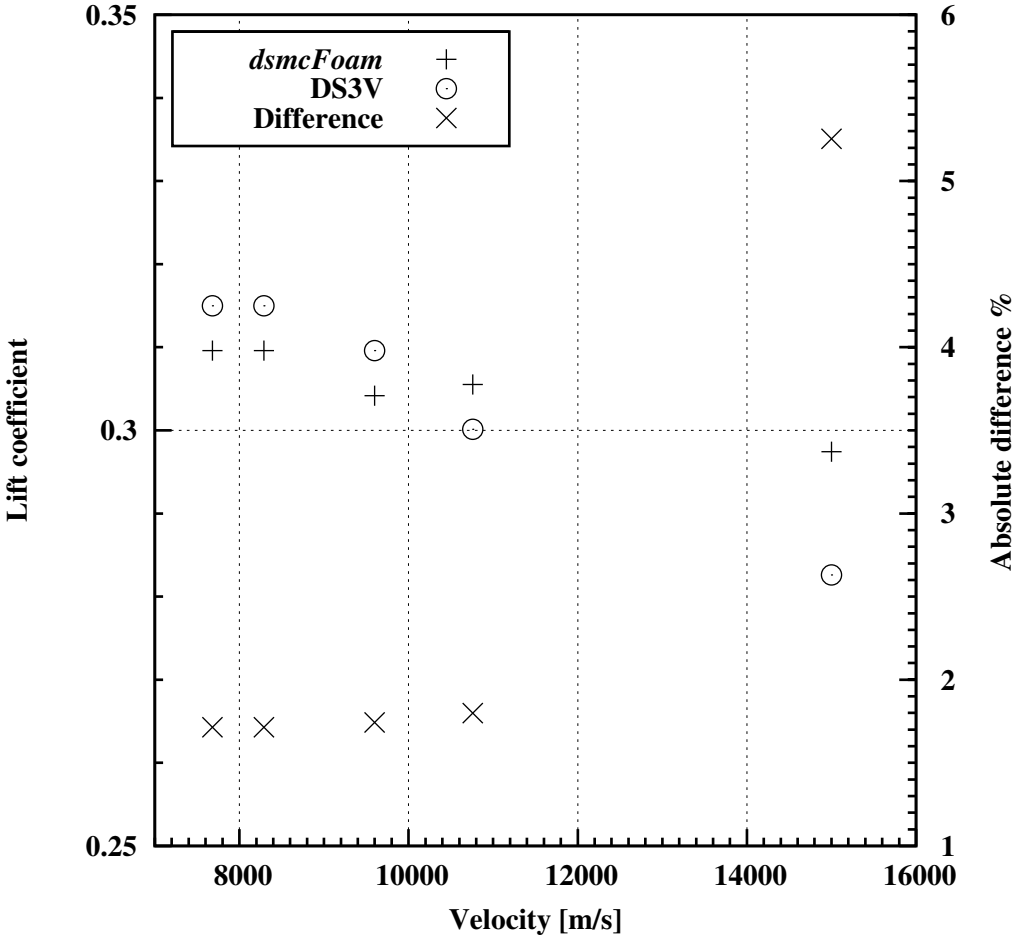

Figure 3.3: Comparison of *dsmcFoam* and DS3V calculations [1] of lift coefficients over the Apollo Command Module.

3.2 Comparisons of *dsmcFoam* with experimental methods

The author benchmarked and extended the range of applications of *dsmcFoam*. Some of the hypersonic test cases considered in the benchmarking were:

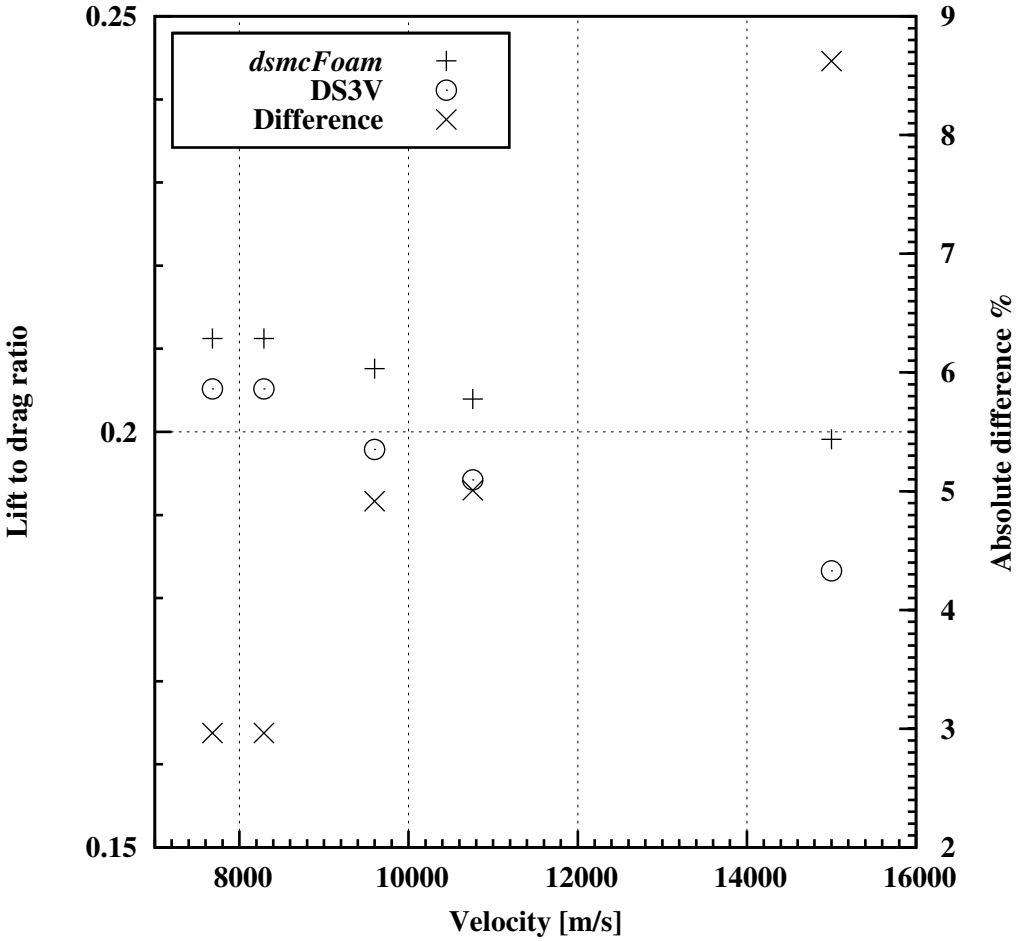

Figure 3.4: Comparison of *dsmcFoam* and DS3V calculations [1] of lift to drag ratios over the Apollo Command Module.

- Mach 20.2 Nitrogen flow over a planetary probe geometry,
- Mach 15.6 Nitrogen flow over a 25° and 55° bi-conic cylindrical object.

This section outlines these two test cases. For more information on the experimental methods and facilities, the reader is referred to [102–106].

Both bi-conic cylindrical object and planetary probe cases were modelled as three-dimensional quarter-section models whereas the Apollo capsule case is modelled as a three-dimensional half-section model because it has a non-zero angle-of-attack. All cases are run with symmetry boundary conditions, as *dsmcFoam* does not currently have an axi-symmetric capability. The bi-conic case takes

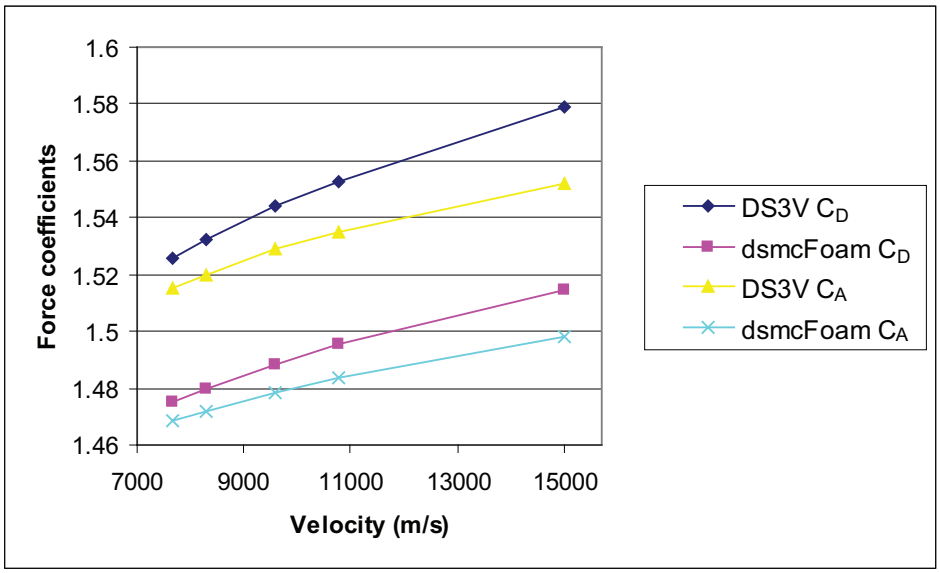

Figure 3.5: Comparison of *dsmcFoam* and DS3V calculations [1] of aerodynamic coefficients over the Apollo Command Module.

roughly ten times longer to resolve due to the complex nature of the flow physics, involving a shock-shock interaction, in this instance compared with the planetary probe. The bi-conic simulation took six days to resolve the flow features using sixty-four processors. In addition, *dsmcFoam* for both tests employed a time-step size of approximately a third of the mean collision time. The planetary probe and bi-conic tests employed a cell size of approximately a third of the mean free path and two times the mean free path, respectively. The system of the planetary probe test contained approximately eighty million DSMC particles - twelve million less than the bi-conic case.

3.2.1 Hypersonic gas flow over a planetary probe geometry

Allègre *et al.* [104–106] conducted experiments to observe density flowfields, surface heat transfer and drag coefficients in the SR3 low-density wind tunnel of the *Centre National de la Recherche Scientifique*, for Mach 20.2 flow of Nitrogen

over a planetary probe geometry with the forebody structure identical to the Mars Pathfinder probe. The planetary probe, considered as a test case model by AGARD[1], is a 70° spherically-blunted cone mounted on a cylindrical sting as shown in figure 3.6. The free-stream flow conditions, along with numerical parameters used in the *dsmcFoam* simulation, are shown in tables 3.3 and 3.4, and [100]. Three simulations were completed for the planetary probe at 0° angle-of-attack, as a different wall temperature was necessary for each study, as listed in table 3.4. Further investigations, using *dsmcFoam*, were conducted on the planetary probe at both positive and negative 10° angle-of-attacks, with the same free-stream environment and wall temperature as in tables 3.3 and 3.4, respectively. The body-length global Knudsen number of these three test cases is 0.067 - based on a variable hard sphere mean free path and the length scale is the radius of the forebody structure.

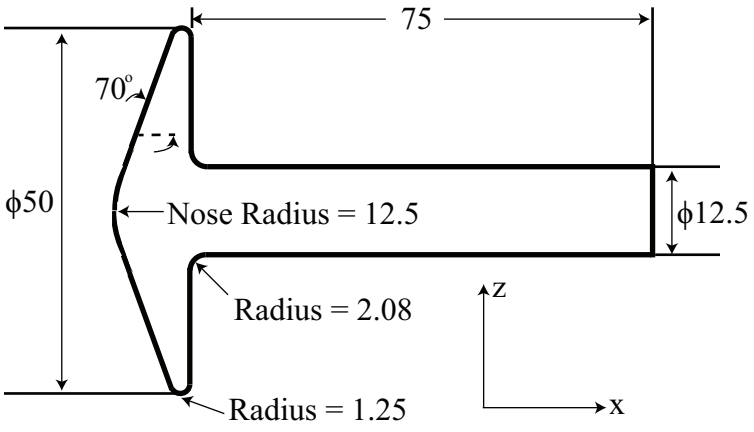

Figure 3.6: Planetary probe configuration. Dimensions are in millimetres. ϕ only here, in this figure, represents the diameter.

[1]Advisory group for aerospace research and development (AGARD) fluid dynamics panel and its working group 18.

Condition	Ma_∞	T_0 [K]	p_0 [bar]	ρ_∞ [gm^{-3}]
Planetary probe case	20.2	1100	3.5	0.0173

Table 3.3: Free-stream flow conditions of the planetary probe test case.

Investigation	Wall temperature [K]
Bi-conic case	297.2
Planetary probe case [104]: density flowfield	290
Planetary probe case [106]: drag coefficient	350
Planetary probe case [105]: heat transfer	300

Table 3.4: Surface temperatures of the planetary probe and bi-conic cylindrical object test cases.

Dimensionless density flowfields from the experimental observations of Allègre *et al.* [104] and results observed from *dsmcFoam* simulations are shown in figures 3.7, 3.8 and 3.9 for zero angle-of-attack, and both positive and negative 10° angle-of-attacks, respectively. The contour plots show a very good agreement between experimental and *dsmcFoam* observations. Upstream of the forebody, the bow shock structure has been particularly well captured and the maximum density occurs in the stagnation region directly in front of the object. And in this region, for the zero angle-of-attack planetary probe setup, the maximum relative density is approximately sixteen. The principal area of disagreement appears in the wake region immediately downstream of the forebody, adjacent to the sting. This section is occupied with extremely rarefied flow so, in order to sufficiently resolve the flowfield in this area, a coarser mesh is necessary to increase the number of collisions. Furthermore, if a coarser option is not possible, another method to adequately resolve the flowfield is to increase the number of particles in those regions, however this will increase the computational time.

Comparisons of surface heat transfer between experiment [105] and *dsmcFoam* are shown in figure 3.10 and very good agreement is perceived at the different

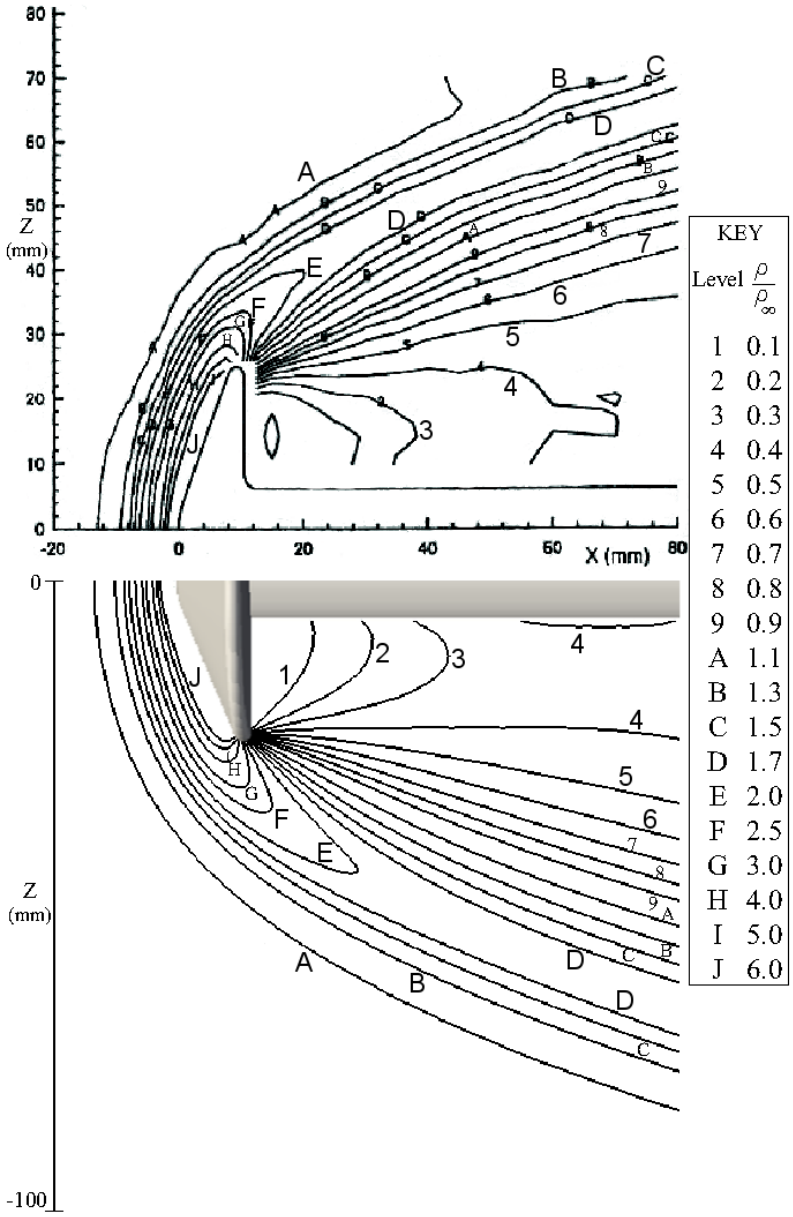

Figure 3.7: Planetary probe at zero angle-of-attack: comparison of experimental data (top) and *dsmcFoam* calculations (bottom) of dimensionless density profiles.

thermocouple positions. However, some differences occur in the extremely rarefied region - thermocouple positions 5 and 6. Furthermore, Allègre *et al.* [105] state that there is a degree of experimental uncertainty in this region due to the difficulty in precisely quantifying such low heat fluxes. Therefore it is not possible to establish the degree of numerical-experimental agreement in this region. The

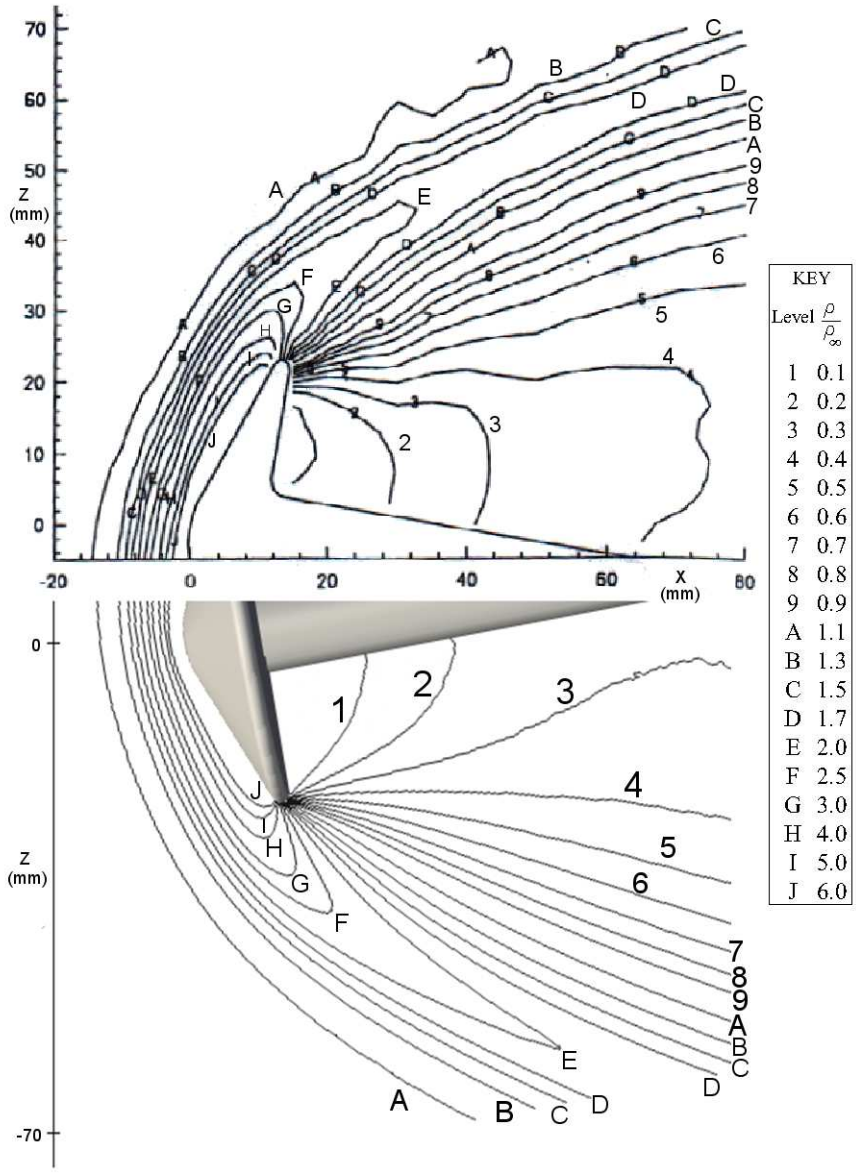

Figure 3.8: Planetary probe at 10° angle-of-attack: comparison of experimental data (top) and *dsmcFoam* calculations (bottom) of dimensionless density profiles.

experimental [106] drag coefficient, for the 0° angle-of-attack planetary probe, is 1.657 and in contrast, *dsmcFoam* predicted 1.89. Although this is a reasonable agreement, further grid, time-step and particle number sensitivity analyses are essential to improve the DSMC results. Time limitations prevented this from being included in the thesis and it is suggested as an area for future work.

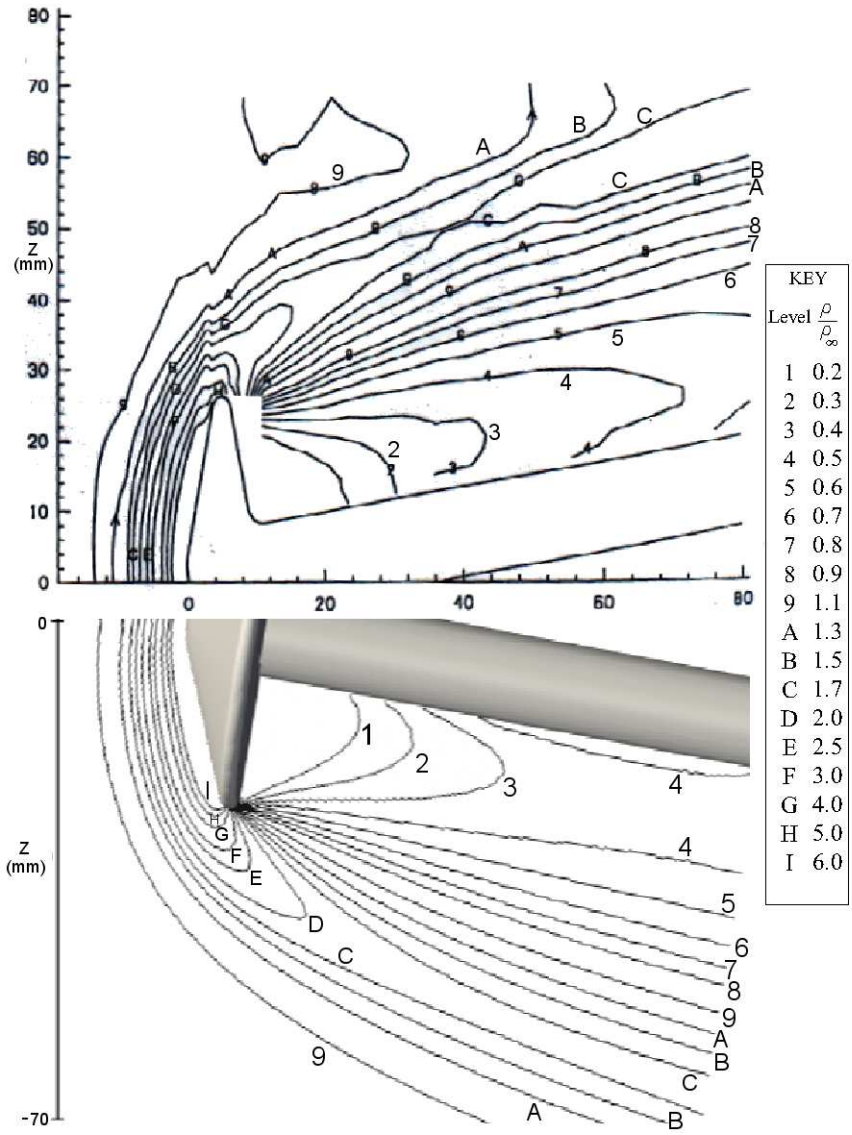

Figure 3.9: Planetary probe at -10° angle-of-attack: comparison of experimental data (top) and *dsmcFoam* calculations (bottom) of dimensionless density profiles

3.2.2 Hypersonic gas flow over a bi-conic cylindrical object

Experimental studies, to determine surface heating rates and pressure measurements, were completed by Holden *et al.* [102, 103] for Ma 15.6 flow of Nitrogen over a 25° and 55° bi-conic cylindrical configuration and this arrangement is shown in figure 3.11. The free-stream flow conditions and other parameters are presented

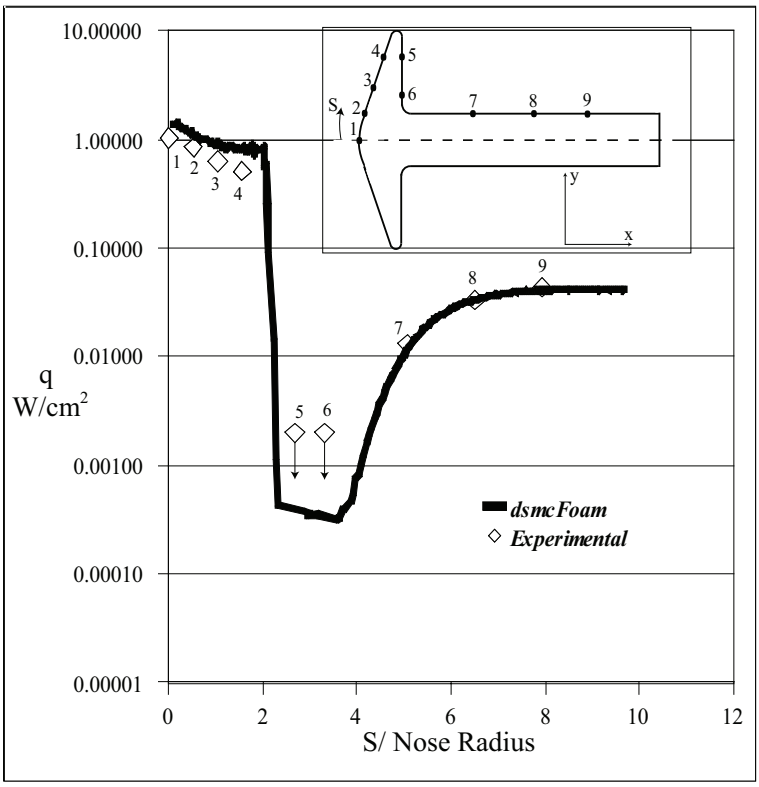

Figure 3.10: Comparison of experimental data and *dsmcFoam* calculations of surface heat transfer over the planetary probe at zero angle-of-attack.

in tables 3.5 and 3.4, and [100]. The body-length global Knudsen number of this test case is 0.005 - based on a variable hard sphere mean free path and the length scale is the radius of the 25° section.

Condition	Ma_∞	T_∞ [K]	p_∞ [Nm^{-2}]	ρ_∞ [gm^{-3}]
Bi-conic case	15.6	42.61	2.23	0.1757

Table 3.5: Free-stream flow conditions of the planetary probe and bi-conic cylindrical object test cases.

Experimental investigations [102, 103] of surface pressure and heating rates on the bi-conic cylindrical surface are compared, in figures 3.12 and 3.13, respectively with the results acquired from *dsmcFoam*. The surface pressure results, obtained from *dsmcFoam*, show a reasonable agreement with the experiment. The agreement is less apparent for the heat flux on the 25° section of the bi-conic cylindrical

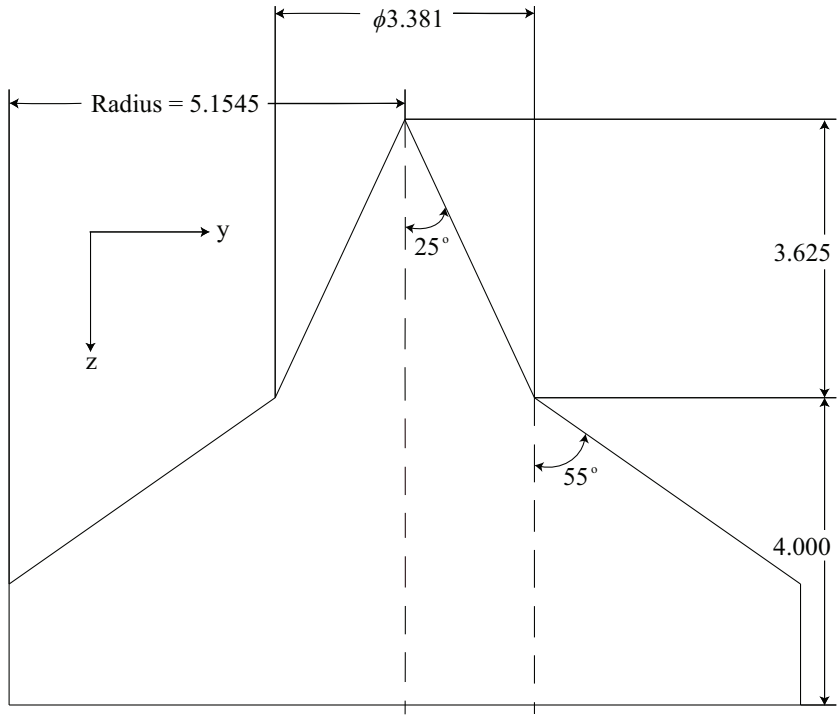

Figure 3.11: 25° and 55° bi-conic cylindrical object configuration. Dimensions are in inches.

body but greatly improves on the 55° section. At the approximate location in between the two conical sections, around z $\approx$ 0.1 m, a shock-shock interaction occurs which produces a relatively huge surface heating rate on the surface with *dsmcFoam* in comparison to the experiment. To sufficiently determine the surface heating rate in the shock-shock interaction a very refined mesh is mandatory in this region. Further DSMC studies will reduce the noise in the surface heating rate and pressure values by using more simulated particles and cells to pick up the large gradients in flow accurately. Once more, time limitations prevented this from being included in the thesis and it is suggested as an area for future work.

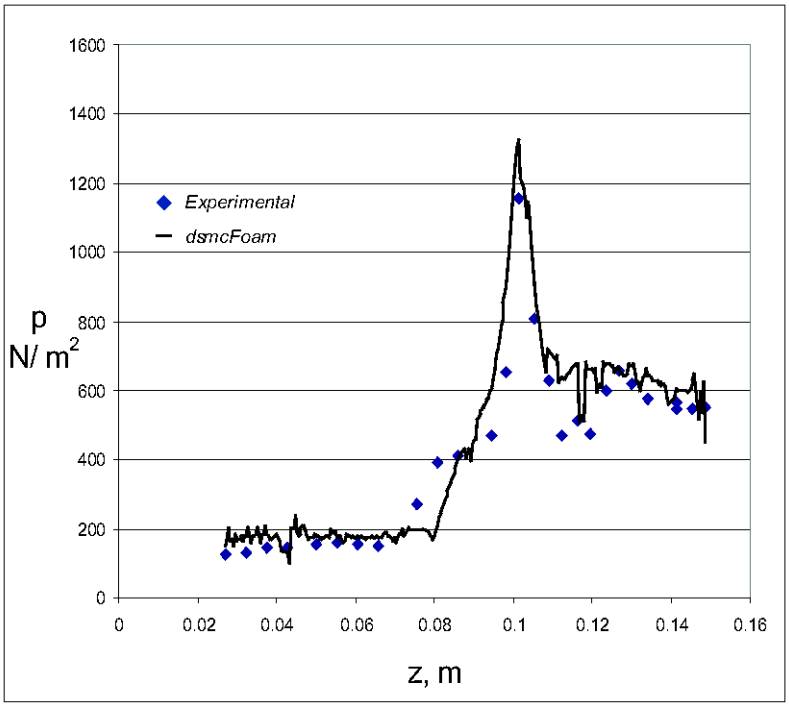

Figure 3.12: Comparison of experimental data and *dsmcFoam* calculations of surface pressure over the bi-conic cylindrical object.

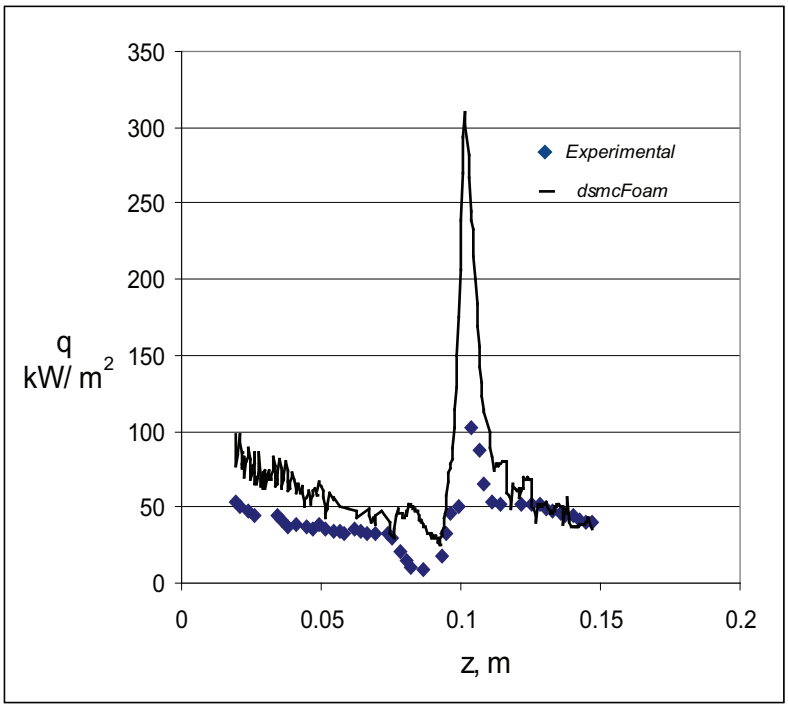

Figure 3.13: Comparison of experimental data and *dsmcFoam* calculations of surface heat transfer over the bi-conic cylindrical object.

3.3 Summary

This chapter has presented benchmark trials of an open-source DSMC code called *dsmcFoam* that has the ability to easily handle arbitrary, complex three-dimensional geometries. Results for initial benchmark trials [94] showed good agreement with analytical solutions and other conventional DSMC codes. This chapter and Appendix A presented *dsmcFoam* comparisons with analytical solutions, other DSMC codes and experimental data. When good DSMC practice was employed in *dsmcFoam*, the results were in excellent agreement with the other sources mentioned before. The largest differences noticed was concerning the surface heat transfer over the bi-conic cylindrical object, and it is believed this will be resolved by considering energy exchange with the vibrational mode, as well as the rotational mode in the simulation. Also, further work is required to consider the influence that different numerical parameters (e.g. altering the cell size, time step and molecules per particle) have on the simulations.

Chapter 4

Transient adaptive sub-cell module

The DSMC technique can easily calculate poor microscopic phenomena if the intrinsic constraints of the method are not followed and can lead into inaccurate macroscopic data being determined. One of the main constraints is the cell volume, as the collision pairs are constrained to this space. If the cell volume is large this has a direct impact on the accuracy of the collisions as it can force collisions between particles that have a very large separation distance. Good DSMC practice [2] suggests the cell size has to be a fraction of the local mean free path. In addition, it is recommended [2, 4] to set the time-step size to a fraction of the mean collision time to ensure several collisions occur in a cell.

This chapter presents the importance of a cell volume in determining collision pairs. It also presents a transient adaptive sub-cell (TASC) routine, implemented in *dsmcFoam*, and an extension to the 8 sub-cell method for the purpose of selecting collision partners in close proximity to each other. The 8 sub-cell method splits up a sampling cell into 8 sections/ sub-cells and particles are only chosen for collision if they are in the same sub-cell. And in the case if there is only

one paricle in a sub-cell the collision partner is chosen from the entire sampling cell. The TASC technique can produce more or less or equal to eight sub-cells in a computational cell and the number of sub-cells produced by this method is not restricted. However, it does not guarantee nearest-neighbour collisions as particles close to each other but separated by cell boundaries cannot collide. This is also a restriction in the conventional eight sub-cell method and other methods such as the 'virtual sub-cell' method of LeBeau [47]. The 'virtual sub-cell' method determines the distances between particles explicitly and the particles closest to each other are only selected for collision, this method was introduced in the DAC method [47, 107] and has since been included in DS2V [2]. Although this procedure is not as expensive as it seems for around thirty particles or lower in a cell it is more expensive than the conventional eight sub-cell method as it determines the distances between all particles and the randomly chosen particle in a cell to find the minimum distance. Macrossan [108] has recently improved the computational efficiency of the 'virtual sub-cell' method by determining the expected minimum distance (d_n) for a particle in a cell to search within for its nearest neighbour and it is termed the 'pseudo sub-cell' method. From statistical trials of three-dimensional cells of various aspect ratios, Macrossan has found the expected minimum distance to the nearest neighbour is

$$F_{VSC} d_n = \frac{0.746}{N_{pic}^{0.383}} V_{cell}^{\frac{1}{3}}, \tag{4.1}$$

where N_{pic} is the number of particles in a cell and V_{cell} is the volume of the cell. Macrossan also sets a factor F_{VSC} to compromise between accuracy and speed of the simulation, for example using $F_{VSC} = 1.1$ [108] the accuracy might be reduced and the simulation might run faster in comparison to a factor of 1 if the particles are not within the expected minimum distance. In addtion, in the

situation where the factor is set to 1 and the particles are not within the expected minimum distance then an exhaustive search is conducted of all particles in the cell to find the closest collision pair.

The TASC method discussed in this chapter allows the user to choose the desired number of particles per sub-cell (PPSC) and therefore implicitly allows a particle to collide with another close by but it may not be the immediate nearest. Also, with the TASC routine the cell size can be greater than the recommended third of the mean free path. One of the test cases considered in this chapter has cell dimensions of approximately two mean free paths and the microscopic accuracy is not affected as long as the TASC routine is used with the correct criteria. For cell sizes larger than two mean free paths the ability to capture steep macroscopic gradients may be reduced. One possible method to resolve the macroscopic accuracy, in areas of interest, is discussed in section 4.1. Also, by reducing the number of cells the computational run-time and memory is reduced in addition, the memory is reduced for post-processing too as less sampling cells are involved.

4.1 Introduction

As discussed in chapter 2, sub-cells are employed to promote nearest neighbour collisions. However, it is important to emphasise that they do not guarantee it as the separation distance between particles does not depend upon the selection of collision pairs but solely on the volume of the cell and sub-cell. In addition, particles that are close to each other, and those separated by cell or sub-cell boundaries cannot be considered as collision pairs. Only particles in the same sub-cell can be selected for collision. However, in the special case of only one particle in a sub-cell, then this single particle may collide with any other particles

in the entire cell according to the conventional eight sub-cell method. By using sub-cells the time of computations is reduced in comparison to looping over all particles and figuring out exactly what the closest particle to another is.

Furthermore, Bird's code [4] uses a fixed number of particles per sampling cell and in the latest version a transient mesh adaption is possible [109]. However this was tested on structured grids and has recently been included [5] into a parallel three-dimensional DSMC code called PDSC [110] to be utilised with unstructured grids and has now been implemented into *dsmcFoam* by the author for structured or unstructured two- or three-dimensional systems.

The use of a TASC module in DSMC ensures good quality collisions are enforced in the simulations. This applies even for coarse grids, where the cell dimensions are larger than a third of the mean free path - a standard recommendation of the cell size for good DSMC practice. However, the resolution of macroscopic gradients may be adversely affected. Such effects may be reduced in specific areas of interest by using the mesh refinement in OpenFOAM utilities such as *snappyHexMesh* [45]. Figure 4.1 shows a mesh created by *snappyHexMesh* of the Apollo Command Module, benchmarked in section 3.1.1, and it shows an increased refinement level through the shock. This extra refinement is produced by initially creating an iso-surface of a field property, such as the translational energy through the shock, then exporting the surface as a triangulated mesh (.obj, .VTK, .stl) and using the surface as a refinement zone in *snappyHexMesh*. In addition, this refinement procedure is normally undertaken after a *dsmcFoam* simulation using the conventional eight sub-cell method in order to refine the mesh according to the local mean free path calculated from the *dsmcFoam* results. The simulation is then re-run with the new mesh and this process is repeated until the mesh has cells that meet good DSMC practice. However, this procedure has the potential to be very computationally intensive and cumbersome.

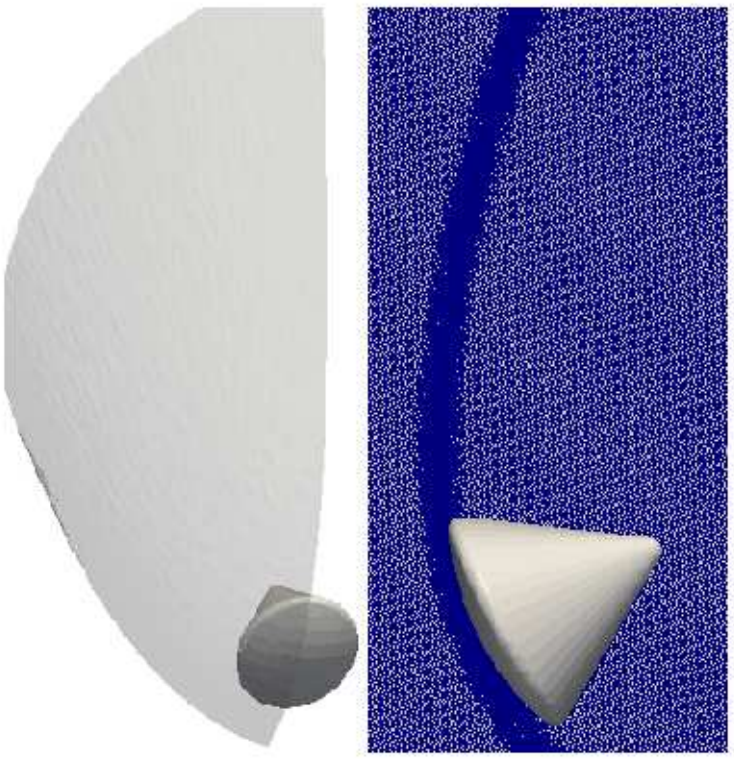

Figure 4.1: The iso-surface (left) of the shock, around the Apollo Command Module, is used by *snappyHexMesh* to refine the mesh (right) to either meet good DSMC practice or to resolve the macroscopic gradients.

Two TASC routines are presented in the following sections, the standard and improved TASC techniques. The improved TASC routine inherits all of the features of the standard TASC routine but with an extra feature that occurs when there is only one particle in a sub-cell. The standard TASC technique looks in the entire cell for a collision partner when there is only one particle in a sub-cell, but the improved TASC technique does a search for collision partners close by - it does this by increasing the volume of the sub-cells until there is one or more possible collison partners. The standard and improved TASC techniques are different to the literature [5]. The main difference is in the literature a collision partner may be found in the adjacent sub-cells immediately next to the sub-cell containing one particle. And if the collision partner can not be found in the adjacent sub-cells it is then looked in the sampling cell. The other difference is

in the literature the TASC framework is for two-dimensional problems, whereas the standard and improved TASC techniques discussed in this thesis has been built with a three-dimensional framework. In addition, the three-dimensioanal framework works for two-dimensional problems too.

The *dsmcFoam* collision rates of both standard and improved TASC routines for a range of PPSC are verified, based on the setup and some of the test conditions in section A.1, with an analytical collision rate based on equation A.2. The comparisons are in very good agreement and are illustrated in tables 4.1, 4.2 and 4.3 for Nitrogen at 200, 500 and 800 K, respectively. This provides verification of the implementation of both TASC techniques.

PPSC	Standard TASC collision rate $[s^{-1}m^{-3}]$	Improved TASC collision rate $[s^{-1}m^{-3}]$	Standard TASC difference [%]	Improved TASC difference [%]
2	1.61761×10^{24}	1.61890×10^{24}	-0.05751	0.02178
3	1.61745×10^{24}	1.61756×10^{24}	-0.06735	-0.06101
4	1.61747×10^{24}	1.61731×10^{24}	-0.06670	-0.07635
5	1.61743×10^{24}	1.61740×10^{24}	-0.06898	-0.07101
6	1.61728×10^{24}	1.61761×10^{24}	-0.07804	-0.05752
7	1.61755×10^{24}	1.61748×10^{24}	-0.06170	-0.06579
8	1.61742×10^{24}	1.61750×10^{24}	-0.06937	-0.06435
9	1.61747×10^{24}	1.61736×10^{24}	-0.06658	-0.07298
10	1.61742×10^{24}	1.61751×10^{24}	-0.06921	-0.06395
15	1.61735×10^{24}	1.61752×10^{24}	-0.07377	-0.06313
20	1.61746×10^{24}	1.61746×10^{24}	-0.06716	-0.06716
30	1.61741×10^{24}	1.61741×10^{24}	-0.07001	-0.07001
40	1.61763×10^{24}	1.61736×10^{24}	-0.07322	-0.07322

Table 4.1: *dsmcFoam* collision rates of Nitrogen, in an adiabatic box at 200 K, using the standard and improved TASC routines. The corresponding analytical collision rate is 1.61854×10^{24} $s^{-1}m^{-3}$. The last two columns represent the percentage difference of the standard and improved TASC routine collision rates with the analytical rate, and is calculated using equation A.6.

PPSC	Standard TASC collision rate $[s^{-1}m^{-3}]$	Improved TASC collision rate $[s^{-1}m^{-3}]$	Standard TASC % error	Improved TASC % error
2	2.05262×10^{24}	2.05249×10^{24}	-0.06465	-0.07081
3	2.05262×10^{24}	2.05268×10^{24}	-0.06456	-0.06188
4	2.05271×10^{24}	2.05271×10^{24}	-0.06021	-0.06024
5	2.05279×10^{24}	2.05275×10^{24}	-0.05620	-0.05809
6	2.05263×10^{24}	2.05266×10^{24}	-0.06403	-0.06267
7	2.05268×10^{24}	2.05259×10^{24}	-0.06181	-0.06618
8	2.05271×10^{24}	2.05260×10^{24}	-0.06002	-0.06559
9	2.05251×10^{24}	2.05264×10^{24}	-0.07013	-0.06360
10	2.05259×10^{24}	2.05253×10^{24}	-0.06593	-0.06915
15	2.05256×10^{24}	2.05260×10^{24}	-0.06763	-0.06559
20	2.05255×10^{24}	2.05262×10^{24}	-0.06783	-0.06450
30	2.05244×10^{24}	2.05244×10^{24}	-0.07353	-0.07353
40	2.05253×10^{24}	2.05253×10^{24}	-0.06879	-0.06879

Table 4.2: *dsmcFoam* collision rates of Nitrogen, in an adiabatic box at 500 K, using the standard and improved TASC routines. The corresponding analytical collision rate is 2.05395×10^{24} $s^{-1}m^{-3}$. The last two columns represent the percentage difference of the standard and improved TASC routine collision rates with the analytical rate, and is calculated using equation A.6.

4.2 Standard TASC routine

This section outlines the standard TASC routine implemented in *dsmcFoam* and validates this method using the hypersonic cylinder test case, introduced by Lofthouse *et al.* [111] in 2006 and later used by Bird [2] for benchmark studies.

4.2.1 Standard TASC routine: background

Consider an arbitrary three-dimensional cell, from a typical DSMC computational mesh, that is enclosed by a bound-box with sides parallel or perpendicular to each direction of the global axis system as shown in figure 4.2. The length of the bound-box is l_x, l_y and l_z in the x-, y- and z-direction, respectively. The bound-box is always cuboid and it can accommodate a cell which has either been

PPSC	Standard TASC collision rate $[s^{-1}m^{-3}]$	Improved TASC collision rate $[s^{-1}m^{-3}]$	Standard TASC % error	Improved TASC % error
2	2.31946×10^{24}	2.31931×10^{24}	-0.06316	-0.06919
3	2.31955×10^{24}	2.31958×10^{24}	-0.05893	-0.05767
4	2.31953×10^{24}	2.31931×10^{24}	-0.06000	-0.06957
5	2.31949×10^{24}	2.31943×10^{24}	-0.06172	-0.06438
6	2.31950×10^{24}	2.31949×10^{24}	-0.06130	-0.06186
7	2.31960×10^{24}	2.31949×10^{24}	-0.05703	-0.06148
8	2.31965×10^{24}	2.31962×10^{24}	-0.05476	-0.05614
9	2.31949×10^{24}	2.31953×10^{24}	-0.06177	-0.06000
10	2.31938×10^{24}	2.31958×10^{24}	-0.06645	-0.05792
15	2.31946×10^{24}	2.31937×10^{24}	-0.06294	-0.06688
20	2.31933×10^{24}	2.31933×10^{24}	-0.06833	-0.06833
30	2.31965×10^{24}	2.31965×10^{24}	-0.05465	-0.05465
40	2.31951×10^{24}	2.31951×10^{24}	-0.06077	-0.06077

Table 4.3: *dsmcFoam* collision rates of Nitrogen, in an adiabatic box at 800 K, using the standard and improved TASC routines. The corresponding analytical collision rate is 2.32092×10^{24} $s^{-1}m^{-3}$. The last two columns represent the percentage difference of the standard and improved TASC routine collision rates with the analytical rate, and is calculated using equation A.6.

built up by *blockMesh*, *snappyHexMesh* or a mesh from another source that has been transferred into the OpenFOAM style. The number of sub-cells (N^{sc}) for the bound-box of the cell is,

$$N^{sc} = \frac{nV_{bb}}{n_{PPSC}}, \tag{4.2}$$

where n is the number density, n_{PPSC} is the desired number of PPSC specified at the start of the simulation and the bound-box volume (V_{bb}) is,

$$V_{bb} = l_x \times l_y \times l_z. \tag{4.3}$$

The total number of sub-cells in the bound-box is then re-determined to form cuboid sub-cells that have exactly the same volumes. To do this, an initial as-

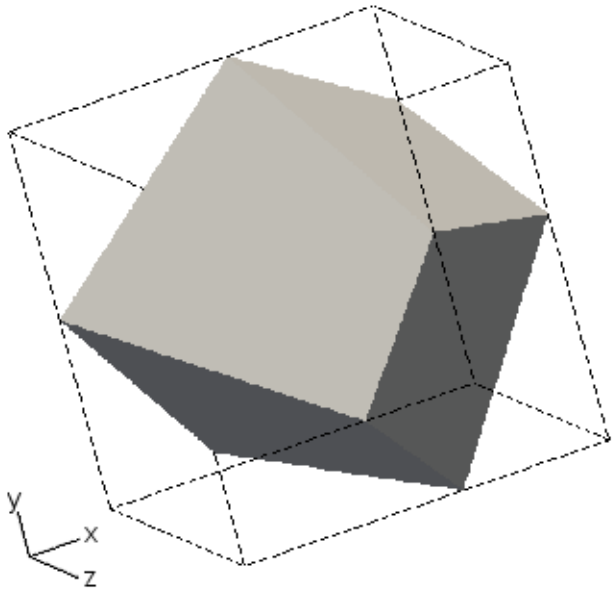

Figure 4.2: A typical mesh cell within a bound-box. The bound-box is represented by the dotted black lines and the axis represents the global axis.

sumption is made of the bound-box being cubic and this is done to get a rough estimate of the sub-cell lengths (Δl),

$$\Delta l = \sqrt[3]{\frac{Vbb}{N^{sc}}}. \tag{4.4}$$

Then the number of sub-cells in each direction (N_i^{sc}), using the nearest integer function, is roughly,

$$N_i^{sc} = nint\left(\frac{l_i}{\Delta l}\right), \tag{4.5}$$

where N_i^{sc} is a natural number and $i = x, y, z$. The lengths of the sub-cells in each direction are re-calculated as,

$$\Delta l_i = \frac{l_i}{N_i^{sc}}, \tag{4.6}$$

and the total number of sub-cells as,

$$N^{sc} = \frac{l_x}{\Delta l_x} \times \frac{l_y}{\Delta l_y} \times \frac{l_z}{\Delta l_z}. \tag{4.7}$$

The sub-cells are generated, in the entire bounding box, with sides parallel or perpendicular to each direction of the global axis system as shown in figure 4.3. This figure also presents the problem in generating sub-cells, that is some sub-cells may be generated outside of the sampling cell. This only applies to a sampling cell that is not a cuboid, or a cuboid with sides not parallel or perpendicular to each direction of the global axis system. Therefore, it is preferred but not important, to use meshing techniques and generators such as *snappyHexMesh* to develop a mesh for the TASC technique. An example of a preferred mesh produced by *snappyHexMesh* is shown in figure 4.4 - the cells close to the surface of this mesh can be improved by using the *layers* function in *snappyHexMesh* without sacrificing majority of the cubic cells. In section 4.3.3 two different mesh configurations are compared for one of the test cases used to benchmark the adaptive sub-cell method in order to determine the effect of the mesh on the results.

To deal with transient type systems, the sub-cells are constructed at every user defined time-step - they can be constructed from every time-step to only generated once throught the entire simulation. Although the construction of sub-cells is not expensive, for steady-state type systems sub-cells do not have to be generated every time-step. A suggested approach to determine the number of time-steps in between constructing sub-cells is to calculate it based on how many time-steps is required to reach steady-state from initial conditions. If it requires many time-steps then the re-construction of sub-cells should be done frequently as the system can reach steady-state sooner. Although it is not very important

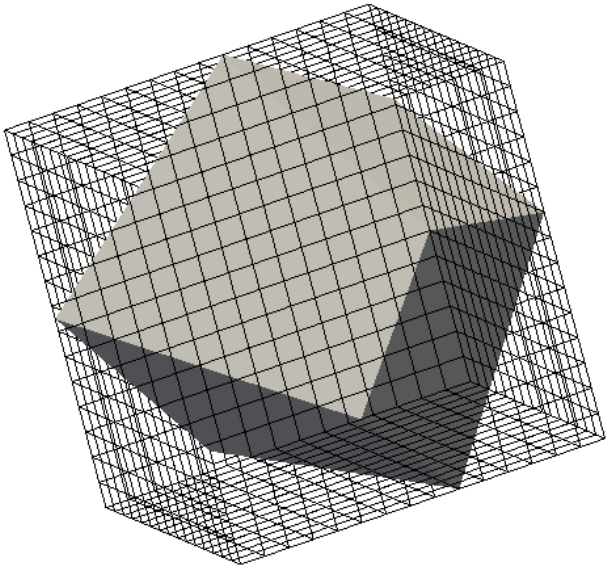

Figure 4.3: Mesh cell with 3375 sub-cells. The sub-cells are represented by the black lines.

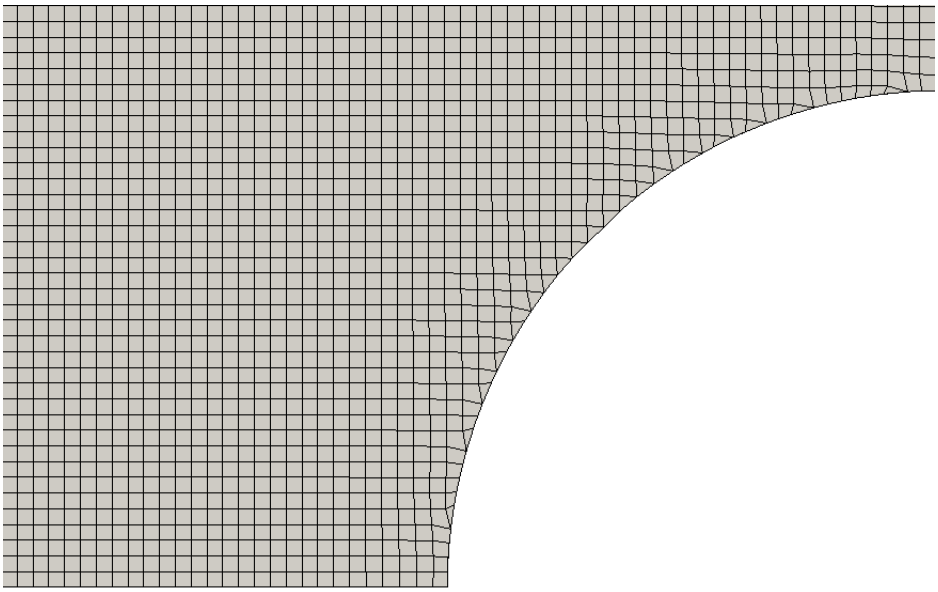

Figure 4.4: Preferred mesh for the TASC routine.

to re-construct it frequently as steady-state is independent of when the sub-cells are re-constructed, it will just take longer to reach that state using sub-cells that are re-constructed less often. However, the number of time-steps required to reach steady-state for a certain system may be a challenge to determine before

running the actual simulation. In particular, if the number of time-steps between creating sub-cells is greater than one then it may take more time-steps to reach steady-state as opposed to generating sub-cells every time-step. Also, the final steady-state results, based on long sampling times, are independent of the time-steps defined between the construction of sub-cells. During steady-state some systems, at a microscopic level, will not change a great deal over time therefore in those systems sub-cells do not have to be frequently generated.

Once the sub-cells have been generated, a particle is then assigned to a particular sub-cell using equations 4.8 and 4.9. The sub-cell index for an arbitrary particle in a cell is,

$$j = j_x + j_y N_x^{sc} + j_z N_x^{sc} N_y^{sc}, \tag{4.8}$$

and j_i with the use of the floor function represents the bin in each direction,

$$j_i = \left\lfloor \frac{1}{\Delta l_i} \left(r_{pp} - r_{bb}^{cp} \right) \cdot \hat{e}_i \right\rfloor . \tag{4.9}$$

Where r_{pp} is the position of the particle, r_{bb}^{cp} is the minimum corner-point of the bound-box, $\hat{e}_i$ is the unit vector.

4.2.2 Standard TASC routine: validation study

The hypersonic cylinder test case introduced by Lofthouse *et al.* [111] was initially used for comparative studies between DSMC and Navier-Stokes CFD calculations. This has now become a popular benchmark test for DSMC implementations; it has been used to test new DSMC techniques [5] and new DSMC codes [94]. Therefore, this test case is used to validate the TASC routine and the sub-cells are re-constructed every one-thousand time-steps - this is a suitable amount since steady-state does not take very long to reach. The free-stream conditions and

dimensions for this test case are listed in table 4.4 and figure 4.5, respectively. The simulation gas is Argon, the body-length global Knudsen number based on the cylinder diameter is around 0.01 and the results are compared with Bird [2]. The *dsmcFoam* simulations employ a fixed time-step of 0.01 μs, have around 3.7 million DSMC particles in the system and the results have been sampled for longer than one million time-steps. The computational domain is two-dimensional with 7248 cells and each cell has a dimension of around two mean free paths in all directions. The surface properties are sampled at the same resolution as the computational mesh cells and a 2° interval is used between surface cell boundaries as used by Bird [112]. Finally, an isothermal wall temperature of 500 K is used. The variable hard sphere (VHS) method [4] is employed to process the collisions and since the gas is monatomic the energy between the particles is exchanged in the translational mode only and the gas is considered as non-reacting. The VHS molecular properties at a reference temperature of 1000 K used for the test case are shown in table 4.5 and were set by Lofthouse [39].

Mach number	10
n_∞	4.247×10^{20} m^{-3}
T_∞	200 K

Table 4.4: Free-stream conditions used in the simulations of hypersonic rarefied gas flows over a two-dimensional cylinder.

ω	0.734
d	3.595×10^{-10} m
m	66.3×10^{-27} kg

Table 4.5: Variable hard sphere model parameters for Argon, at a reference temperature of 1000 K, used in the simulations of hypersonic rarefied gas flows over a two-dimensional cylinder.

The heat transfer over the surface of the cylinder for the standard TASC

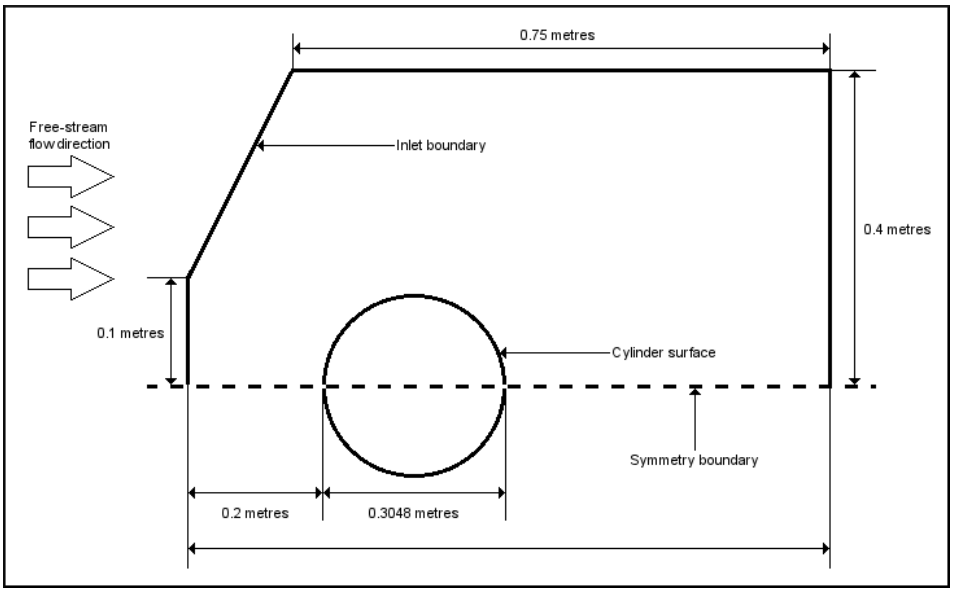

Figure 4.5: Geometry and boundary dimensions used in the simulations of hypersonic rarefied gas flows over a two-dimensional cylinder (drawing not to scale).

routine, conventional 8 sub-cell technique[1] and Bird's data [2] are shown in figure 4.6. For the standard TASC routine eight PPSC has been defined. The heat transfer comparisons between the conventional 8 sub-cell method and Bird's data disagree by a great deal, as expected since the mean collision separation with the 8 sub-cell technique is very large. In other words, the particle collision pairs are selected from larger sub-cell volumes. By increasing the number of sub-cells in a cell, the volume of each sub-cell decreases therefore collision pairs are selected within close vicinity only and as a result the accuracy of the solution is improved as shown in the figure by the standard TASC routine. Similar trends in accuracy are noticed for the shear stress over the surface of the cylinder as shown in figure 4.7. However, the surface pressure is not affected by the different techniques as shown in figure 4.8.

Furthermore, a similar analogy was noticed in section 3.2.2, where the experimental data of the bi-conic cylindrical object was compared with *dsmcFoam*.

[1]The conventional 8 sub-cell technique is transformed into four sub-cells for two-dimensional *dsmcFoam* systems.

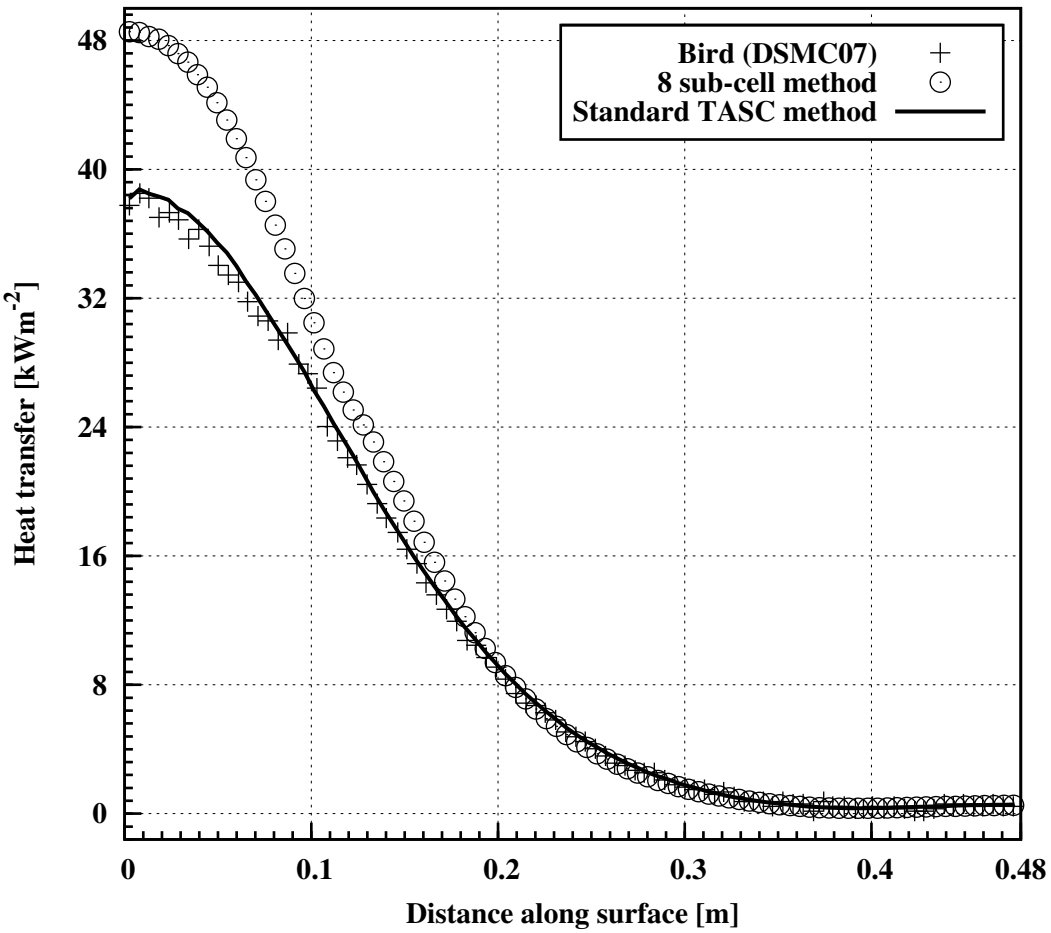

Figure 4.6: Surface heat transfer comparisons of the conventional 8 sub-cell method, standard TASC method and Bird's data [2] over the hypersonic cylinder.

The 8 sub-cell method was used for the simulation and the surface pressure was predicted quite close to the experimental data however, the surface heat transfer was predicted a lot higher than the experiment but followed a similar trend. By using the TASC routine the surface heat transfer over the bi-conic cylindrical object may be reduced and it will be tested in the future.

4.3 Improved TASC routine

In the previous section, the standard TASC routine managed to replicate the results of Bird by using larger cells than the recommended size with a criteria of

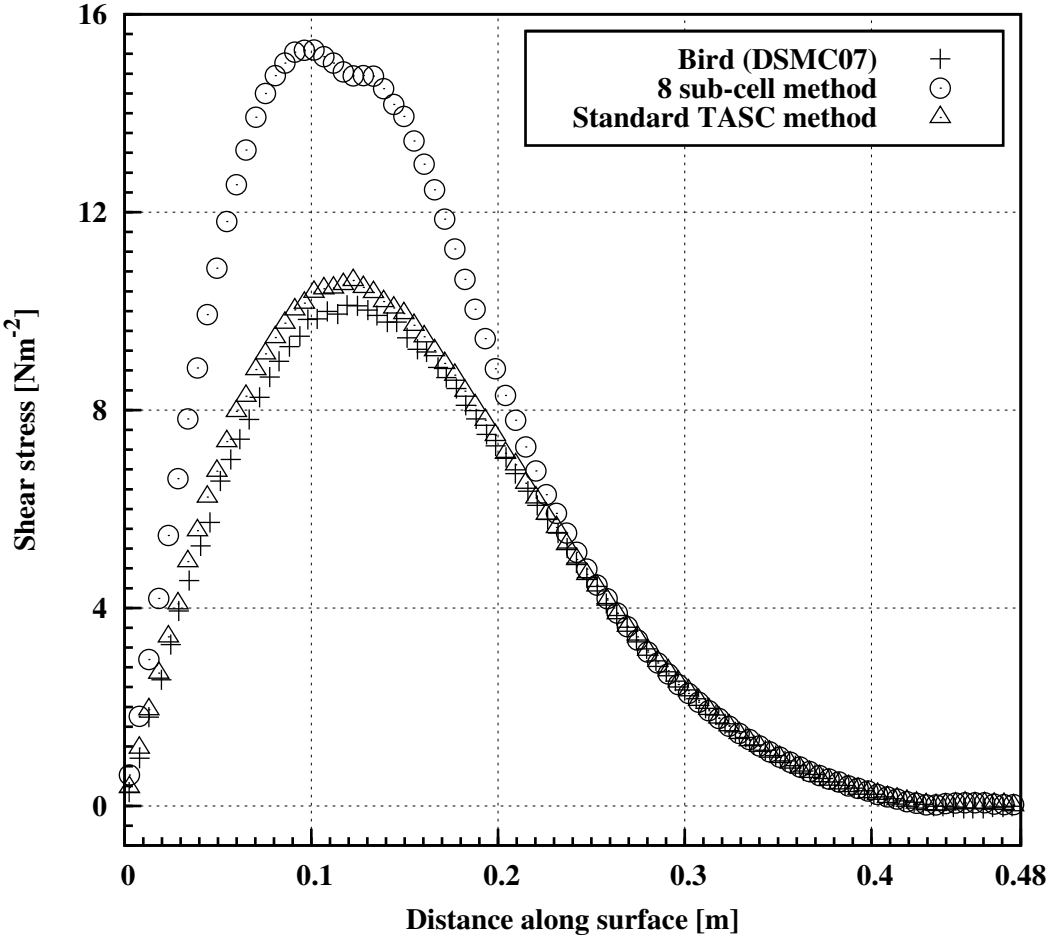

Figure 4.7: Surface shear stress comparisons of the conventional 8 sub-cell method, standard TASC method and Bird's data [2] over the hypersonic cylinder.

eight PPSC. Furthermore, the standard TASC routine was more efficient than the conventional 8 sub-cell method as for each time-step an average of 5.5% saving was noticed. However, this section outlines the problem of the TASC method and demonstrates it on the hypersonic cylinder. This problem arises when the user initially defines the number of PPSC to a value below eight. As this value reduces from eight, the error in the simulation increases. To resolve this, an improvement is also introduced to allow the number of PPSC to be defined to a value below eight, without sacrificing a great deal of accuracy. Also the sensitivity of particles, mesh and time-step on a system is investigated for the improved TASC routine.

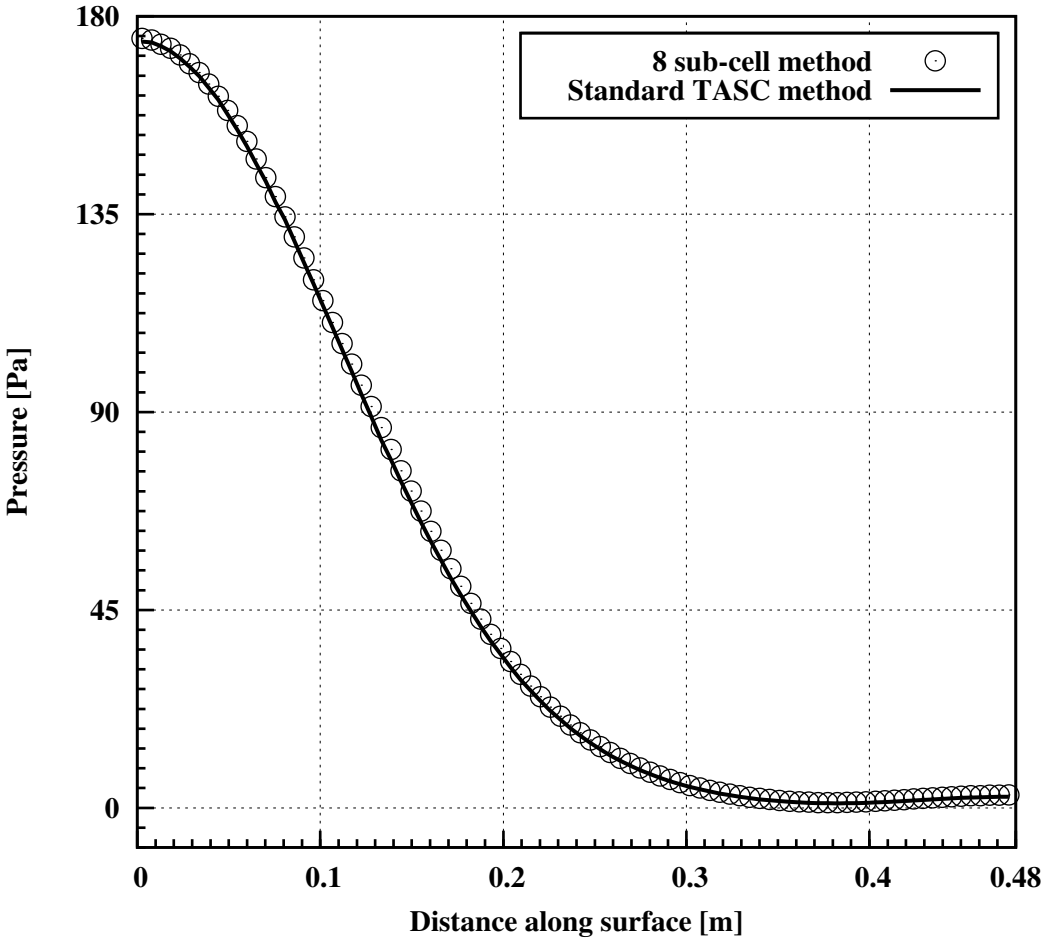

Figure 4.8: Surface pressure comparisons of the conventional 8 sub-cell method and standard TASC method over the hypersonic cylinder.

4.3.1 Improved TASC routine: background

The standard TASC routine only produces high accuracy results when the PPSC is defined as eight for the hypersonic cylinder test case considered in section 4.2.2. Reducing this value affects the surface heat transfer and shear stress greatly, as shown in figures 4.9 and 4.10, respectively. However, it has no affect on the surface pressure. As noticed in these figures, the differences start to become more apparent when the set number of PPSC decrease. As the number of PPSC reduces the probability of repeat collisions increase, and if there is only one PPSC then its collision partner is chosen from the entire cell, thus the degree of error

elevates as the size of the cell increases. The improved TASC routine produces a solution to this problem of one PPSC, it enforces the particle pairs to be chosen within close vicinity. The term G, is added as a denominator to the right hand side of equation 4.5 and this has a direct impact on the sub-cell volume, because as the value of G increases the volume of each sub-cell increases and as a result the number of sub-cells is reduced. The sub-cell volume is increased until the particular particle is surrounded by one or more other particles. The process of increasing the sub-cell volume is shown in figure 4.11 and an example of the process stages in this figure are demonstrated in figure 4.12. Furthermore, if the particle does not find another particle in the last transformation of the sub-cell volume at stage (f), then it resorts to looking for a particle in the entire cell. Also, this is rare and only occurs when there are a lot of sub-cells and is more likely to arise when the number of PPSC, defined at the start, is very low.

4.3.2 Improved TASC routine: validation study

The improved TASC routine is validated using the same, hypersonic cylinder test case as in section 4.2.2. The same mesh is used for all tests considered in this section. Using the improved TASC method the minimum number of PPSC is sought, and reduced from eight, that produces similar results as Bird. This minimum is determined as six PPSC as shown for the surface heat transfer over the cylinder in figure 4.13. Any value lower than six PPSC still produces a peak surface heat transfer closer to Bird than the standard TASC routine, as illustrated in table 4.6. A similar trend is found in the drag force calculations, as in table 4.7, using both routines at different PPSC definitions. That is, as the number of PPSC increase the drag force gets closer to Bird's prediction of 39.95 N. For both routines the drag force is predicted closest to Bird at six PPSC,

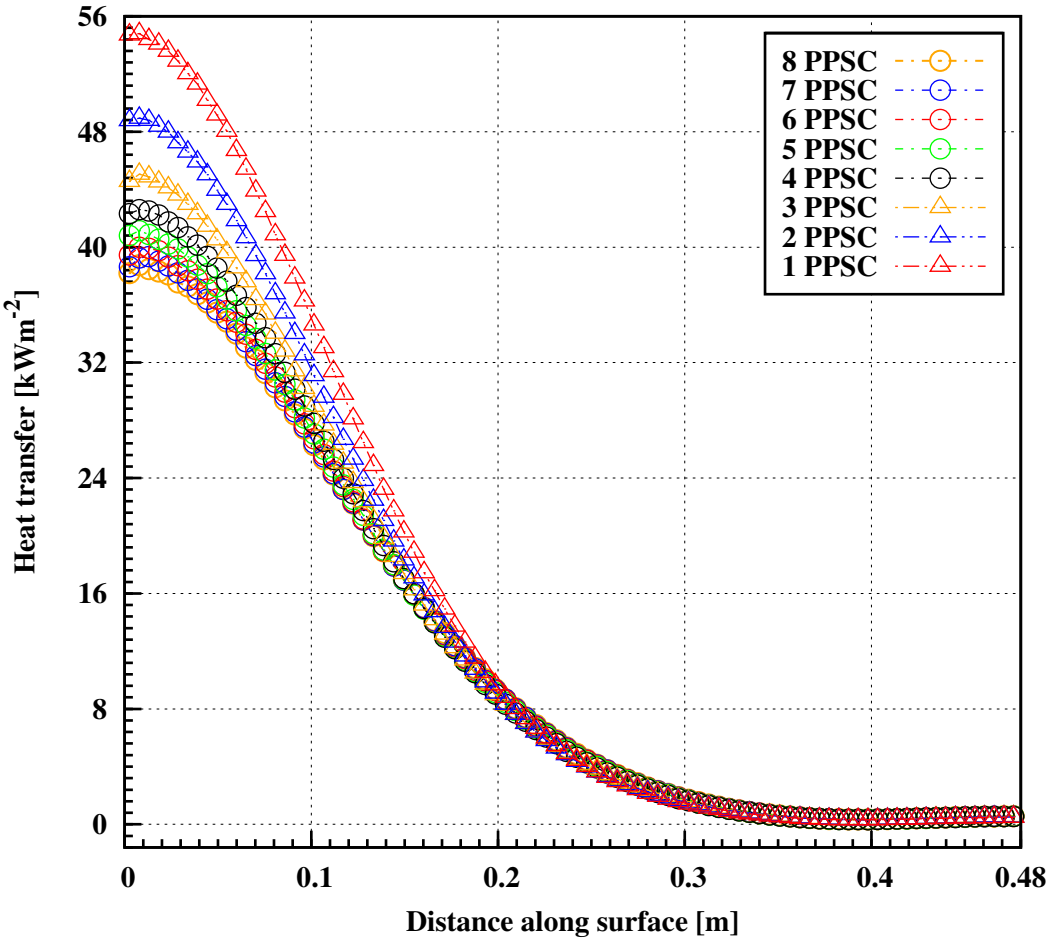

Figure 4.9: The effect of the number of PPSC using the standard TASC routine on the heat transfer over the hypersonic cylinder.

and the difference for the seven and eight PPSC defined systems is no more than 0.15% from Bird. Furthermore, the shear stress is predicted very close to the standard TASC routine at eight PPSC but it did not reduce to a value closer to Bird.

Moreover, the results from some of the lower defined number of PPSC of both routines are within the minimum and maximum values in table 4.8, and these values are determined by various solvers in the literature [2]. The surface heat transfer results of the improved TASC routine using eight PPSC are in better agreement with Bird than PDSC (with TASC) [5]. These results produced by

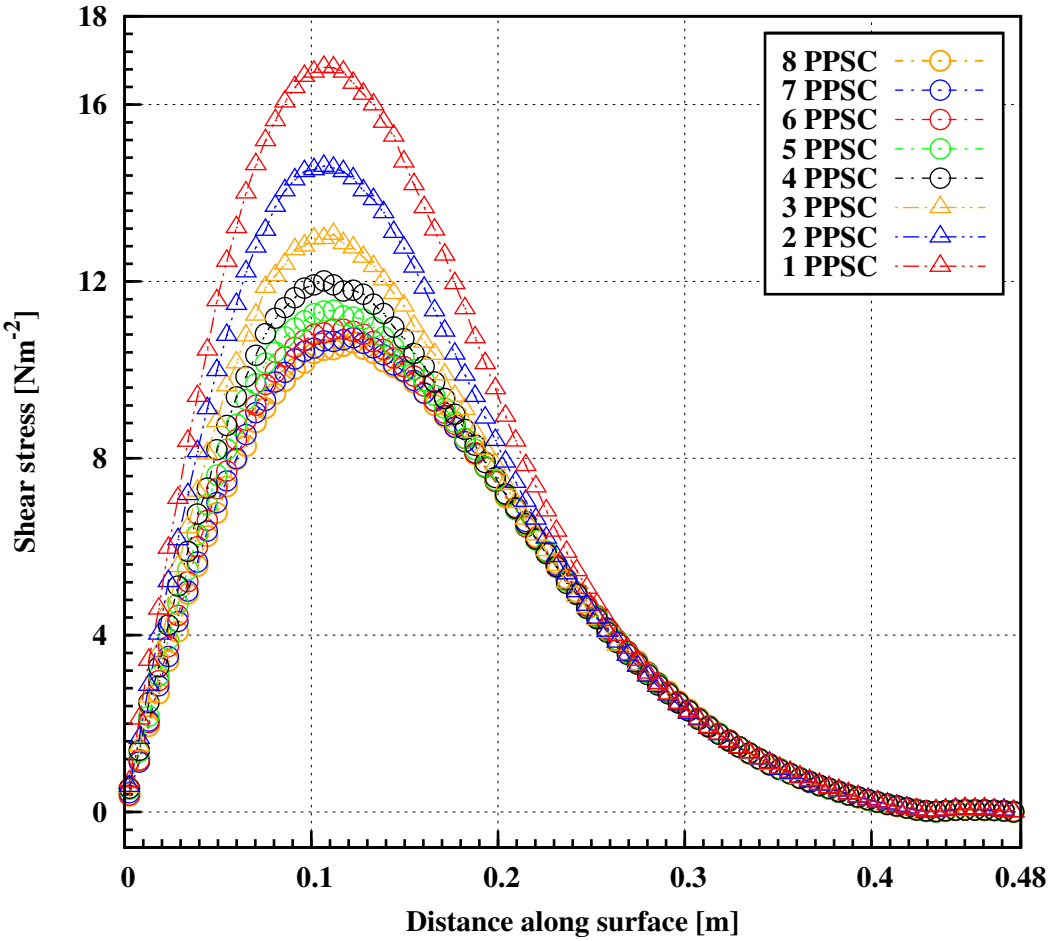

Figure 4.10: The effect of the number of PPSC using the standard TASC routine on the shear stress over the hypersonic cylinder.

PPSC	Standard TASC routine	Improved TASC routine
8	38747.82	38337.97
7	39350.66	38668.19
6	39989.24	38942.83
5	41144.12	39620.71
4	42598.11	40202.06
3	45051.21	42047.70
2	48930.68	44843.14
1	54806.21	51053.99

Table 4.6: The peak surface heat transfer [Wm^{-2}] predicted by *dsmcFoam* using the standard and improved TASC routines at different defined PPSC. Bird's [2] peak surface heat transfer is 38300 Wm^{-2}.

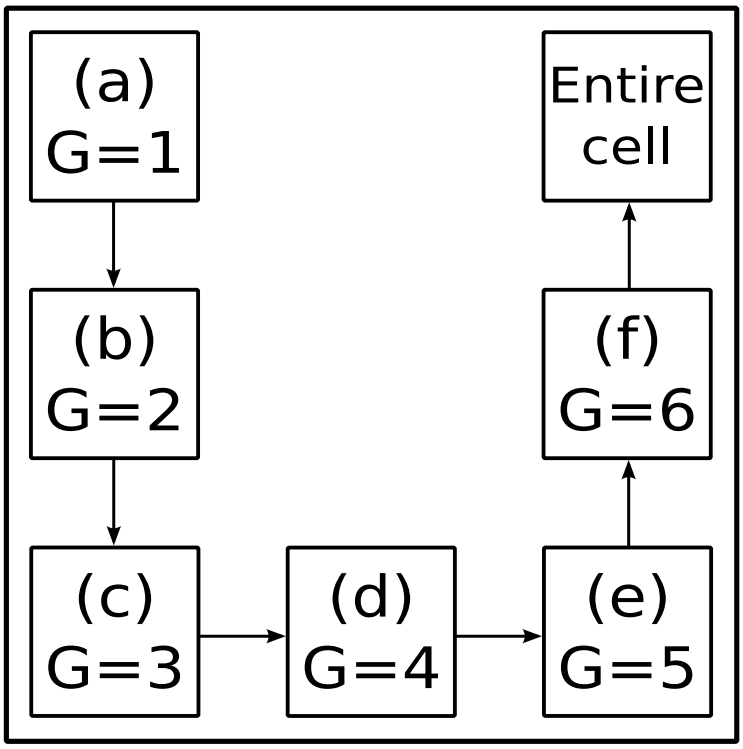

Figure 4.11: The procedure of the improved TASC routine, in alphabetical order, in finding collision pairs in close vicinity when there is only one particle in the sub-cell of the sub-cells initially generated at (a). G is defined in section 4.3.1.

PPSC	Standard TASC routine	Improved TASC routine
8	39.89	39.90
7	39.92	39.92
6	39.96	39.97
5	40.03	40.03
4	40.17	40.12
3	40.40	40.25
2	40.83	40.51
1	41.50	41.14

Table 4.7: The drag force [N] predicted by *dsmcFoam* using the standard and improved TASC routines at different defined PPSC. Bird's [2] drag force is 39.95 N.

PDSC were based on a criteria of 2 PPSC and had a larger number of PPSC been defined then the results may have been closer to Bird. Table 4.8 also shows results of *dsmcFoam* with standard and improved TASC and without TASC.

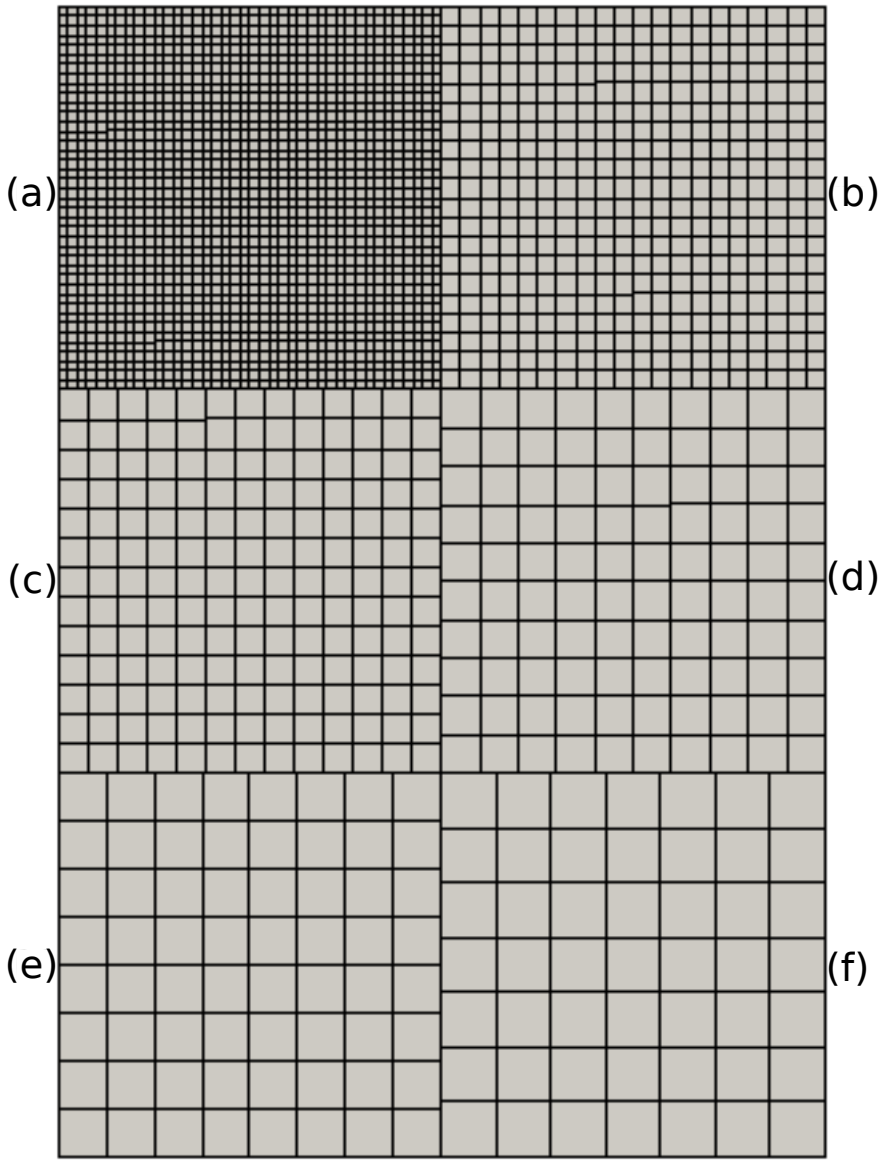

Figure 4.12: Example of the improved TASC routine in finding collision pairs in close vicinity when there is only one particle in the sub-cell of the sub-cells initially generated at (a). This is an example for a two-dimensional cell, but it is similar to a three-dimensional approach. In this figure, each stage is assigned a letter and they are processed in alphabetical order.

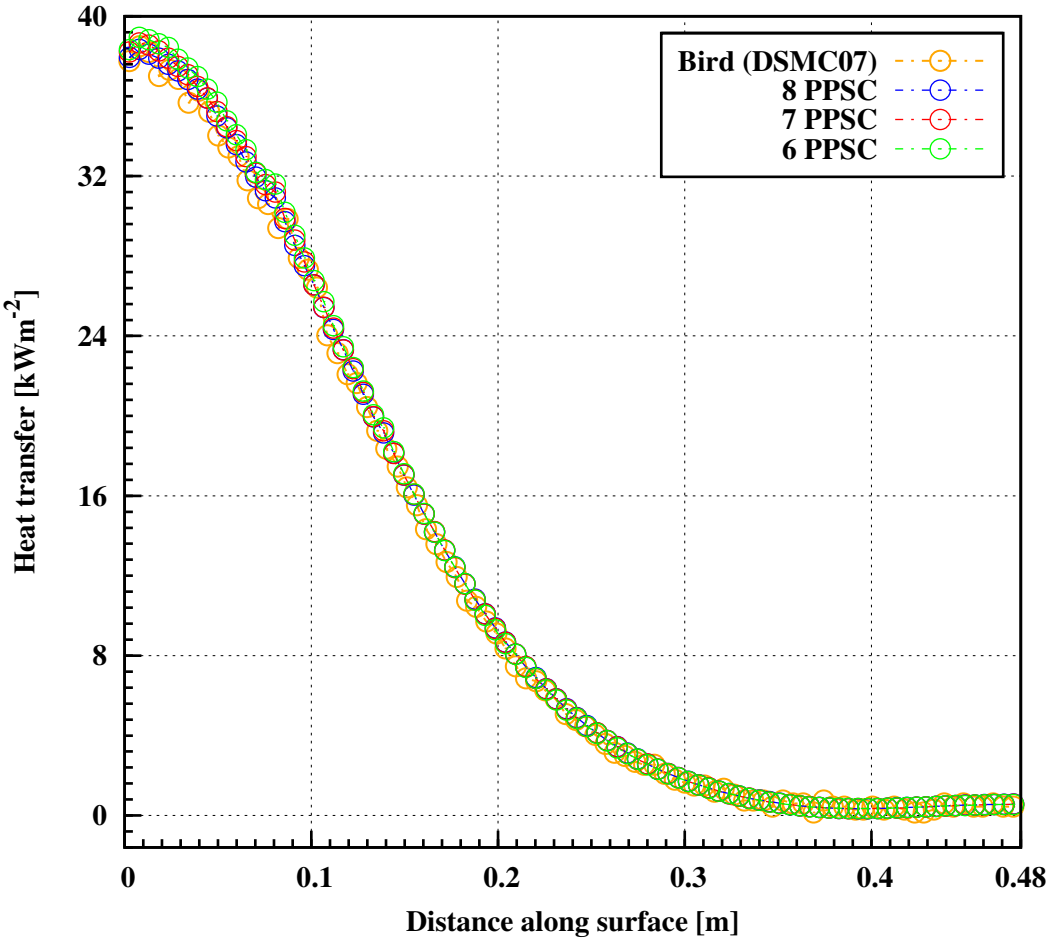

Figure 4.13: Surface heat transfer comparisons over the hypersonic cylinder between the improved TASC method and Bird's data [2].

Solver	Peak heat flux [Wm^{-2}]	Total drag [N]
MONACO	39319	40.00
SMILE	39000	39.76
DAC	38500	39.71
DS2V	38400	39.76
PDSC (without TASC)	44813	41.90
PDSC (with TASC)	40888	39.16
dsmcFoam (without TASC)	48547.52	40.80
dsmcFoam (standard TASC)	38747.82	39.89
dsmcFoam (improved TASC)	38337.97	39.90

Table 4.8: The peak heat flux and total drag predicted by *dsmcFoam* and various other DSMC solvers over the hypersonic cylinder [5].

4.3.3 Improved TASC routine: Particle, time-step and mesh sensitivity investigation

To further validate the improved TASC routine a thorough particle and time-step study is undertaken in this section using the hypersonic cylinder test case, investigated previously. Following this, a particle and mesh sensitivity study is undertaken using a steady driven cavity flow of Su *et al.* [5] that compares benchmark results against the improved TASC, standard and no sub-cell routines.

Hypersonic cylinder: sensitivity study

Firstly, a particle sensitivity study on the hypersonic cylinder is considered and table 4.9 illustrates the number of particles used in each system. For each system of particles two scenarios are simulated, one with a defined PPSC of seven and the other eight, and these two definitions are used since they produce results that are in excellent agreement with Bird in section 4.3.2. The same mesh over the cylinder, considered in all test cases previously in this chapter, is adopted for the simulations and between each test there is a difference of at least a million particles. For all tests the heat transfer over the surface of the cylinder is compared in figure 4.14 against Bird's predictions. Also, this figure only shows the surface heat transfers of the first 0.12 m along the surface. And beyond 0.12 m all results are in very good agreement and beyond 0.14 m all results are in excellent agreement. The comparisons in figure 4.14 and the comparisons of drag forces in table 4.9 are in good agreement with Bird and the agreement becomes closer as the number of particles increase in the system. Also, as the number of particles increase from 2.83 million to 5.82 million the drag force becomes lower than Bird's prediction but the difference is no more than 0.2% for both PPSC definitions. In addition, DAC and SMILE predicted [2] lower drag forces than

Bird and the standard and improved TASC routines using seven or eight PPSC with 3.7 million particles in the system, as shown in section 4.3.2, also predicted lower drag forces than Bird. Increasing the number of particles in the simulation requires more computational resources, but one possible method to reduce the computational run-time is to employ a larger time-step, but not too large such that it reduces the accuracy of the simulation.

Test case	Particles	PPSC	Total drag [N]
A.1	5.82 million	7	39.89
A.2	5.82 million	8	39.87
B.1	2.83 million	7	39.95
B.2	2.83 million	8	39.93
C.1	1.42 million	7	40.03
C.2	1.42 million	8	40.01
D.1	0.37 million	7	40.31
D.2	0.37 million	8	40.30

Table 4.9: The number of particles used for the particle sensitivity study on the hypersonic cylinder. The total drag force predicted is also illustrated for each test.

Furthermore, figure 4.15 shows the heat transfer over the cylinder using a time-step of 0.01 μs, used in previous cylinder test cases in this chapter, and a time-step of 0.2 μs. In addition, the same number of particles and number of PPSC are employed in these two cases as in test case B.2 and the latter time-step is the same as one of the benchmark test cases of Bird [2]. The figure shows the results are not significantly affected by the larger time-step and identical drag forces are predicted by both scenarios. Although, the larger time-step has predicted a slightly larger heat transfer at the stagnation region the computational run-time has been reduced by around 90%. Increasing the time-step further will reduce the accuracy of the properties as figure 4.16 shows the maximum time-steps that

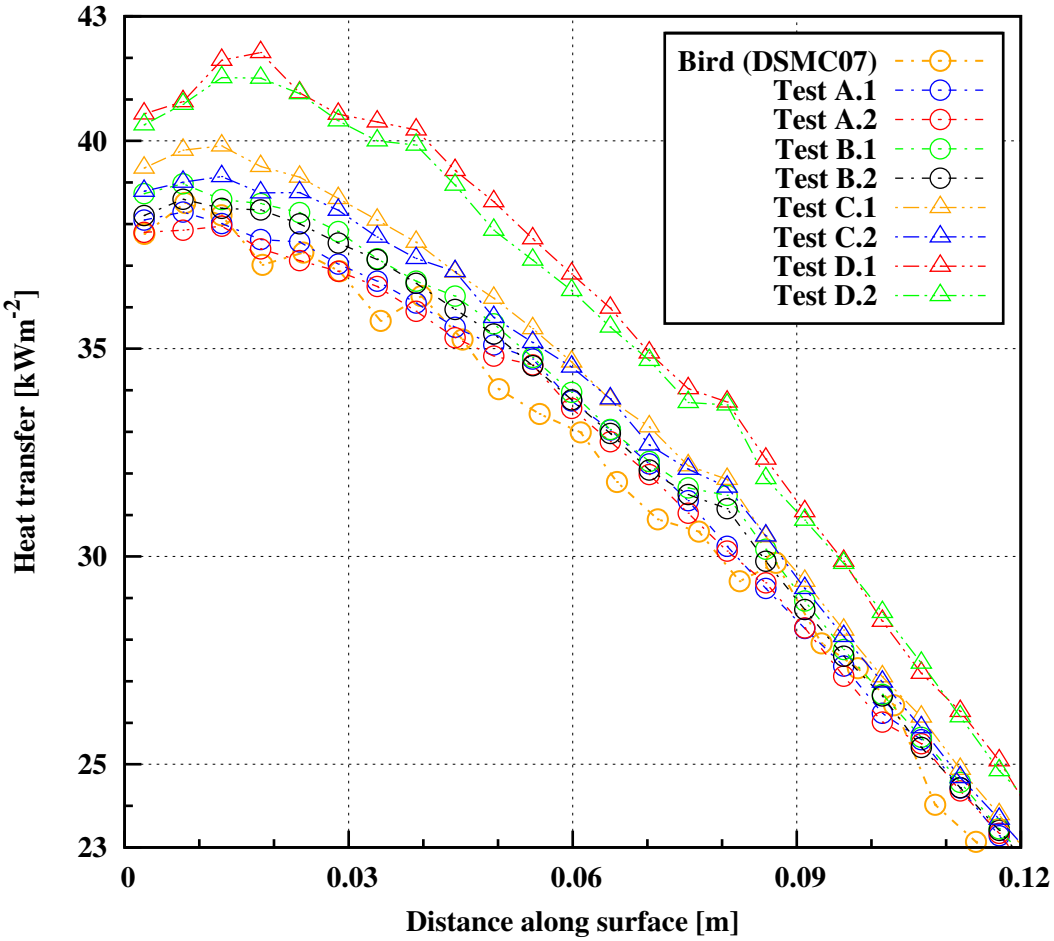

Figure 4.14: The sensitivity of the particles on the surface heat transfer over the hypersonic cylinder.

can be used throughout the domain. These time-steps are represented as,

$$Time - step = \left\lfloor \frac{0.3\lambda_{VHS}^{loc}}{U_{mp}} \right\rfloor, \tag{4.10}$$

where λ_{VHS}^{loc} and U_{mp} represent the variable hard sphere local mean free path and most probable velocity, respectively. The time-steps are normally a fraction of the calculation in equation 4.10, so that particles remain in a cell for a number of time-steps to aid the averaging process. The time-steps in the figure do not include an extra fraction of a third for good DSMC practice, but with the fraction some of the time-steps become lower than 0.2 μs but are still larger than 0.01 μs.

Therefore good DSMC practice is not fulfilled throughout all of the domain with the larger time-step, but the results are still in good agreement.

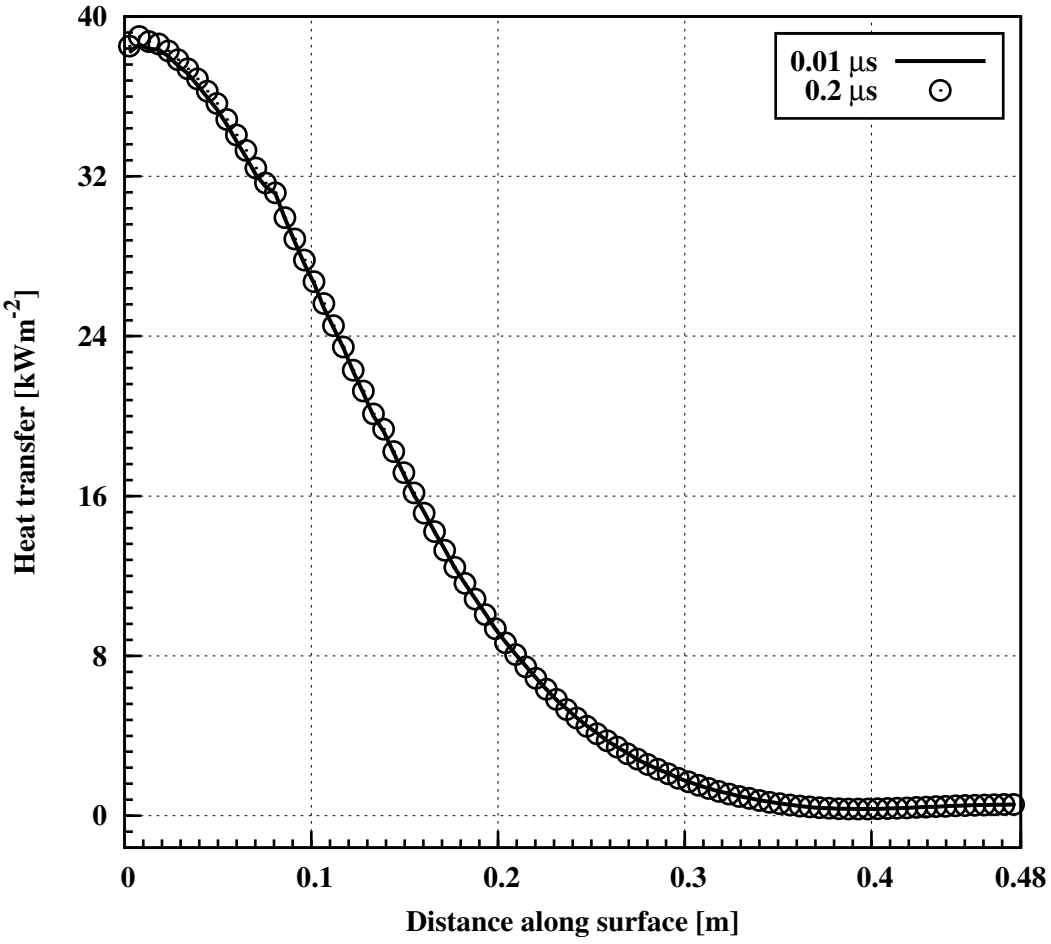

Figure 4.15: The sensitivity of the time-step size on the surface heat transfer over the hypersonic cylinder.

Steady driven cavity flow: sensitivity study

The final validation study for the improved TASC routine involves a steady driven cavity flow that is two-dimensional. The computational domain consists of walls that are diffusely reflecting the particles away at a temperature of 300 K. The upper wall has a velocity of 354.2 ms^{-1} (Mach 1.1) and all other walls are stationary as shown in figure 4.17. The cavity is initialised with stationary Argon gas at

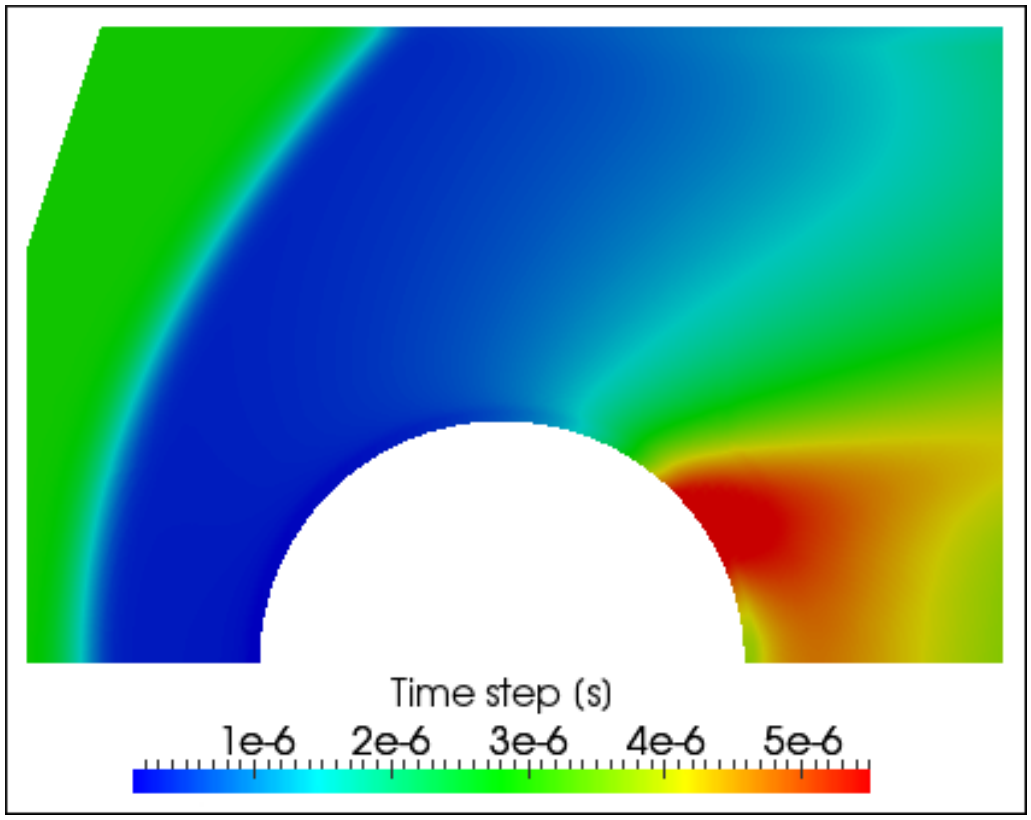

Figure 4.16: The maximum time-step size, based on equation 4.10, that can be used throughout the computational domain of the hypersonic cylinder.

300 K and the body length global Knudsen number is 0.01 where the length scale is based on the cavity dimensions. Five simulations, illustrated in table 4.10, are initially undertaken and they include two benchmark tests and three simulations that have approximately one mean free path long cell dimensions.

Firstly, both benchmark test cases A and B have cell sizes that are a quarter of the mean free path therefore their results should be the same. The contours of overall temperature and a profile of the overall temperature through the vertical centreline of the cavity domain are shown in figures 4.18 and 4.19, respectively. Both benchmark test cases are compared in these two figures and the results are in very good agreement, thus the benchmark does not require sub-cells. The sub-cell parameter is now compared for the remaining three tests, as shown in table 4.10, against the benchmark run in figure 4.20. Test case B and E, are in

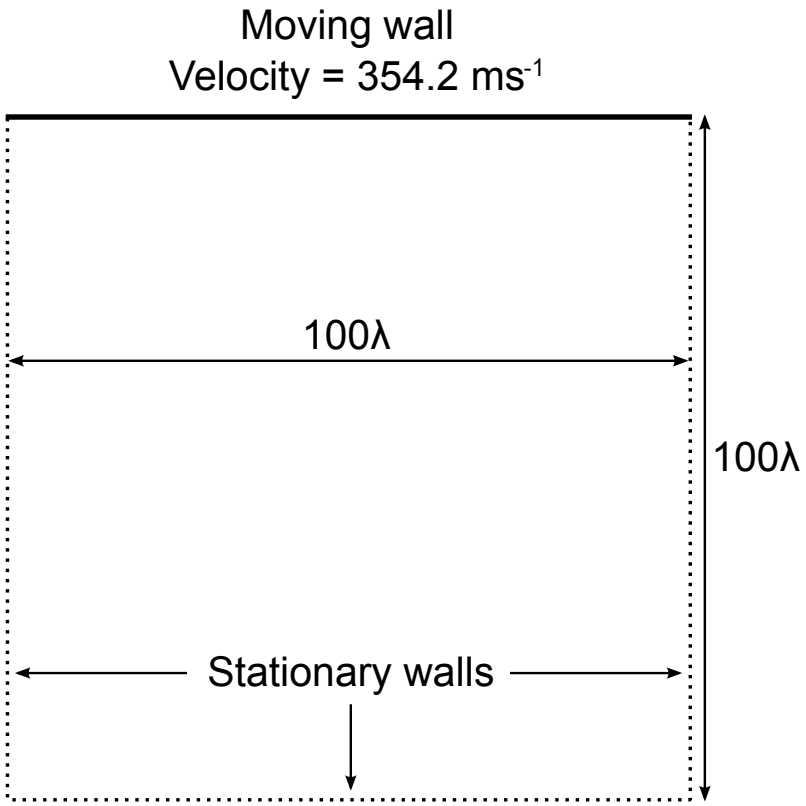

Figure 4.17: Steady driven cavity flow configuration.

Test case	Sub-cells	Cells	Total particles	Execution time per time-step (s)
A	Standard	400 x 400	4 million	10.30*
B	No	400 x 400	4 million	10.19*
C	Standard	100 x 100	0.25 million	0.378*
D	No	100 x 100	0.25 million	0.271
E	TASC	100 x 100	0.25 million	0.275

Table 4.10: Test cases for the steady driven cavity flow. Tests A and B are considered as benchmark cases and test E employs the improved TASC routine using 8 PPSC. The standard sub-cells employ 4 sub-cells for two-dimensional cells. The execution times are based on one processor and the * denotes parallel simulations.

good agreement but some differences are noticed in the peak values but this may be due to the macroscopic data not been picked up very well due to the larger cells in test E. Test C is in very good agreement with test E, as by chance test C has roughly the same number of PPSC as test C. This is because test C employs

standard sub-cells in all cells that have more than one particle and the average number of particles per cell in the entire domain is 25. When no sub-cells are employed for the test case with large cell sizes (test D), the results are far from the benchmark as the mean collision separation is large.

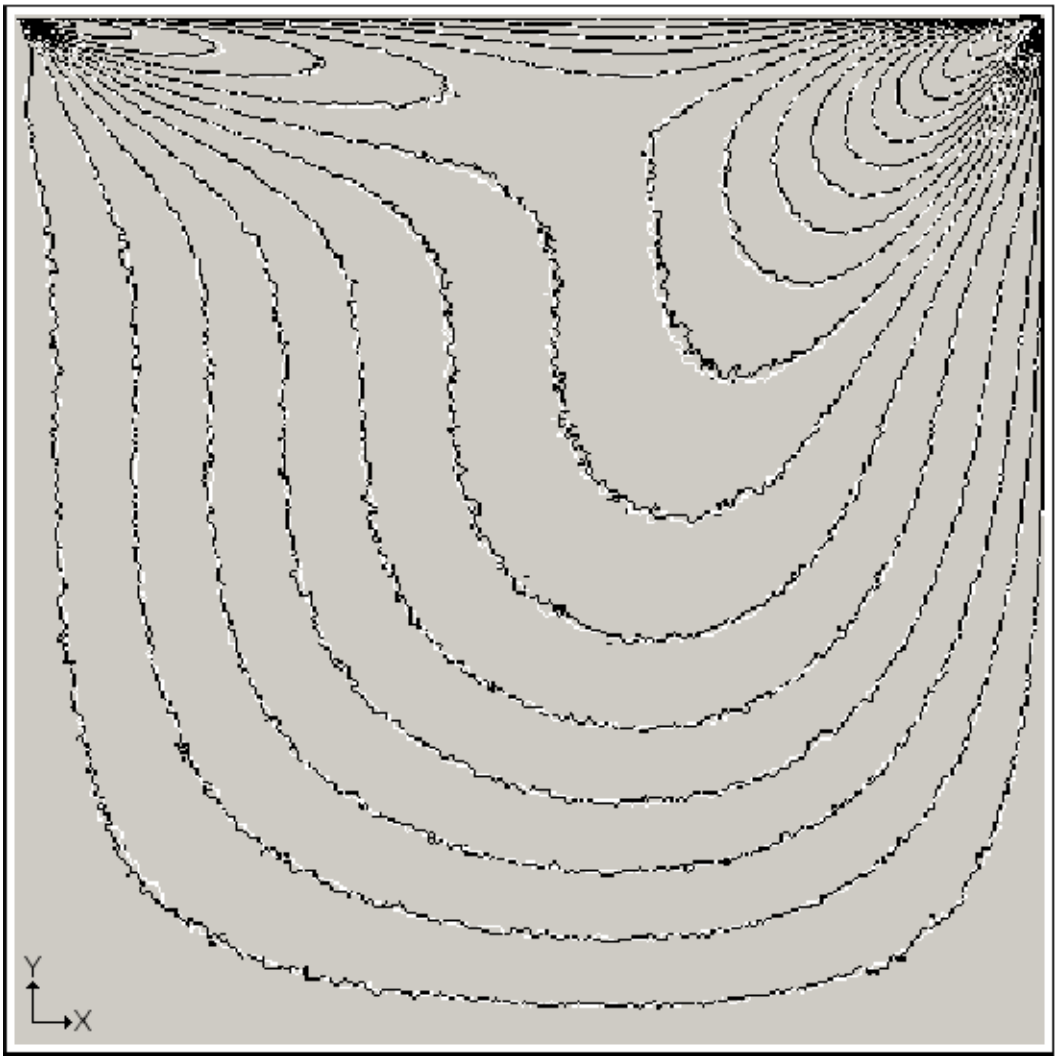

Figure 4.18: Contours of overall temperature of the steady driven cavity flow. The black and white lines represent the benchmark test cases with standard sub-cells and no sub-cells, respectively.

The influence of the number of PPSC on the cavity is shown in figure 4.21 using the improved TASC routine. The results show that all PPSC calculations are in very good agreement, apart from 1, 9 and 10 PPSC and their corresponding

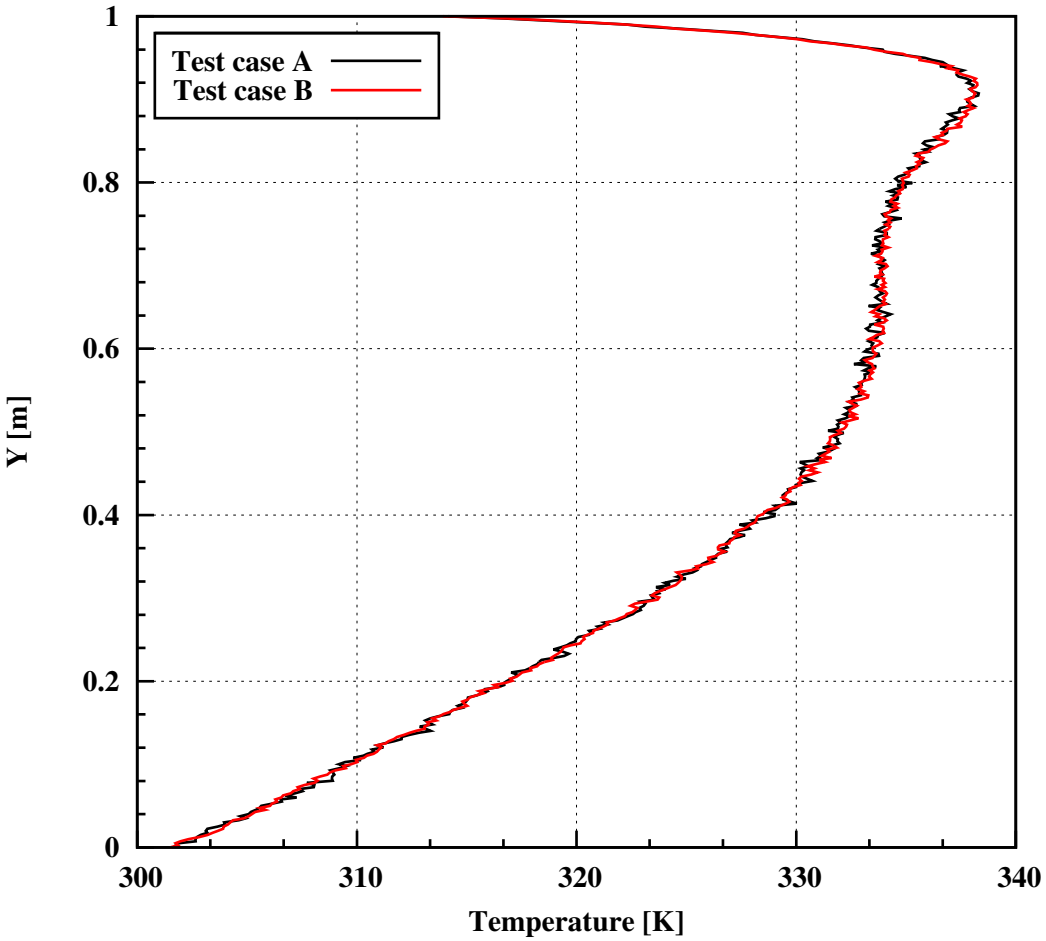

Figure 4.19: Comparisons of temperature profiles through the vertical centreline of the computational domain for the steady driven cavity flow. Test cases A and B represent the benchmark run with standard sub-cells and no sub-cells, respectively.

profiles are further away from the benchmark. However, 1, 9 and 10 PPSC have a difference of no more than 0.5% in comparison to the remaining tests in figure 4.21. The differences by 9 and 10 PPSC might be caused by the large mean collision separation as the cell size is larger in comparison to the lower PPSC and in the case of 1 PPSC, there may have been more repeat collisions.

Finally, the cavity sensitivity study has produced a different phenomenon to the hypersonic cylinder sensitivity study, considered in the previous section, and related to the influence the number of PPSC has on the macroscopic properties. The cavity properties are not affected as much, by the different number of PPSC,

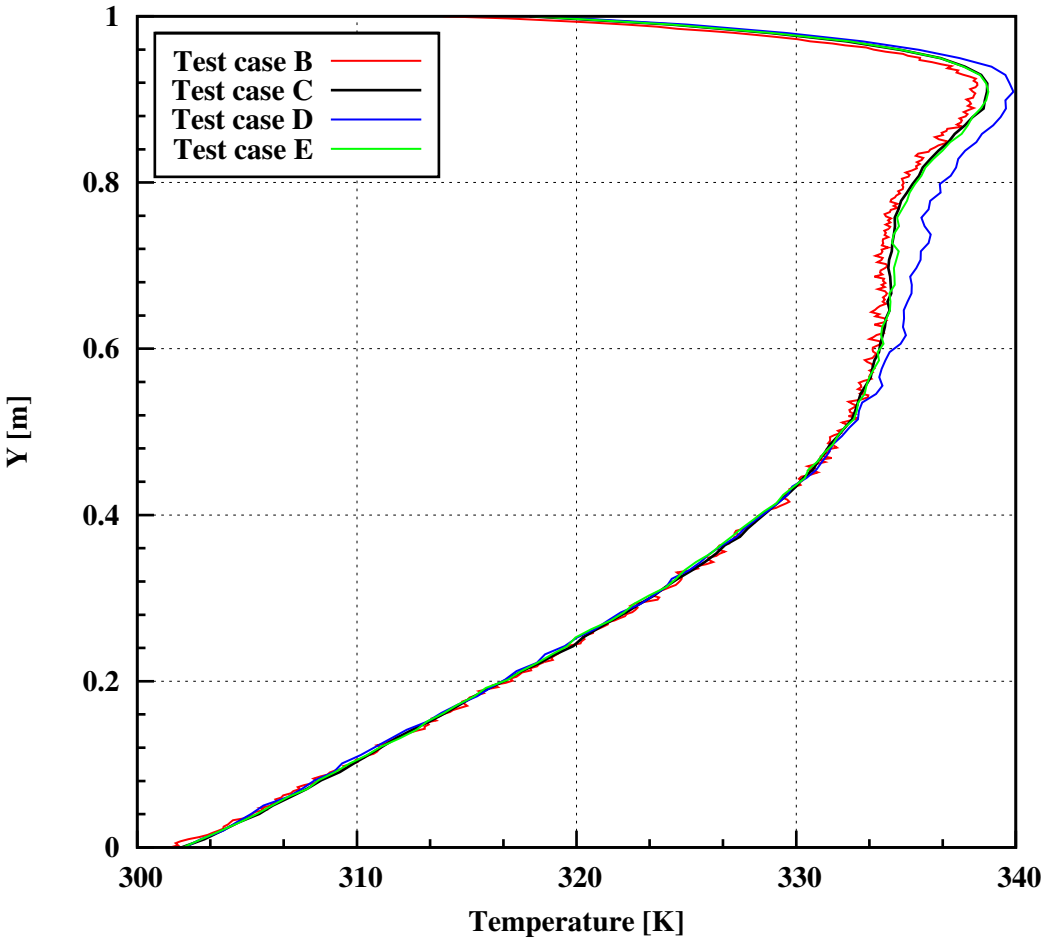

Figure 4.20: Comparisons of temperature profiles through the vertical centreline of the computational domain for the steady driven cavity flow. Test case B represents the benchmark run with no sub-cells. Test cases C, D and E represent the runs with larger cell sizes using standard and no sub-cells and the improved TASC routine (8 PPSC), respectively.

as the hypersonic cylinder properties. This is because the cavity case has cell sizes that are roughly one mean free path long, therefore with the use of sub-cells good DSMC practice is met throughout the domain.

4.4 Summary

This chapter presented the importance of a cell volume in determining collision pairs. It also presented a new TASC routine, implemented in *dsmcFoam*, and an extension to the 8 sub-cell method for the purpose of selecting collision partners

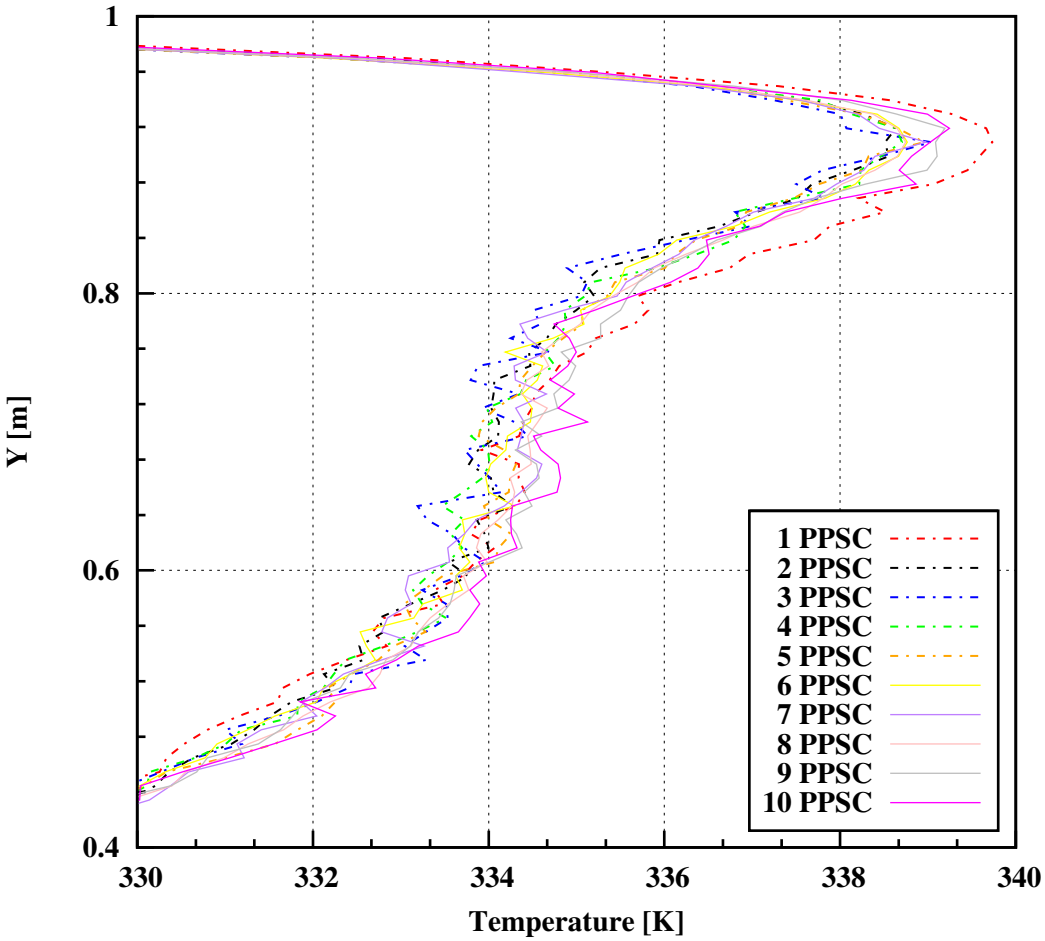

Figure 4.21: The effect of varying the number of PPSC, using the improved TASC routine, on the temperature profile through the vertical centreline of the computational domain for the steady driven cavity flow.

in close proximity to each other. The standard TASC method proved to be a reliable tool in predicting accurate properties of systems that have a large cell size, as shown in figures 4.6 and 4.7 for the cylinder test case. The size of the cells in this case were approximately two mean free paths long, this is relatively large in comparison to the recommended size of one third of the mean free path. In the same graph it is evident that the results using the conventional 8 sub-cell method do not agree well with Bird's results as good DSMC practice was not followed. The TASC method requires a smaller number of computational mesh cells in the system in comparison to the conventional method for a similar accuracy, therefore

the TASC method uses less memory and as a result has a faster solution time. Also, less computer random-access memory is required for post-processing.

The TASC method was then improved for sub-cells that contain only one particle. In this scenario, the standard TASC method looks for a collision partner in the entire cell whereas the improved TASC algorithm looks for a collision partner in close proximity - it does this by increasing the volume of the sub-cells until there is one or more possible collison partners.

Chapter 5

Dynamic Wall Temperature Model

This chapter outlines the issues concerning surface temperatures in DSMC simulations. The surface temperature may have a direct influence on the farfield and surface properties, therefore it is important to define it in a robust manner. In practice, the wall temperature is assumed to be isothermal and fixed to a value ranging between 500 and 2000 K over the entire surface. However, this is not valid in most systems that involve hypersonic gas flow streams as the wall temperature is closely related to the heat flux. This will be discussed in more detail later in this chapter, also a dynamic wall temperature model (DWTM) for *dsmcFoam* is introduced as an alternative boundary condition. Verification and validation studies of this DWTM are also investigated in this chapter.

5.1 Introduction

The treatment of particles impinging on the surface is of the utmost importance in DSMC simulations, especially when dealing with the surfaces of hypersonic re-

entry vehicles. Particles hitting and leaving the surface introduce a momentum and energy transfer which in particular affects the aerodynamic properties (i.e. forces and moments) and heating rates, respectively and are essential to the design process of any planetary vehicle. These properties, as well as far-field properties, may be sensitive to the surface condition therefore the surface has to be treated accurately in DSMC but this can be a challenge. In addition, the effect of wall temperature on the properties are discussed in sections 5.2.1 and 5.2.2. The most common DSMC boundary model reflects the particles away from the surface in a completely diffuse manner. These particles leave the surface with a new velocity sampled from a biased Maxwellian distribution based on an isothermal wall temperature. This wall temperature is normally between 500 and 2000 K but there is not a particular definition set in stone.

5.2 Limitation of an isothermal wall temperature model

Diffuse, or a mix of both diffuse and specular wall boundary models require a temperature definition, commonly set to an isothermal condition between 500 and 2000 K for hypersonic DSMC simulations:

- Vashchenkov and Ivanov [113] studied the re-entry aerothermodynamics of the European experimental re-entry testbed space capsule using a constant wall temperature of 1400 K,
- Sampaio and Santos [114] investigated the re-entry aerothermodynamics of a small ballistic re-entry Brazilian vehicle using a constant wall temperature of 800 K,

- Ahmad *et al.* [8, 9] examined the re-entry aerothermodynamics of a re-usable single-stage to orbit vehicle (Skylon spaceplane) using a wall temperature of 1000 K,

- Moss *et al.* [1] performed simulations for aerodynamic forces and moments acting on the Apollo capsule throughout the hypersonic low-density transitional flow regime. A number of different wall temperatures were used in the DSMC simulations and they ranged from 234 to 1598 K for altitudes from 200 to 85 km, respectively.

- Bányai *et al.* [90] investigated the behaviour of the Intermediate eXperimental Vehicle in the upper layer of the atmosphere using a wall temperature of 900 K.

The isothermal wall temperature may be determined by assuming the incident free-stream kinetic energy is fully radiated at the surface using the Stefan-Boltzmann law [115]:

$$\frac{1}{2}\rho_\infty U_\infty^3 = \epsilon\sigma T_W^4, \tag{5.1}$$

where ρ_∞ and U_∞ represent the free-stream density and velocity, respectively and ϵ, σ and T_W are the emissivity, Stefan-Boltzmann constant and wall temperature, respectively. Another method to define the wall temperature is to set the wall as the arithmetic average between the free-stream and stagnation temperature [7]. For the Apollo capsule, Moss *et al.* defined the surface temperature at each altitude as the smallest isothermal value from either the radiative equilibrium value fixed from the heating, at the stagnation point, that is based on the correlation of Sutton [101] or the free-molecular radiative equilibrium heat flux at the stagnation point.

In most DSMC simulations, the isothermal wall assumption is not valid as the temperature of the surface is closely related to the heat flux. The most common DSMC simulation, presented by Bird [2], for code benchmarking is the hypersonic flow over a cylinder. Since this case was for benchmarking purposes only it is acceptable to set an isothermal wall condition but due to the nature of this problem a high temperature bow shock is created upstream of the cylinder, therefore the heat flux is higher on the forebody than the afterbody as a result the temperature should be greater on the forebody than the afterbody, this may influence the aerodynamic forces, surface pressure and shear stress as they are closely related to the pre- and post-momentum of a particle impinging on the wall. The same applies to the surface heat transfer, but it is related to the energy of the particle instead of the momentum. The energy of the particle leaving the surface is sampled from a distribution function based on the wall temperature.

Furthermore, sampled properties are investigated for hypersonic gas flows over two geometries to demonstrate the inconsistencies associated with using one temperature value over the entire surface. The two set-ups used in the investigation are,

1. hypersonic gas flow over a cylinder and
2. hypersonic gas flow over a step.

Both cases represent a significant challenge to numerical codes as they must capture flow physics including weak or diffuse shocks, boundary layer separation, flow recirculation, rapid expansion and re-compression and shear layers with steep gradients of velocity, temperature and density. Therefore these test cases are believed to be suitable for this investigation as they represent some of the conditions planetary vehicles experience through the atmospheric re-entry stage.

5.2.1 Hypersonic gas flow over a cylinder

The hypersonic cylinder benchmark test case used in sections 4.2.2 and 4.3.2 to validate the standard and improved TASC algorithms is used in this section to investigate the effect of different isothermal wall temperature definitions on the surface of the cylinder. The reader is referred to section 4.2.2 for the dimensions and conditions, including the molecular parameters, of the hypersonic cylinder test case. Four tests are carried out using the wall temperature definitions listed in table 5.1. For each test the improved TASC algorithm, discussed in section 4.3, is applied. The condition set for the desired number of particles per sub-cell, in the improved TASC algorithm, is eight. Using this criteria the TASC method, for both standard and improved algorithms, has produced excellent comparisons with Bird [2] in the previous chapter. To differentiate between all four test

Test	T_W [K]
Test A (benchmark test)	500
Test B	1000
Test C	1500
Test D	2000

Table 5.1: Surface temperatures used in the simulations of hypersonic gas flow over a two-dimensional cylinder.

cases the surface heat transfers of tests B, C and D are analysed as a percentage difference from the benchmark case and is determined by,

$$(Test\ case - Test\ A)\,\% = \left(\frac{Test\ case - Test\ A}{Test\ A}\right) \times 100, \tag{5.2}$$

where *Test case* represents the surface property of test B, C or D and *Test A* represents the surface property of test A. The comparison of surface heat transfers, calculated using the above equation, are plotted as absolute values in figure 5.1. Significant difference are noticed for tests B, C and D in comparison to the bench-

mark, with approximately 8% difference at the stagnation point for test B and rising up to approximately 24% for test D. Also, the largest differences are noticed at the afterbody and as the temperature of the wall increases the surface heat transfer at each surface element decreases. Furthermore, the shock stand-off distance becomes larger as the wall temperature increases as shown in figure 5.2 and this is caused by the particles reflecting of the wall with greater energies that are based on the higher surface temperatures, as a result pushing back the shock.

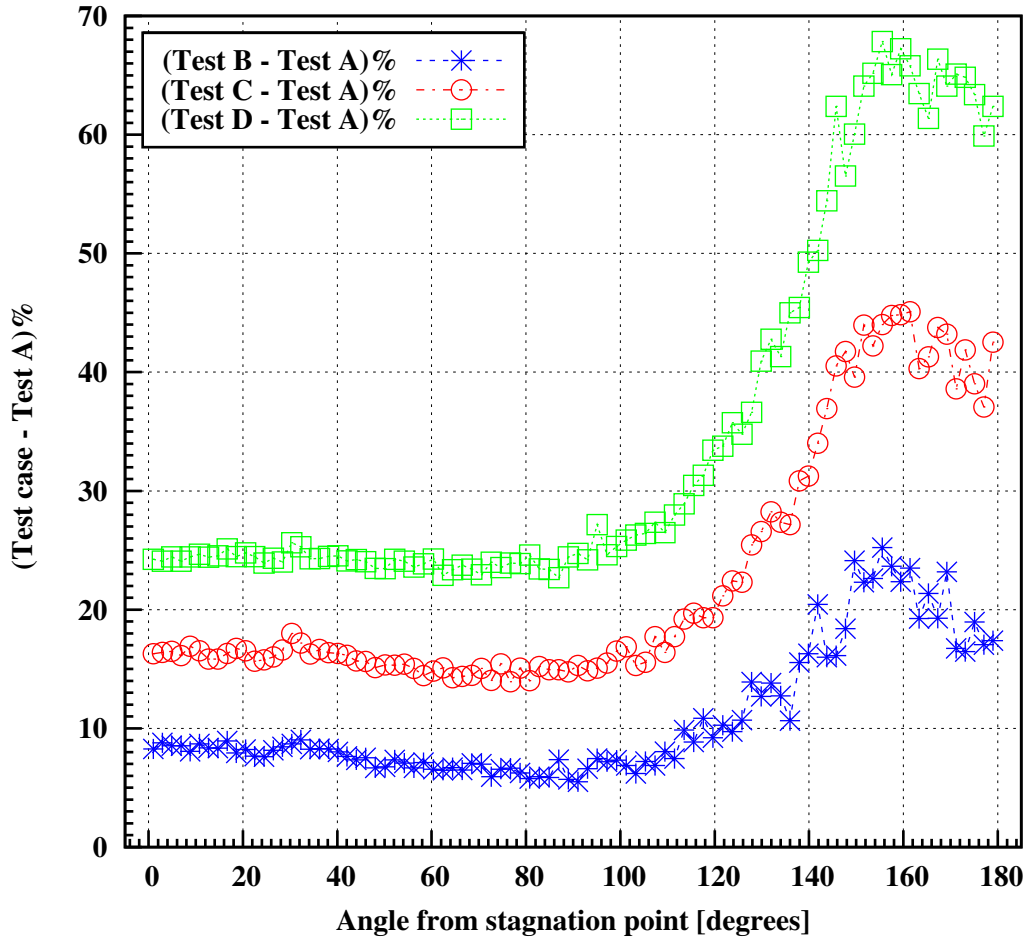

Figure 5.1: Comparison of the difference in heat transfers over the surface of the hypersonic cylinder.

Although, significant differences are noticed with the previous two properties,

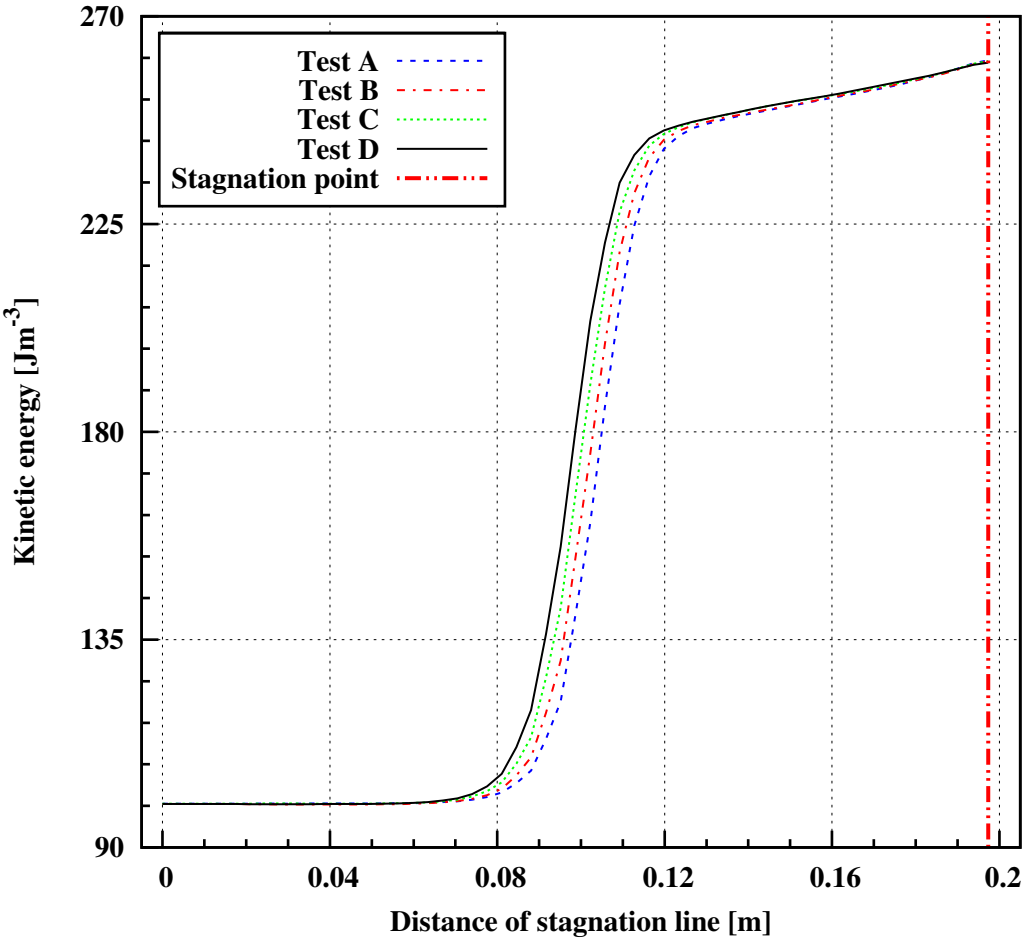

Figure 5.2: Comparison of kinetic energy along the stagnation line of the hypersonic cylinder.

the drag force increases very slightly as the temperature of the wall becomes larger. This is illustrated for tests B, C and D as a percentage difference from the benchmark test case, calculated using equation 5.2, in table 5.2. In addition, the plot of surface pressure over the cylinder in figure 5.3 calculated using equation 5.2, shows that the surface pressure has not been affected a great deal by the surface temperature apart from the cylinder afterbody. The cylinder afterbody has the largest differences but the pressures at those surface elements are very small in comparison to the cylinder forebody as shown by *Test A difference (%)* in the plot and this is determined by taking the percentage of a particular

pressure point on the surface divided by the surface pressure at the stagnation point. Since there is a small effect of surface pressure over the cylinder with different surface temperatures and especially at the forebody therefore this is what influences the small differences in drag force.

(Test B - Test A)%	0.73
(Test C - Test A)%	1.36
(Test D - Test A)%	1.94

Table 5.2: The percentage differences in drag force experienced by the hypersonic cylinder at different surface temperatures.

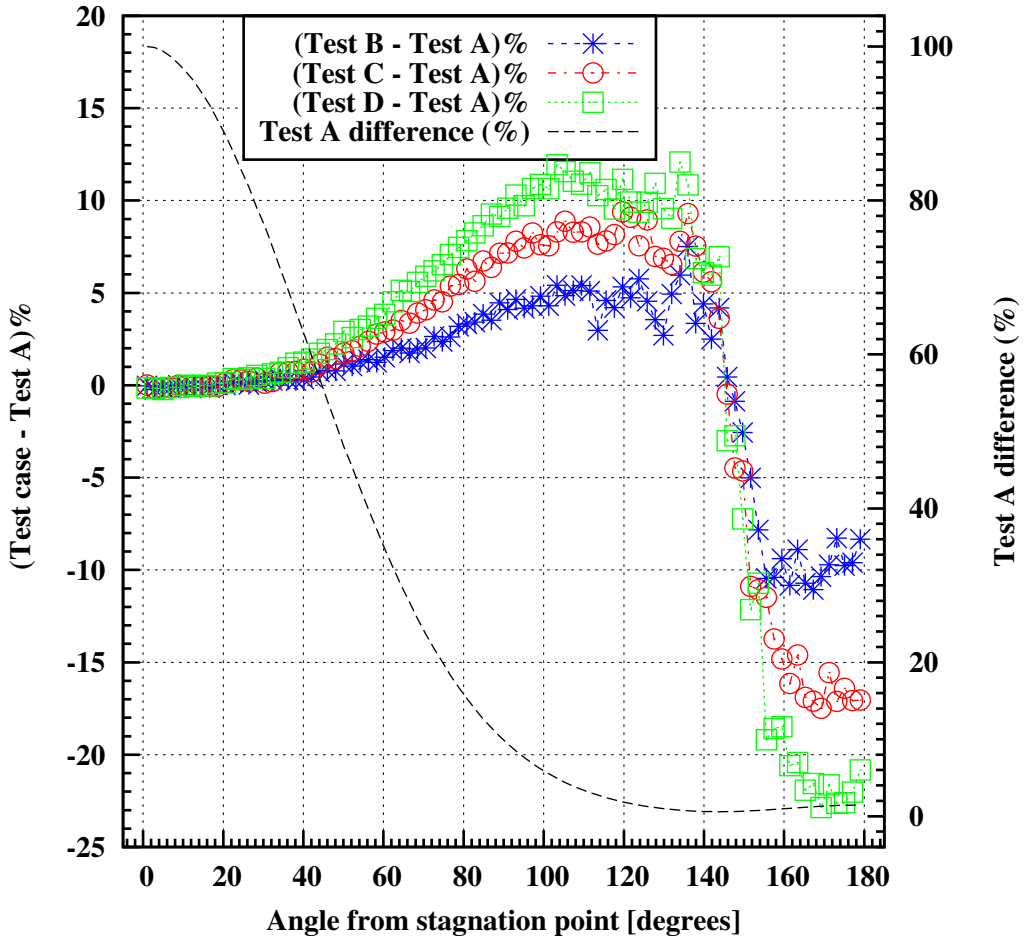

Figure 5.3: Comparison of pressure over the surface of the hypersonic cylinder.

5.2.2 Hypersonic gas flow over a blunt-body

The previous section investigated the effect of the surface temperature of the hypersonic cylinder on the aerothermodynamic properties, and it was found that the surface heat transfer reduced as the shock distance moved further away from the cylinder caused by the increase in surface temperature. In addition, as the surface temperature increased the drag increased too due to the increase in pressure at the forebody. As the hypersonic cylinder was tested at one atmospheric condition, therefore in this section the effect of the altitude is primarily investigated on the aerothermodynamic properties using different surface temperatures. Two altitudes are considered in this investigation and are based on the altitudes considered by Rault [50] to investigate the Shuttle Orbiter aerodynamics. To reduce computational costs the test case used in this investigation is a hypersonic blunt-body.

The dimensions of the hypersonic blunt-body test case are shown in figure 5.4 and is constructed in two dimensions only, this arrangement is employed for all blunt-body tests considered in this section. Figure 5.5 outlines the face definitions of each mesh cell touching the surface of the step, these definitions are used to portray the surface properties later in this section. Four tests are carried out at each free-stream condition in table 5.3 based on Rault [50] and for each test a different surface temperature is employed, the surface temperature definitions are shown in table 5.4. For all hypersonic blunt-body tests, the free-stream velocity is set to 7500 ms^{-1} and the Kn_{BLG} fixed to 0.5 - based on the length of the blunt-body. The surface properties are sampled at the same resolution as the computational domain mesh cells and the conventional eight sub-cell approach is applied at each cell for selecting possible collision pairs. The variable hard sphere model [4] is used to process the collisions while the Larsen-Borgnakke phenomenological

model [4] is used to determine the energetics of the intermolecular collisions; energy is exchanged between the translational, rotational and vibrational modes and the gas is considered as non-reacting. The gas composition and molecular properties, at a reference temperature of 273 K used for all of these tests are shown in tables 5.5 and 5.6. The system parameters and computational effort are illustrated in table 5.7.

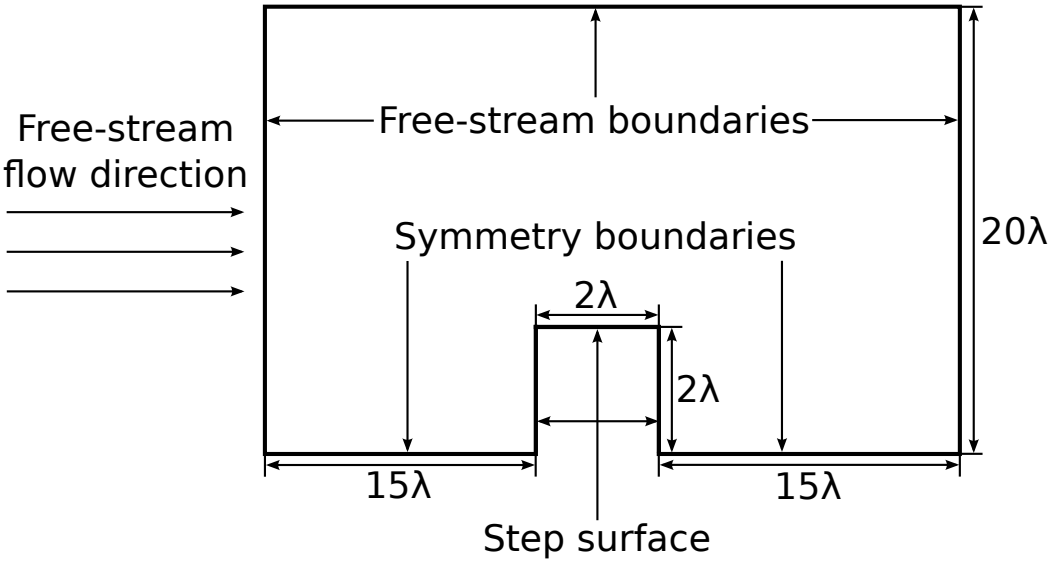

Figure 5.4: Geometry and boundary dimensions used in the simulations of hypersonic gas flows over a blunt-body (drawing not to scale).

Tests	Altitude [km]	n_∞ [m^{-3}]	T_∞ [K]
A.1, A.2, A.3 and A.4	100	1.20×10^{19}	193.7
B.1, B.2, B.3 and B.4	170	2.06×10^{16}	790.4

Table 5.3: Free-stream conditions used in the simulations of hypersonic gas flows over a blunt-body.

Surface heat transfers over the surface of the hypersonic blunt-body at 100 and 170 km are compared in figures 5.6 and 5.7, respectively. The largest differences are also plotted based on,

$$(max - min)\,\% = \left(\frac{test_{max} - test_{min}}{test_{min}}\right) \times 100, \tag{5.3}$$

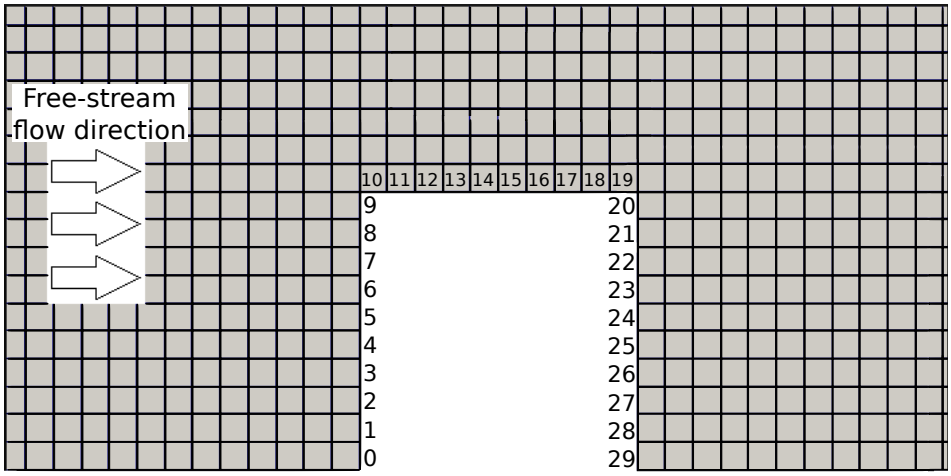

Figure 5.5: Cell face definitions on the surface of the hypersonic blunt-body. The grid represents the computational mesh.

Tests	T_W [K]
A.1 and B.1	500
A.2 and B.2	1000
A.3 and B.3	1500
A.4 and B.4	2000

Table 5.4: Surface temperatures used in the simulations of hypersonic gas flows over a blunt-body.

Altitude [km]	N_2	O_2	O
100	0.78	0.18	0.04
170	0.523	0.04	0.437

Table 5.5: Molecular compositions used in the simulations of hypersonic gas flows over a blunt-body.

Parameter	N_2	O_2	O
ω	0.74	0.77	0.8
d [m]	4.17×10^{-10}	4.07×10^{-10}	3×10^{-10}
m [kg]	46.5×10^{-27}	53.12×10^{-27}	26.56×10^{-27}

Table 5.6: Variable hard sphere model parameters, at a reference temperature of 273 K, used in the simulations of hypersonic gas flows over a blunt-body.

where $test_{max}$ and $test_{min}$ represent the maximum and minimum surface properties, respectively. The largest differences are noticed between the tests that con-

Tests	No. of particles	Time-step [s]	Average execution time per time-step [s]
A.1, A.2, A.3 and A.4	≈700000	7×10^{-7}	1.2
B.1, B.2, B.3 and B.4	≈700000	3.5×10^{-4}	1.2

Table 5.7: The system parameters and computational effort for simulating hypersonic gas flows over a blunt-body. The execution time is based on a simulation using one processor.

sidered the surface temperatures of 500 and 2000 K. For both altitudes, a similar trend is observed and the heat transfer decreases as the altitude increases. The heat transfer to the wall is reduced due to the decrease in free-stream density at the higher altitude. Furthermore, the difference between the maximum and minimum surface heat transfers at different surface temperatures is smaller at the front and top of the blunt-body in comparison to the forebody of the cylinder. The afterbody of the blunt-body has a larger heat transfer difference at the wall than the cylinder afterbody and this may be explained by the influence of the large expansion region created behind the blunt-body. Since the particle velocities in this region are very small the surface temperature will have a greater influence on the energy of the particles reflecting off the surface.

Furthermore, a similar trend in differences are also noticed with the surface pressures on the blunt-body but the magnitudes are smaller in comparison. In particular the front side has a maximum difference of less than 1%, except for face nine in both tests - the difference at this face rises to approximately 1.6%. As a result of the small surface pressure differences the drag forces of all tests at each altitude are in close agreement, as illustrated in table 5.8. The main reason for the small differences in the properties at different surface temperatures is due to the large free-stream velocity. Therefore the incident energy to the surface in particular at the front of the blunt-body is very large in comparison to

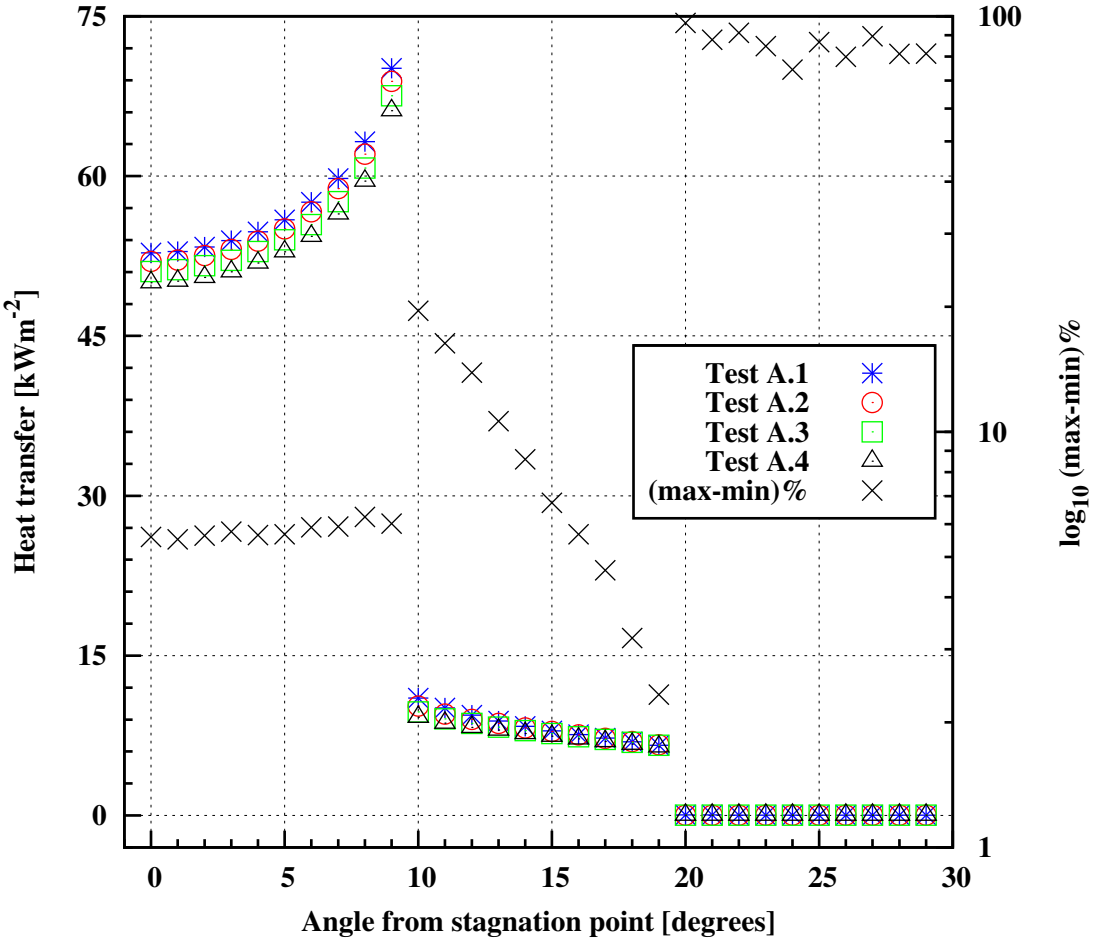

Figure 5.6: Comparison of heat transfer over the surface of the hypersonic blunt-body at 100 km.

the reflected energy. This is investigated further by considering the blunt-body at 100 km, as used in the above tests, but with a free-stream velocity of 500

Test	Drag force [N]	Test	Drag force [N]
A.1	1806.77	B.1	1486.76
A.2	1806.95	B.2	1487.57
A.3	1806.55	B.3	1487.04
A.4	1806.97	B.4	1486.82

Table 5.8: Drag forces of blunt-body investigations.

ms^{-1}. For this study, surface temperatures of 500 and 2000 K are considered. Figure 5.8 shows the non-dimensionalised number density of both tests and the

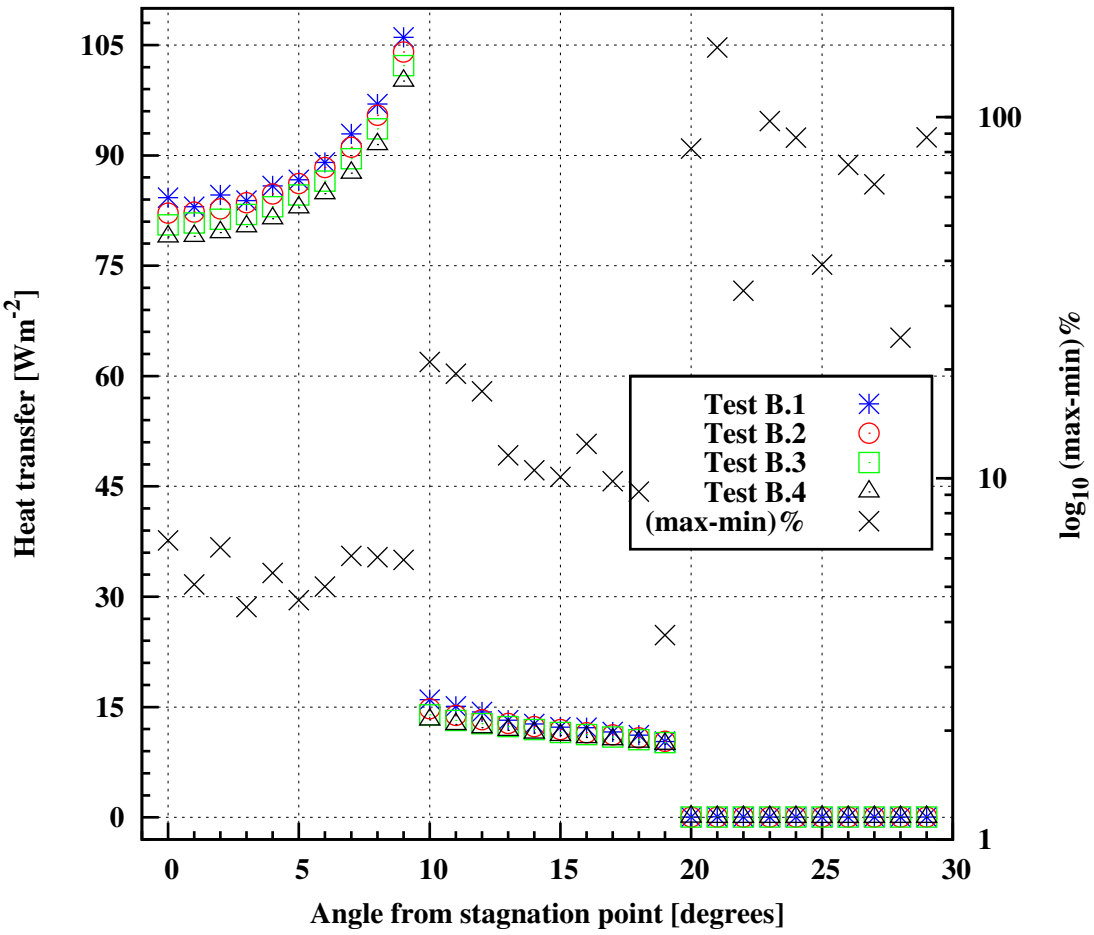

Figure 5.7: Comparison of heat transfers over the surface of the hypersonic blunt-body at 170 km.

leading shock appears further away from the blunt-body at 2000 K than at 500 K surface temperature - a similar phenomenon noticed previously with the hypersonic cylinder. As a result the drag force is greater by 12% at 2000 K than 500 K.

5.3 Verification and validation of the DWTM

The previous section suggests that a fixed temperature over the entire surface is inadequate for re-entry problems as the properties, in certain cases, are dependent upon the wall temperature. Therefore, this section outlines a DWTM

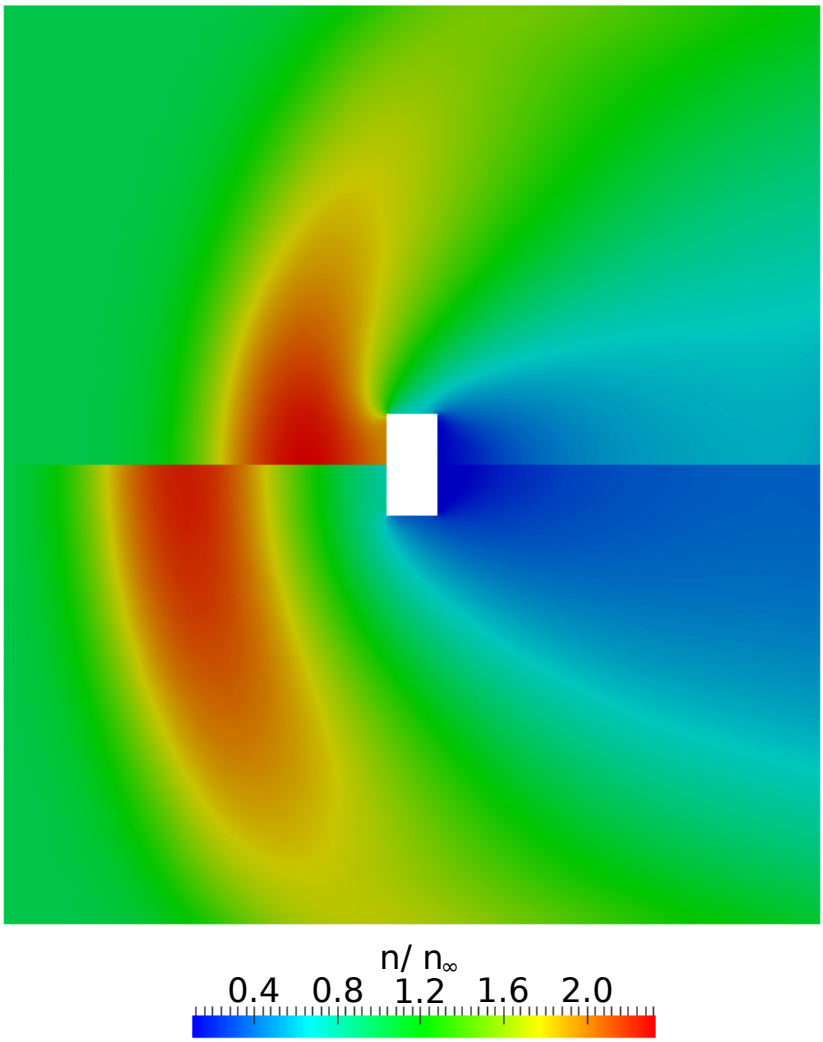

Figure 5.8: Comparison of non-dimensionalised number density over the blunt-body. The figure at the top represents the surface at a wall temperature of 500 K and the bottom at 2000 K.

implemented in *dsmcFoam* to predict a temperature distribution over the surface of an object. The results in this study are all based on particles reflecting off the surface in a fully diffuse fashion, however the dynamic wall model may also work for walls that reflect particles in a mixed specular and diffuse fashion.

.

5.3.1 Dynamic wall temperature model

The DWTM of *dsmcFoam* is applicable for walls that experience convection, radiation and no conduction and is based on the theory of thin walls where the surface temperature is formulated by the energy of the particles hitting and reflecting off the surface. This energy may include the translational, rotational and vibrational modes and the particles are reflected according to the biased Maxwellian distribution based on the new updated wall temperature.

Furthermore, for the surface of thin walls, built up by individual planar facets and each facet modelled with a thermal node i, Haas [116] describes the energy balance as,

$$\dot{q}_i(t) - \epsilon_i \sigma \left(T_i^4 - T_{DS}^4\right) - \sum_j (k_t)_{i,j} (T_i - T_j) = h_i \frac{dT_i}{dt}, \tag{5.4}$$

where each node has a temperature $T_i(t)$, heat capacity h_i, radiating emissivity ϵ_i, heat flux $\dot{q}_i(t)$ and a thermal conductivity $(k_t)_{i,j}$ that connects nodes i and j. T_{DS} is the deep-space temperature, t is the time and σ is the Stefan-Boltzmann constant.

By considering the front (f) and back (b) sides of the thin wall, and assuming that both sides have one facet each and neglecting k laterally along the thin wall surface, the energy balance for face f and b become,

$$\dot{q}_f^{net}(t) - \epsilon_f \sigma \left(T_f^4 - T_{DS}^4\right) - k_t (T_f - T_b) = h_f \frac{dT_f}{dt} \tag{5.5}$$

and

$$\dot{q}_b^{net}(t) - \epsilon_b \sigma \left(T_b^4 - T_{DS}^4\right) + k_t (T_f - T_b) = h_b \frac{dT_b}{dt} \tag{5.6}$$

respectively. The coefficients h and k_t also account for the thickness and density of the material. $\dot{q}_f^{net}(t)$ and $\dot{q}_b^{net}(t)$ are the convective heat fluxes incident to the front and back sides of the wall, respectively. Under hypersonic conditions

$\dot{q}_b^{net}(t)$ may be neglected. The heat flux on the back surface is neglected because it negligible in comparison to the front surface, as the back surface is in the wake and therefore has lower density than the front surface. The lower density coupled with particles having lower energy results in a much lower heat flux on the back than the front. For the DWTM of *dsmcFoam* the conduction term is negated and the above two equations condense to,

$$\dot{q}_{c-f}^{net}(t) - \epsilon_{c-f}\sigma\left(T_{c-f}^4 - T_{DS}^4\right) = h_{c-f}\frac{dT_{c-f}}{dt} \tag{5.7}$$

at each cell-face (c-f) on the surface. The conduction heating is very important to the thermal response of the material and therefore will be looked into in future work. For all studies in this chapter T_{DS} is set to 0 K and the transient term on the right hand side of the above equation will have no effect on the simulations as they all reach steady-state. Therefore, properties such as the thermal mass that is accounted for in the heat capacity can be ignored.

A step-by-step procedure, for using the dynamic wall temperature model efficiently, is shown in figure 5.9. Step 1 in this procedure is setting the wall temperature based on equation 5.1, this temperature is similar to the stagnation point of high speed bodies under large Kn flow regimes. It is important to note that this procedure is only efficient in certain simulations, mostly when the surface temperature is close to the initial guess. Also, the converged temperature in step 3 is dependent on the rarefaction, if in the case that a very small number of particles hit the surface or even in the case that no particles hit the surface during a time-step then this step can be costly in time.

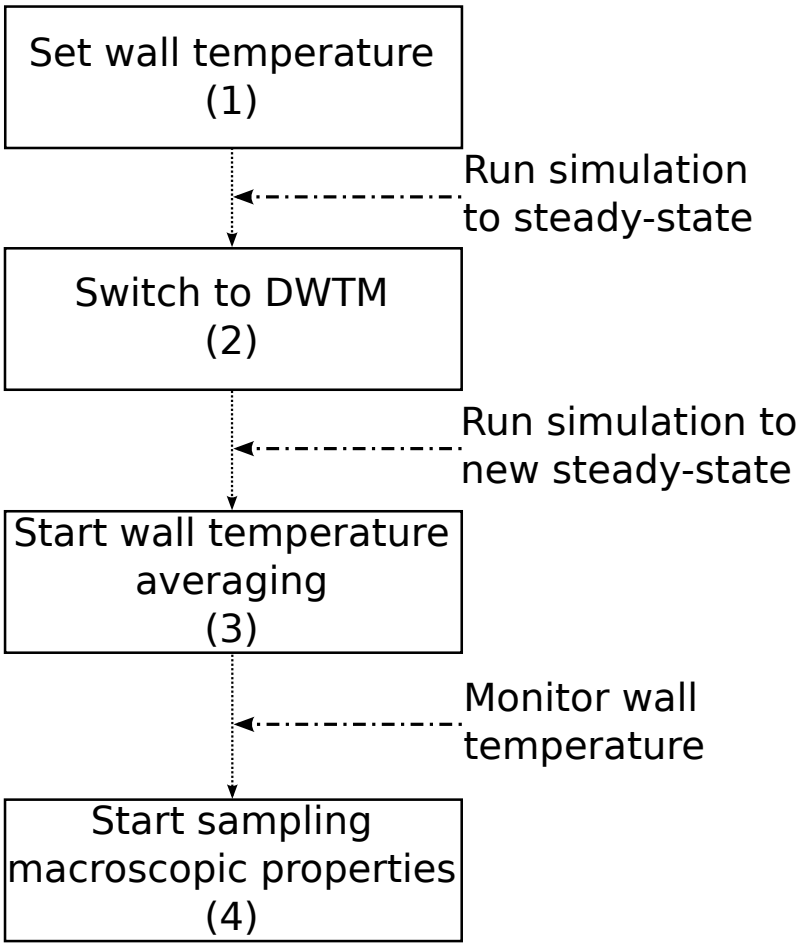

Figure 5.9: Step-by-step procedure for steady-state simulations using the DWTM.

5.3.2 Analytical solution

The analytical solutions used in the next section to verify the DWTM using free-molecular theory are,

$$\dot{q}_{inc} = \epsilon\sigma \left(T_W\right)^4_{AS1} \tag{5.8}$$

and

$$\dot{q}_{net} = \epsilon\sigma \left(T_W\right)^4_{AS2}, \tag{5.9}$$

where $\dot{q}_{inc}$ and $\dot{q}_{net}$ are calculated from equations B.26 and B.33, respectively. Equations 5.8 and 5.9 are termed analytical solution 1 (AS1) and analytical solution 2 (AS2), respectively. Free-molecular theory is derived in Appendix B and

the resulting equations can be derived directly from the boundary condition that is implemented in *dsmcFoam*.

5.3.3 Verification of the DWTM with free-molecular theory

The analytical solutions derived in the previous section are used to verify the DWTM of *dsmcFoam* in this section. AS1 is used in this study as it represents one of the techniques in defining wall temperatures in DSMC calculations as discussed in section 5.2. And AS2 is used as it represents both the incident and reflected energies, in addition the incident energy accounts for both the thermal and kinetic forms.

The verification study involves several *dsmcFoam* simulations of free-molecular gas flows towards a flat plate of no thickness and length 0.01λ, as shown in figure 5.10. Also shown in this figure are the dimensions of the computational domain. Velocities in tables 5.9, 5.10 and 5.11 are considered in the study and these are simulated at three altitudes. These altitudes are 100, 170 and 250 km. The free-stream number densities and temperatures for the three altitudes are illustrated in tables 5.12 and 5.13, respectively, and are obtained from the U.S. standard atmosphere [117]. Some of the *dsmcFoam* parameters are also illustrated in the latter table. The molecular properties for Nitrogen, Oxygen and atomic Oxygen are illustrated in table 5.6 and the remaining properties are illustrated in table 5.14. The Kn_{BLG} is fixed to one hundred for each test, as the results from the *dsmcFoam* calculations are compared against analytical solutions derived from free-molecular theory. The emissivity is set to 0.83 and is similar to the value defined for re-entry vehicles [118, 119].

The results from the verification study at altitudes of 100, 170 and 250 km are

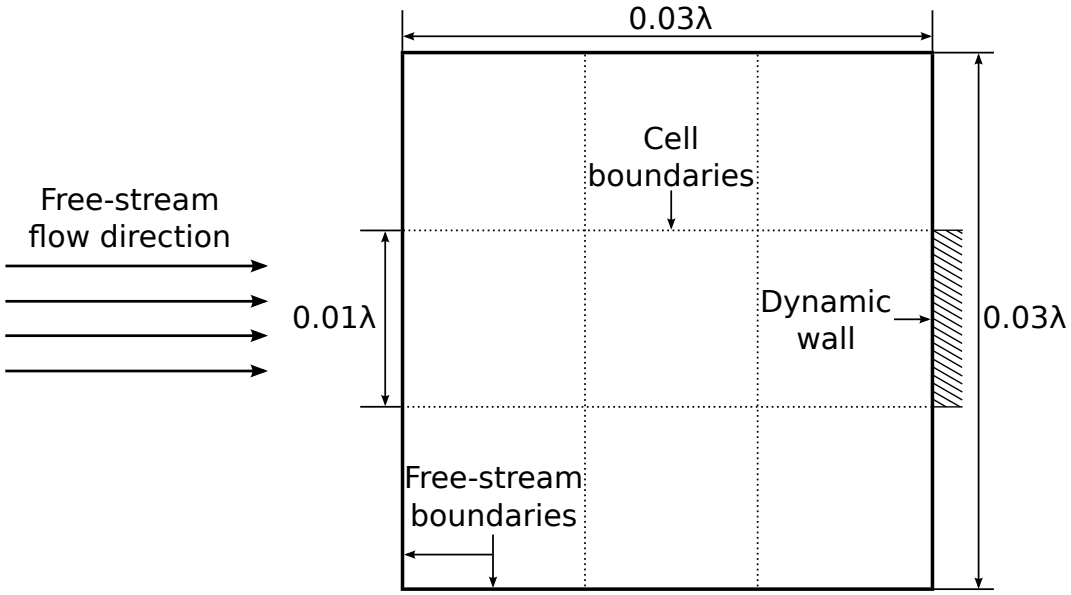

Figure 5.10: Geometry and boundary dimensions used in the simulations of free-molecular gas flows towards a two-dimensional flat plate (drawing not to scale).

U_∞ [ms^{-1}]	ζ	U_∞ [ms^{-1}]	ζ
0.155	4.586×10^{-4}	2500	7.396
0.5	1.479×10^{-3}	3000	8.875
1	2.958×10^{-3}	3750	11.094
3.75	1.109×10^{-2}	4500	13.313
7.5	2.219×10^{-2}	5250	15.532
18.75	5.547×10^{-2}	6000	17.751
37.5	0.111	6750	19.970
75	0.222	7500	22.189
200	0.592	8250	24.407
375	1.109	9000	26.626
1500	4.438	9750	28.845
2000	5.917	10500	31.064
2250	6.657	15000	44.377

Table 5.9: Free-stream velocities and corresponding speed ratios used in the simulations of free-molecular gas flows towards a two-dimensional flat plate at 100 km.

in figures 5.11, 5.12 and 5.13, respectively. The differences are plotted as absolute

U_∞ [ms^{-1}]	ζ	U_∞ [ms^{-1}]	ζ
0.155	2.104×10^{-4}	2500	3.393
0.5	6.786×10^{-4}	3000	4.072
1	1.357×10^{-3}	3750	5.090
3.75	5.090×10^{-3}	4500	6.107
7.5	1.018×10^{-2}	5250	7.125
18.75	2.545×10^{-2}	6000	8.143
37.5	5.090×10^{-2}	6750	9.161
75	0.102	7500	10.179
200	0.271	8250	11.197
375	0.509	9000	12.215
1500	2.036	9750	13.233
2000	2.714	10500	14.251
2250	3.054	15000	20.358

Table 5.10: Free-stream velocities and corresponding speed ratios used in the simulations of free-molecular gas flows towards a two-dimensional flat plate at 170 km.

U_∞ [ms^{-1}]	ζ	U_∞ [ms^{-1}]	ζ
0.155	1.716×10^{-4}	2500	2.768
0.5	5.537×10^{-4}	3000	3.322
1	1.107×10^{-3}	3750	4.153
3.75	4.153×10^{-3}	4500	4.983
7.5	8.305×10^{-3}	5250	5.814
18.75	2.076×10^{-2}	6000	6.644
37.5	4.153×10^{-2}	6750	7.475
75	8.305×10^{-2}	7500	8.305
200	0.221	8250	9.136
375	0.415	9000	9.966
1500	1.661	9750	10.797
2000	2.215	10500	11.627
2250	2.492	15000	16.610

Table 5.11: Free-stream velocities and corresponding speed ratios used in the simulations of free-molecular gas flows towards a two-dimensional flat plate at 250 km.

values in all 3 figures using the definition,

$$(dsmcFoam - AS1 \; or \; AS2)\,\% = \frac{(dsmcFoam - AS1 \; or \; AS2)}{dsmcFoam} \times 100. \qquad (5.10)$$

Altitude [km]	N_2	O	O_2	Ar	He	H
100	92100	4298	21510	950.1	1.133	0
170	107	89.96	8.277	0.1163	0.1676	0.002386
250	4.826	13.88	0.2482	0.001546	0.0969	0.00121

Table 5.12: Free-stream number densities used in the simulations of free-molecular gas flows towards a two-dimensional flat plate. The number densities in this table are presented in individual forms and as n$\times 10^{-14}$ [m^{-3}].

Altitude [km]	T_∞ [K]	Time-step [s]	Average no. of DSMC particles
100	193.7	1×10^{-8}	385000
170	790.4	1×10^{-5}	630000
250	941.33	1×10^{-4}	700000

Table 5.13: Free-stream temperature and *dsmcFoam* parameters used in the simulations of free-molecular gas flows towards a two-dimensional flat plate.

Parameter	Ar	He	H
ω	0.81	0.66	0.8
d [m]	4.17×10^{-10}	2.33×10^{-10}	2.5×10^{-10}
m [kg]	66.3×10^{-27}	6.65×10^{-27}	1.67×10^{-27}

Table 5.14: Variable hard sphere model parameters, at a reference temperature of 273 K, used in the simulations of free-molecular gas flows towards a two-dimensional flat plate.

The comparisons are in excellent agreement between *dsmcFoam* and AS1 at hypersonic velocities. However, as the velocity decreases to supersonic and subsonic large differences between the analytical solutions and *dsmcFoam* start to appear. At these velocities the differences are much greater between AS1 and *dsmcFoam*. The differences are larger because the thermal component of the particles is more significant at the lower velocities and this is not accounted for in AS1. Although AS2 accounts for the thermal component differences with *dsmcFoam* still exist but the differences are a great deal less than AS1, and the largest differences decrease as the altitude increases. The differences between AS2 and *dsmcFoam* are 9.293, 6.281 and 3.433% at 100, 170 and 250 km, respectively.

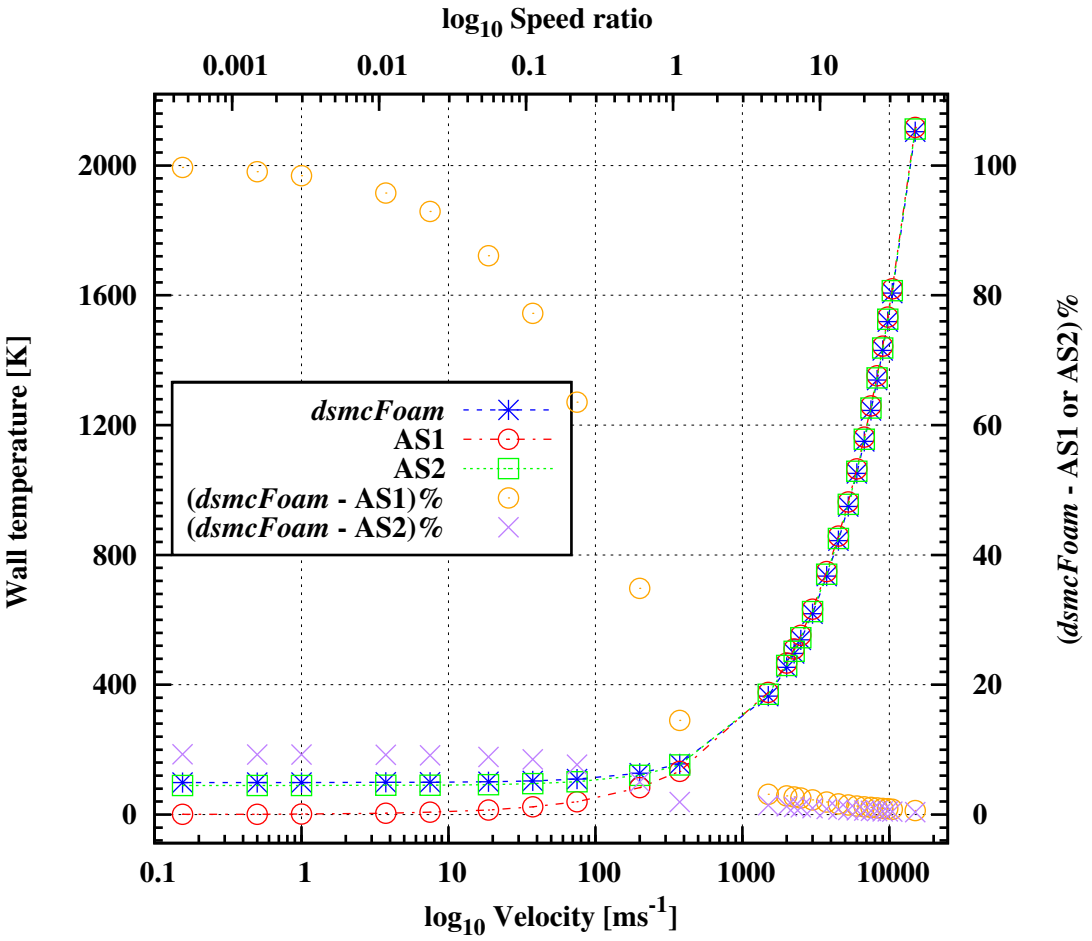

Figure 5.11: Verification of surface temperatures from the *dsmcFoam* simulations of free-molecular gas flows towards a two-dimensional flat plate using analytical definitions, at 100 km.

5.3.4 Further investigations into the verification of the DWTM

The previous section compared the analytical solutions derived in section B with the DWTM of *dsmcFoam*. Excellent agreement was found with both these methods at high velocities, but large differences started to exist at the lower velocities. This section investigates these by looking at the surface heat transfers in individual and complete forms, i.e. incident, reflected and net, and compares these to free-molecular theory. It also outlines a possible remedy to the *dsmcFoam* simu-

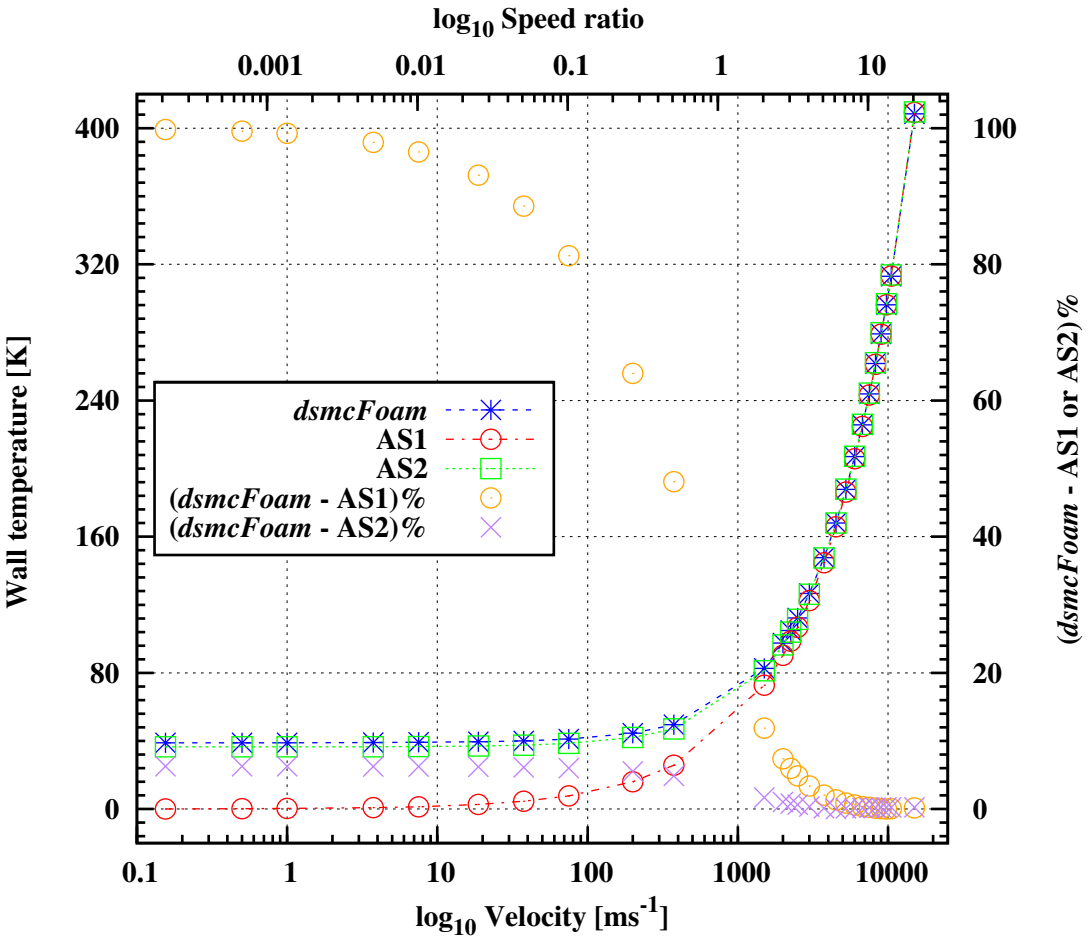

Figure 5.12: Verification of surface temperatures from the *dsmcFoam* simulations of free-molecular gas flows towards a two-dimensional flat plate using analytical definitions, at 170 km.

lations at low velocities by extending the distance of the boundaries. In addition, all tests carried out in the previous section experienced collisions but the number of collisions was very small. The effect of the collisions is also investigated in this section.

Firstly, the analytical reflected heat transfer becomes more significant at lower velocities as shown in figure 5.14 for 170 and 250 km, therefore it is initially thought that the differences between AS2 and *dsmcFoam* at these velocities is caused by the reflected flux and as a result requires an analytical definition rather than partly taken from the *dsmcFoam* calculations. To determine the root cause

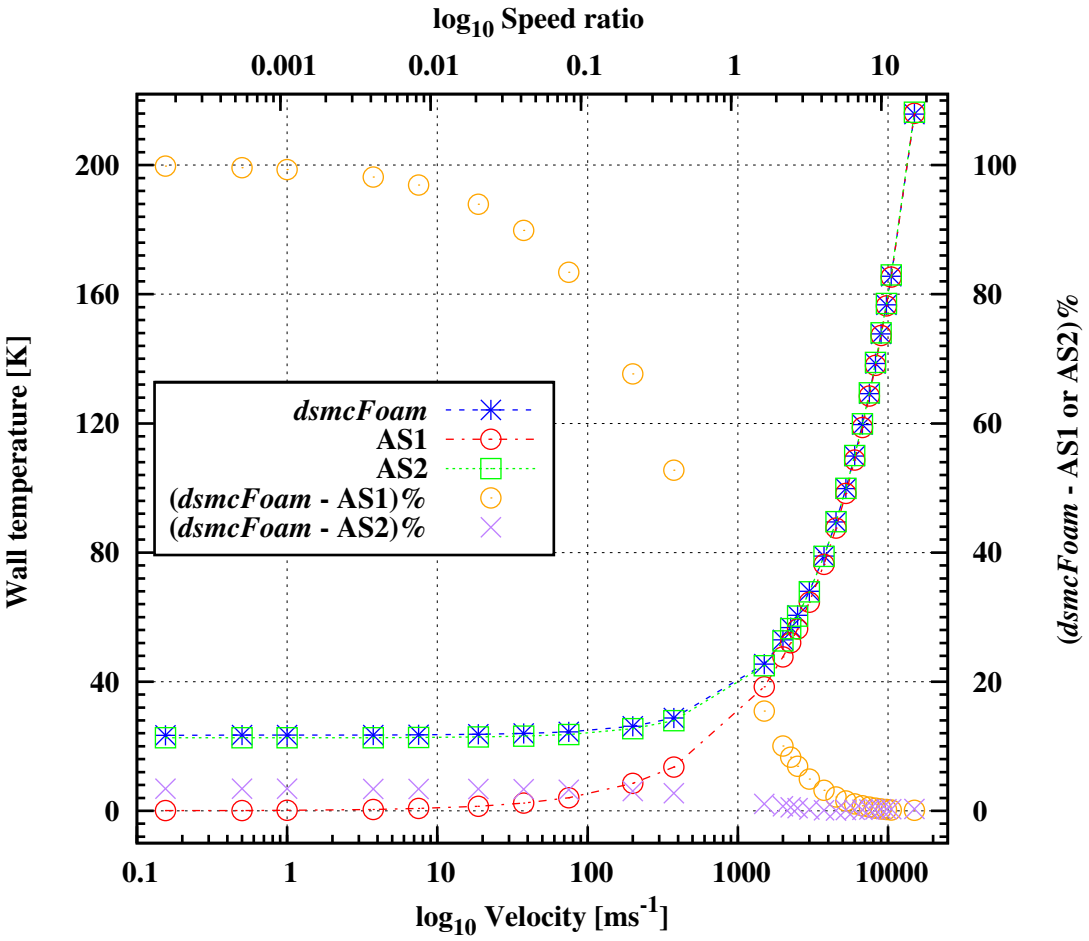

Figure 5.13: Verification of surface temperatures from the *dsmcFoam* simulations of free-molecular gas flows towards a two-dimensional flat plate using analytical definitions, at 250 km.

of the differences, the surface heat transfers are computed in individual and complete forms for 100 and 250 km of the test cases considered in the previous section as shown in figures 5.15 and 5.16, respectively. However, this shows the incident surface heat transfers from the *dsmcFoam* calculations are greater than the analytical solution but the differences reduce as the temperature increases, and the same phenomenon is noticed for the reflected and net heat transfers. This suggests that it is not only the reflected temperature that is the cause of the surface temperature differences with AS2 and *dsmcFoam* in the previous section. By resolving the incident fluxes the reflected fluxes will be similar to the corresponding

analytical definitions as the reflected energy of the particles is based on the wall temperature, and this wall temperature is based on the net heat transfer.

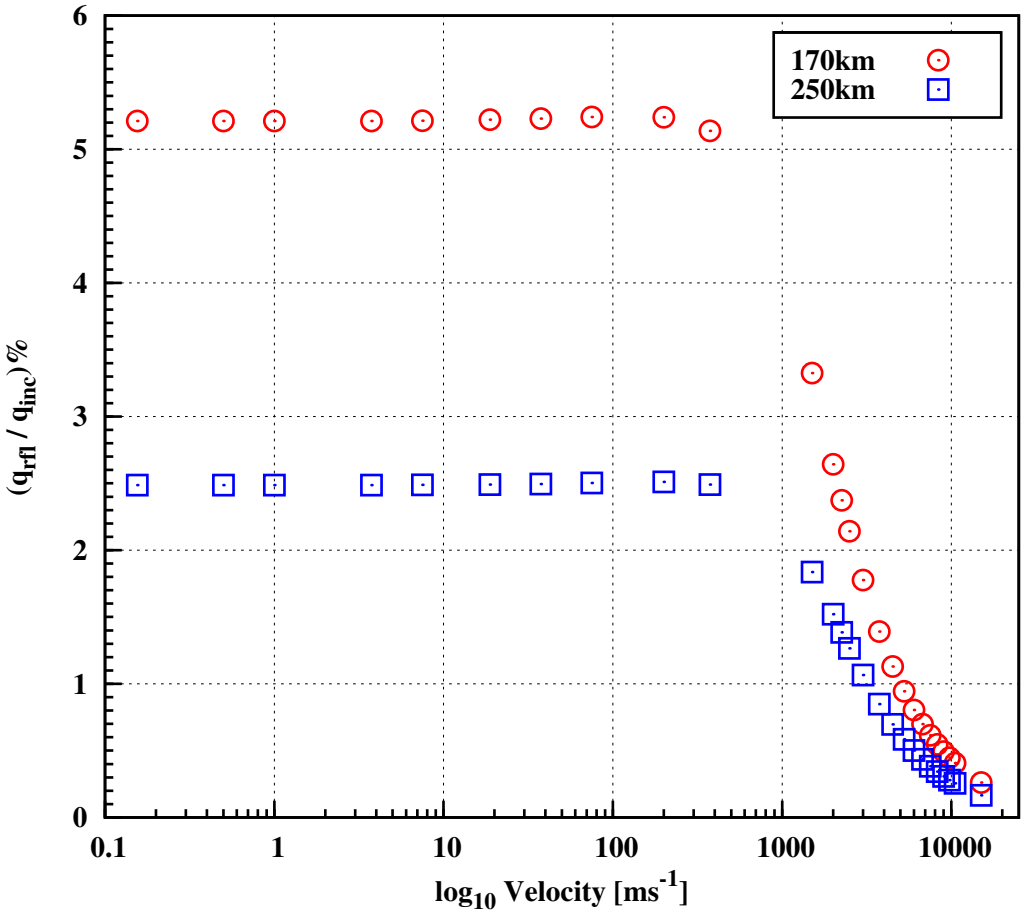

Figure 5.14: The significance of the reflected heat transfer at 170 and 250 km.

The effect of the collisions, in the *dsmcFoam* simulations, are also investigated. Two tests from the previous section at 100 km are used for the investigation; the velocities considered are 200 and 1500 ms^{-1}. The differences between the wall temperatures of both tests with collisions and no collisions are within 0.2%. Therefore, this is not the cause of the differences between *dsmcFoam* and AS2.

Finally, the boundaries are investigated. Table 5.15 illustrates the effect of the computational boundaries on the surface temperatures obtained by the DWTM of *dsmcFoam*. As the computational domain increases the wall temperature ob-

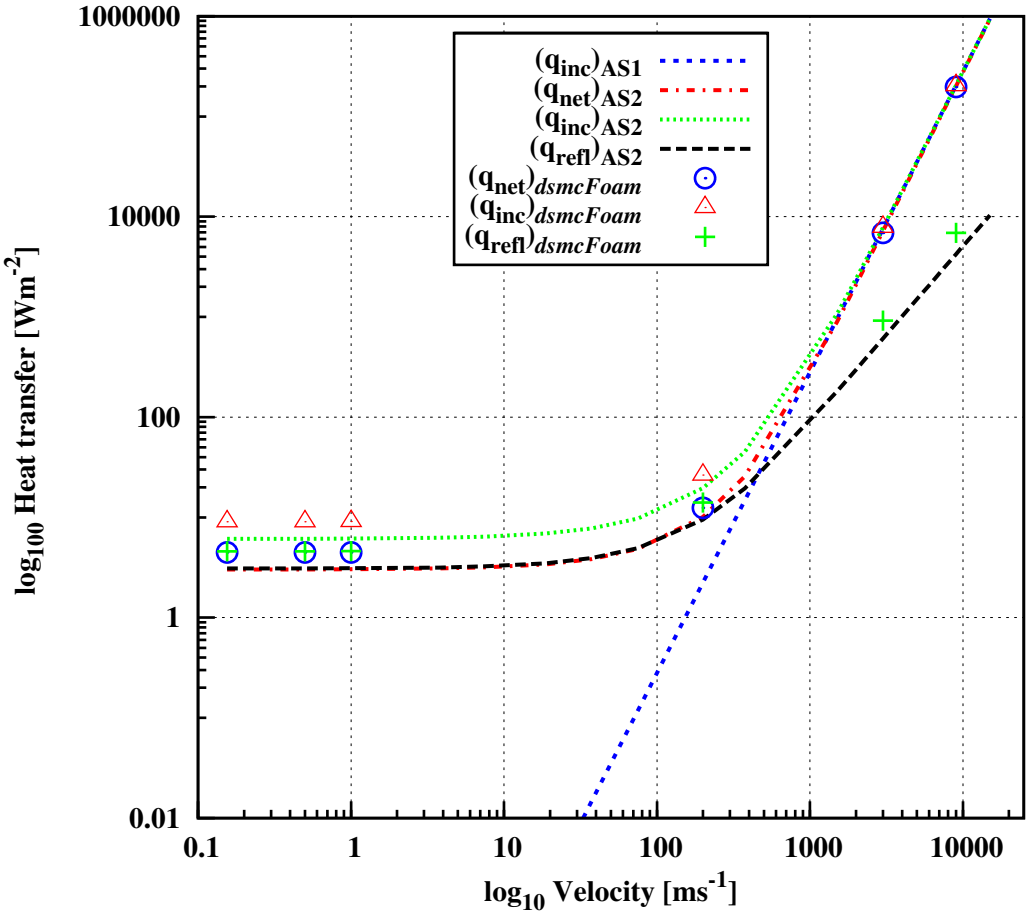

Figure 5.15: Surface heat transfers in individual and complete forms obtained from *dsmcFoam* and analytical solutions, at 100 km.

tained from the simulations become closer to AS2. Therefore, this suggests the computational boundaries have to be further away from the wall, in comparison to the setup in the previous section, to resolve the inflow boundaries correctly. Further studies of this will be necessary to resolve this issue.

5.3.5 Particle sensitivity investigation on the DWTM

The investigation on the sensitivity of the number particles in the system is necessary to determine the influence this has on the DWTM. For each of the simulations carried out under the validation study of the DWTM at 100 km, in

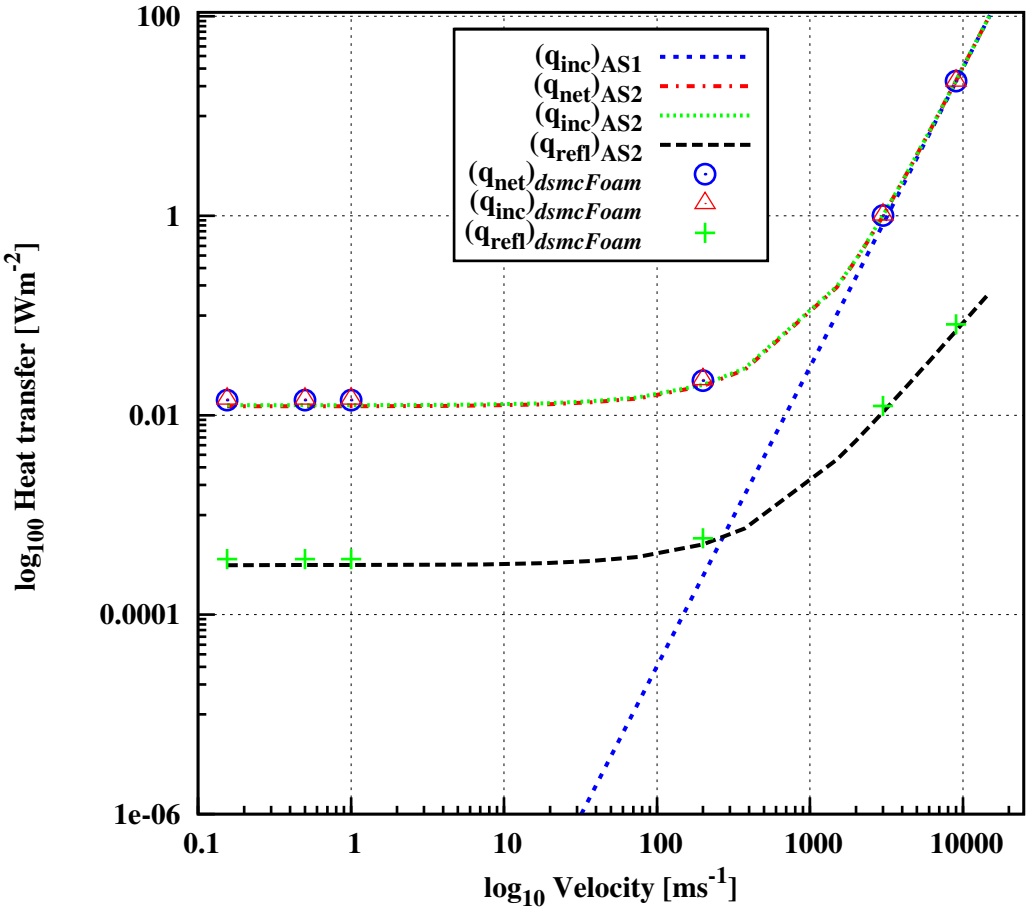

Figure 5.16: Surface heat transfers in individual and complete forms obtained from *dsmcFoam* and analytical solutions, at 250 km.

Test	Boundary dimensions	*dsmcFoam* T_W [K]	(*dsmcFoam* - AS2)%
100 km, 1500 ms^{-1}	0.03×0.03λ	365.159	1.439
100 km, 1500 ms^{-1}	1×2λ	365.874	1.231
100 km, 1500 ms^{-1}	2×4λ	366.755	0.975
100 km, 9000 ms^{-1}	0.03×0.03λ	1429.908	0.507
100 km, 9000 ms^{-1}	10×20λ	1437.270	0.042

Table 5.15: The effect of the boundary dimensions on the wall temperature obtained from the DWTM of *dsmcFoam*.

section 5.3.3, on average 385000 DSMC particles were used. For this section the number of particles in the system range from 1313 to 662146 and this is tested

using one of the test conditions considered in section 5.3.3. This test condition has a free-stream velocity of 10500 ms^{-1} at an atmosphere of 100 km. The wall temperatures are obtained, from *dsmcFoam*, after:

- 1000,
- 5000,
- 10000,
- 100000, and
- 300000 sampling time-steps after steady-state,

and are compared in figure 5.17. This figure increases the confidence in the DWTM implementation as it shows the wall temperature resolves to approximately the same value using a range of particles in the system. The *resolved solution* is also shown in this graph and is based on 662146 particles after 300000 sampling time-steps and is approximately 0.35% smaller than AS2. In addition and as expected, the number of time-steps required by *dsmcFoam* to resolve the wall temperature increases as the number of particles assigned to the system decreases. Table 5.16 illustrates the differences reduce for all systems as the number of sampling time-steps increase, and figure 5.18 shows the results that have the largest differences. The differences are calculated as,

$$Difference\,(\%) = \frac{(Test - Resolved\ solution)}{Resolved\ solution} \times 100, \tag{5.11}$$

where *Test* represents each system of particles. The differences for all systems are very small and it becomes less than roughly 0.1% after 5000 time-steps. In addition, the systems with 2611 particles and above produce a difference less than 0.075% after 1000 sampling time-steps. Furthermore, it is more efficient

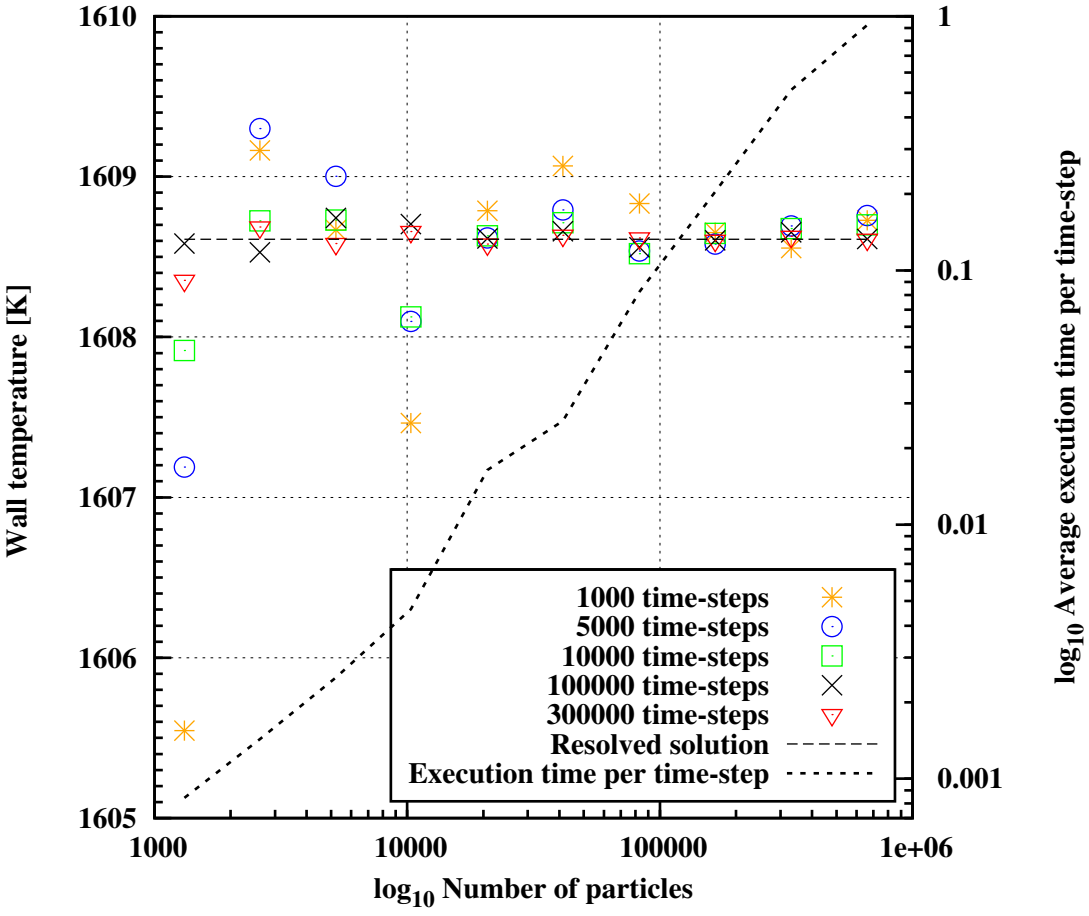

Figure 5.17: Wall temperature based on the number of DSMC particles and sampling time-steps.

to run with 2611 particles for 1000 sampling time-steps than 1313 particles for 5000 sampling time-steps to achieve a difference of 0.0884 or less and the total execution times are 0.8403 and 7.151 s, respectively. In addition, the average execution times per sampling time-step for all systems are presented in figure 5.17.

No. of particles	1000	5000	10000	100000	300000
1313	-0.1905	-0.0884	-0.0431	-1.681×10^{-3}	-1.600×10^{-2}
2611	0.0344	0.0429	0.0071	-5.071×10^{-3}	4.697×10^{-3}
5219	0.0036	0.0244	0.0074	8.188×10^{-3}	-1.688×10^{-3}
10327	-0.0712	-0.0319	-0.0301	5.843×10^{-3}	2.969×10^{-3}
20761	0.0110	0.0005	0.0013	3.088×10^{-4}	-1.903×10^{-3}
41308	0.0284	0.0114	0.0064	3.080×10^{-3}	1.524×10^{-3}
82928	0.0138	-0.0045	-0.0056	-3.134×10^{-3}	5.280×10^{-4}
165372	0.0025	-0.0019	0.0023	-4.894×10^{-4}	-4.250×10^{-4}
330838	-0.0035	0.0052	0.0041	2.660×10^{-3}	-1.097×10^{-3}
662146	0.0073	0.0091	0.0056	8.989×10^{-5}	0

Table 5.16: Differences based on the number of DSMC particles and sampling time-steps for all systems.

5.3.6 Validation of the DWTM with Stardust aerothermodynamics

The DWTM of *dsmcFoam* is validated using the Stardust aerothermodynamic calculations, based on non-reacting and non-ablation flows, performed by Zhong *et al.* [3] using a modified DSMC SMILE technique [120] with a radiative wall boundary model similar to the DWTM. Zhong *et al.*'s approach is not built into the solver and they have to initially run a DSMC simulation using a defined wall temperature to obtain a surface heat transfer distribution, this distribution is then equated to the right hand side of equation 5.9 to calculate the new surface temperature distribution. Using the new surface temperature distribution a second DSMC simulation is run to determine a new surface heat transfer distribution. This procedure is repeated until the surface temperature has converged.

The Stardust configuration and test conditions are shown in figure 5.19 and table 5.17, respectively. Although the conditions in this table are often considered to be very expensive for re-entry vehicles to be simulated with good DSMC

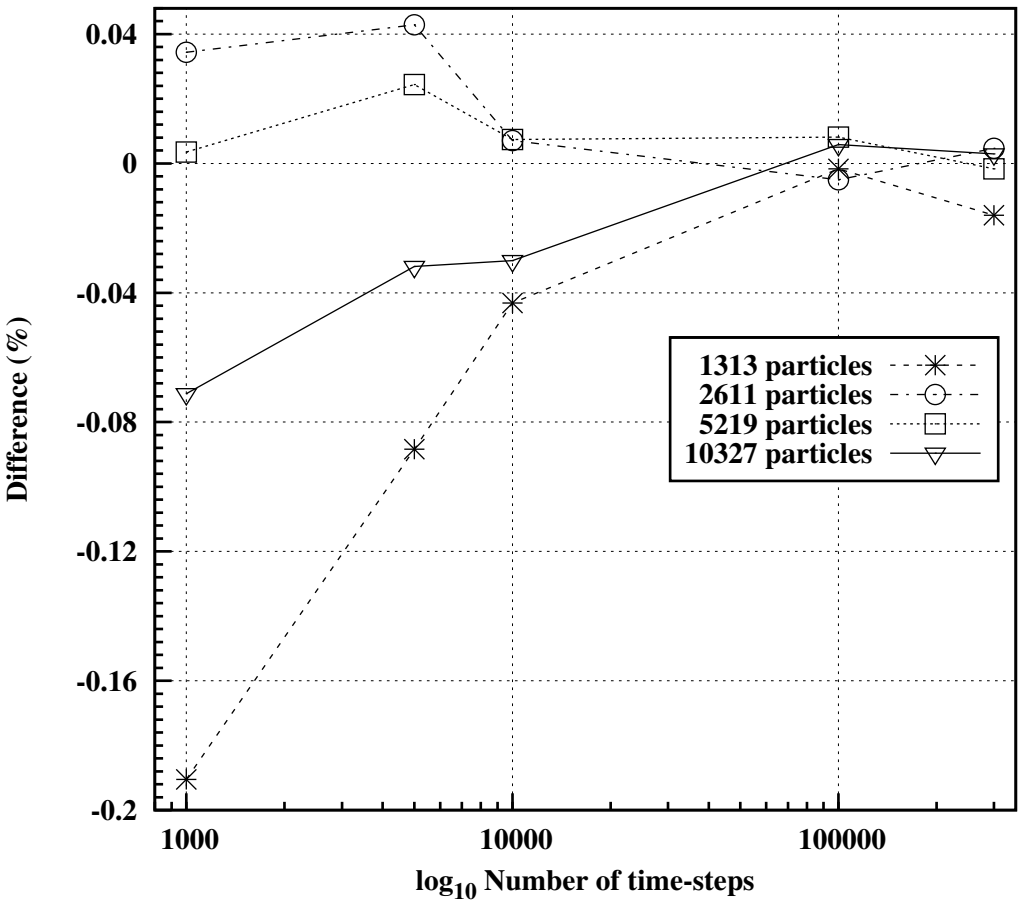

Figure 5.18: Differences based on the number of DSMC particles and sampling time-steps for four systems containing the smallest number of particles.

practice, the Stardust computational domain used by *dsmcFoam* is built up by mesh cells that have sizes roughly one mean free path long but they adopt the conventional eight sub-cell algorithm and therefore the particle collision pairs are chosen within dimensions smaller than the free-stream mean free path. Furthermore, *dsmcFoam* employs a quarter geometry system with symmetry boundary conditions and Zhong *et al.* employed an axi-symmetric configuration. In addition and as considered by Zhong *et al.*, a diffuse wall boundary condition is assumed and the VHS and Larsen-Borgnakke models are used to simulate the collisions and distribute post-collision energy between kinetic, rotational and vi-

brational modes, respectively. Also, high temperature VHS parameters [121] are used in the system. The emissivity is set to 0.9 as considered by Zhong *et al.* and recommended by Covington *et al.* [118]. Further information on the system setup for both *dsmcFoam* and Zhong *et al.* is illustrated in table 5.18.

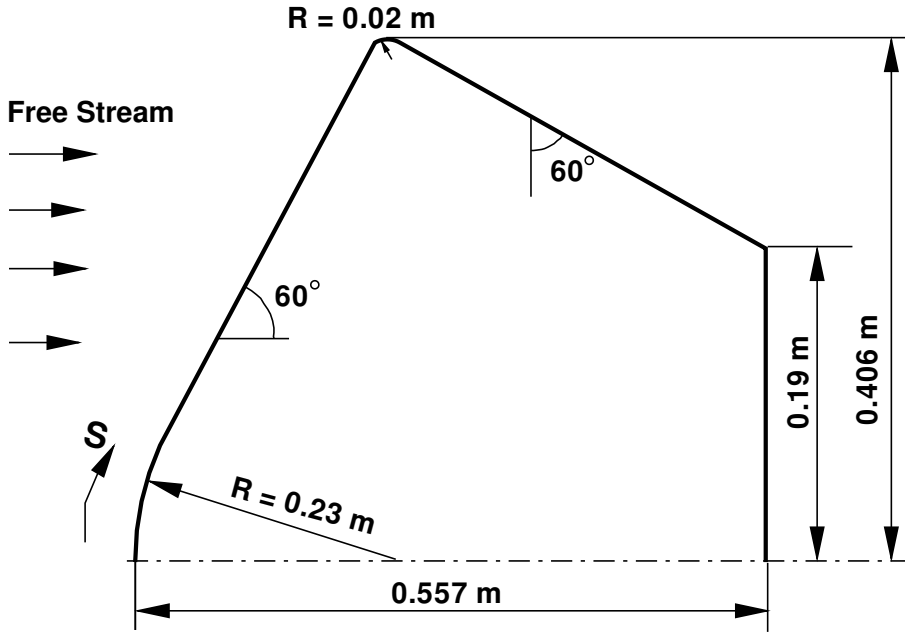

Figure 5.19: Stardust configuration [3]. Note that S represents the distance along the surface starting from the forebody stagnation point and R refers to the radius.

Velocity	12.391 kms^{-1}
Mach number	41.87
Temperature	217.60
Number density	2.6388×10^{20}
N_2 mole fraction	76.23%
O_2 mole fraction	23.77%
Kn	1.28×10^{-2}

Table 5.17: Free-stream conditions experienced by the Stardust at 81 km [3]. The mole fraction of O_2 is increased to 23.77% from 23.72%, the latter percentage is presented by Zhong *et al.* and is thought to be a typographical error.

Figures 5.20 and 5.21 shows the wall temperature and heat transfer comparisons, respectively of the results obtained from Zhong *et al.* and *dsmcFoam* using

DSMC code / Parameter	Zhong *et al.*	*dsmcFoam*
Time-step [s]	1×10^{-7}	1×10^{-7}
Total particles	5.4×10^{6}	6.6×10^{6}
F_{num}	2×10^{12}	8×10^{13}
Sampled time-steps	80000	500000

Table 5.18: DSMC simulation parameters for the Stardust re-entry at 81 km.

the DWTM. Both comparisons are in very good agreement. Although there is scatter apparent in the *dsmcFoam* results, sampling the properties for a longer time will reduce this noise. The total CPU time consumed by *dsmcFoam* was 3192 hours. And although the total number of sampling time-steps was greater for *dsmcFoam* than required by Zhong *et al.* as shown in table 5.18, decreasing the number of real molecules each DSMC particle represents in the *dsmcFoam* calculations would have ensured a more converged solution after a lower number of time-steps in the sampling stage.

5.4 Summary

This chapter has conveyed the importance of wall temperature definitions and although setting an isothermal wall temperature may be applied to benchmark test cases, in real engineering applications this may have a significant impact to the flow phenomena and surface properties, especially during the re-entry stage of spacecraft. The hypersonic cylinder test case, in section 5.2.1, had shown that by setting different isothermal temperature definitions between 500 and 2000 K the results were heavily dependent upon them. Major differences such as surface heat transfer and shock stand-off distances were noticed. Although in much simpler systems, such as the hypersonic blunt-body outlined in section 5.2.2, minor differences were noticed between the surface properties. However, as the

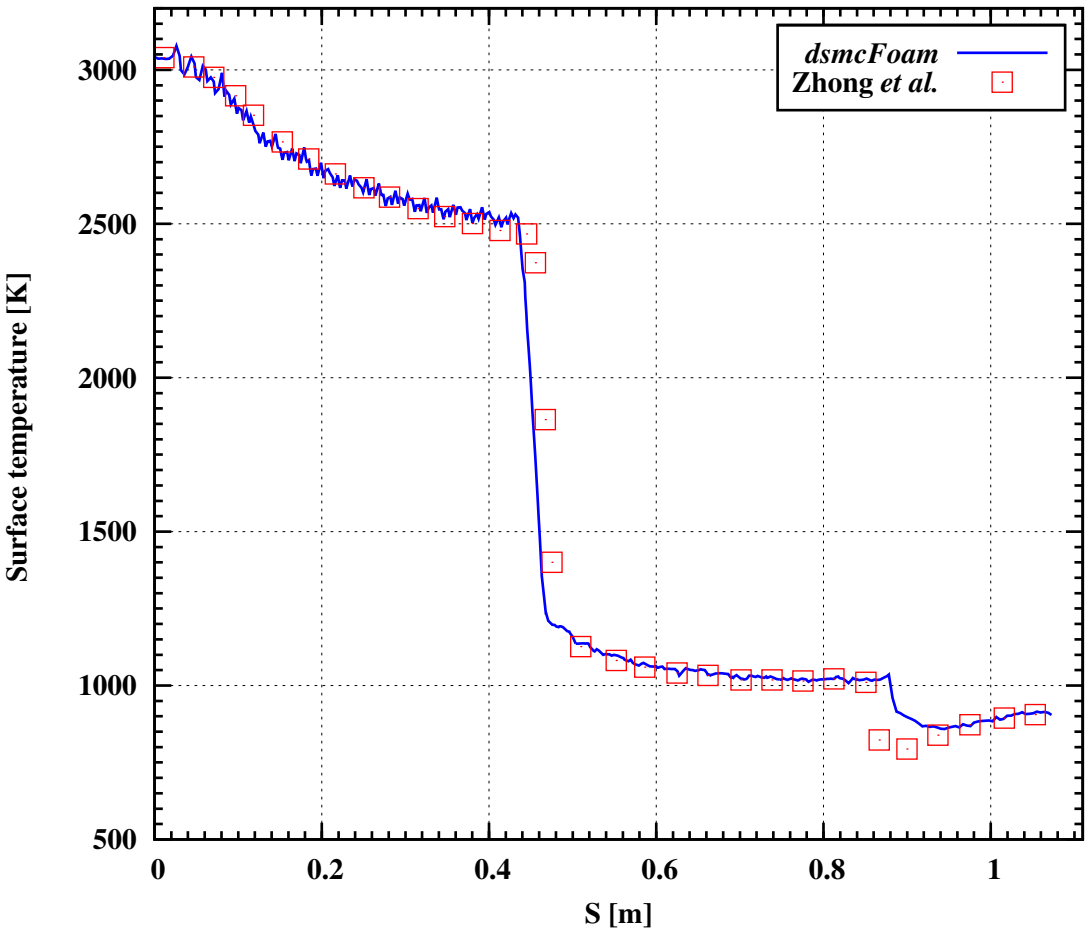

Figure 5.20: Stardust surface temperature distributions calculated by Zhong *et al.* and *dsmcFoam* using the DWTM.

velocity of the blunt-body decreased the temperature of the wall became more important on the properties.

Furthermore, a wall temperature model was implemented in *dsmcFoam* to define the wall temperature based on equation 5.4, by negating the conduction term it was reduced to equation 5.7 and therefore was used to verify the radiative part due to convection against free-molecular theory. The free-molecular theory was used to derive two analytical solutions, AS1 and AS2, and excellent agreement was found between these and *dsmcFoam* at high free-stream velocities. It also helped show that at low free-stream velocities the thermal energy becomes more

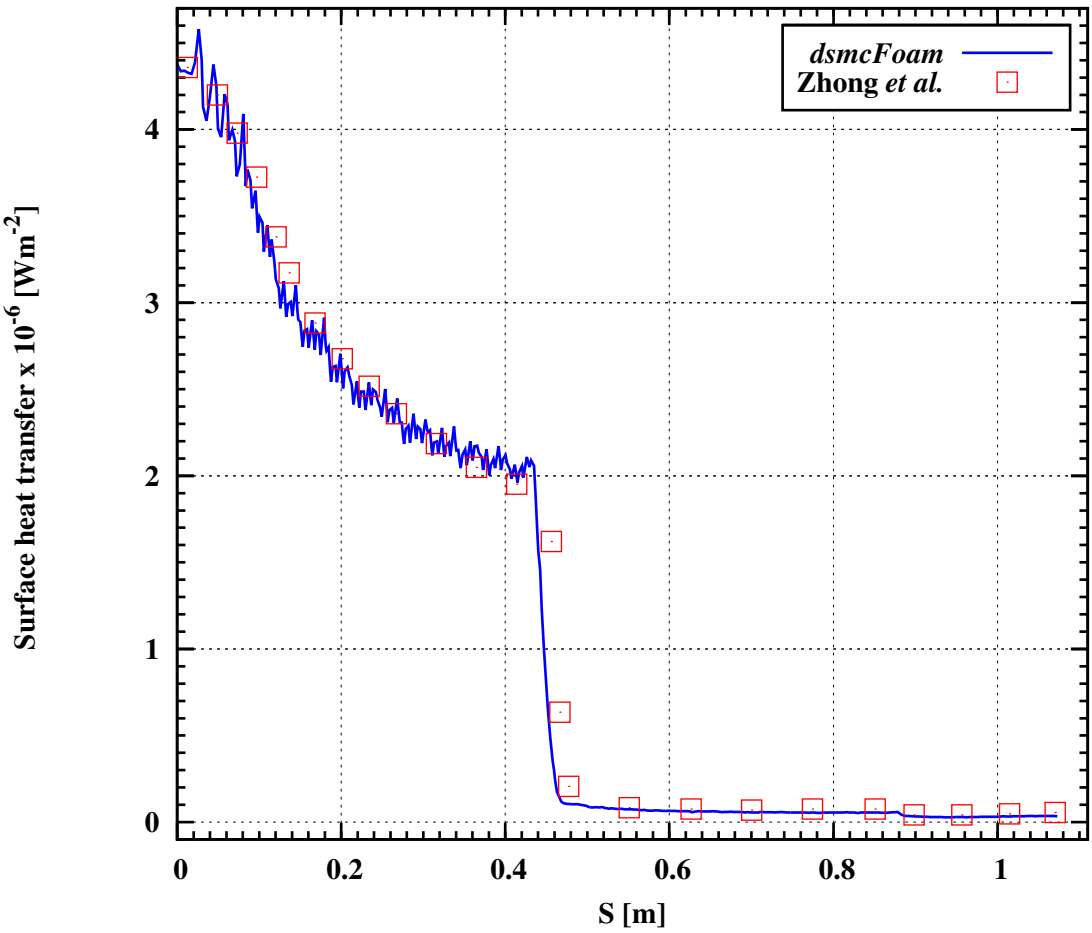

Figure 5.21: Stardust surface heat transfer distributions calculated by Zhong *et al.* and *dsmcFoam* using the DWTM.

significant in comparison to the kinetic energy and the thermal component is not accounted for in AS1. In addition, small differences between AS2 and *dsmcFoam* were apparent at the lower velocities but these will be resolved as part of a future study by extending the free-stream boundaries as investigated for some of the velocities in section 5.3.4.

Finally, the DWTM of *dsmcFoam* was validated with Stardust aerothermodynamics determined by Zhong *et al.*. Very good agreement was observed for both surface temperature and heat transfer.

Chapter 6

Conclusions and future work

6.1 Conclusions

The open source DSMC code, called *dsmcFoam*, has been recently written within the framework of the open source computational fluid dynamics (CFD) toolbox OpenFOAM [45] using the underlying principles of the open source molecular dynamics solver created by Macpherson [46]. This thesis focussed on the benchmarking of *dsmcFoam* and outlined techniques introduced by the author in *dsmcFoam* to improve the efficiency and accuracy of simulations. The results of the benchmark investigations were compared with analytical solutions, other DSMC codes and experimental data available in the literature and excellent agreement was found when good DSMC practice was adopted.

Furthermore, this thesis presented an introduction to the DSMC method and briefly discussed some of the established DSMC codes in the literature and outlined the main features of *dsmcFoam*. In addition, parallel efficiency studies were presented of *dsmcFoam* and they were carried out on high performance computers at the University of Strathclyde and Argonne National Laboratory (U.S.) [11]. Up to two-billion DSMC particles and 1536 processors were used in these studies

and *dsmcFoam* was found to be a very efficient solver. A new domain decomposition method for parallel *dsmcFoam* simulations was also presented and it was compared against the standard OpenFOAM *Scotch* and *Simple* decomposition techniques using the 0° angle-of-attack planetary probe case. The new decomposition technique reduced the computational time by at least 28% in comparison to the standard techniques.

The main advances of *dsmcFoam* discussed in this thesis were a routine for selecting collision pairs called the transient adaptive sub-cell (TASC) method and a dynamic wall temperature model (DWTM) that relates the wall temperature to the heat flux. In addition, verification and validation studies were undertaken of the DWTM with free-molecular theory and the Stardust aerothermodynamics [3], respectively and very good agreement was found.

The widely used conventional 8 sub-cell method used to select possible collision pairs has been shown to be relatively cumbersome to employ properly as a lot of mesh refinement stages are required in order to obtain accurate data. Instead of mesh refinement the TASC technique automatically employs more sub-cells, and these sub-cells are based on the number of particles in a cell. The TASC method is an extension to the 8 sub-cell method for the purpose of selecting collision partners in close proximity to each other. The standard TASC method has been shown to be a reliable tool in predicting accurate properties of systems that have a large cell size. The size of the cells in this case were approximately two mean free paths long, this is very large in comparison to the recommended size of one third of the mean free path. In the same graph and as expected the results using the conventional 8 sub-cell method did not agree well with Bird's results as good DSMC practice was not followed. The TASC method was then improved for sub-cells that contain only one particle. In this scenario, the standard TASC method looks for a collision partner in the entire cell, whereas the improved TASC

algorithm looks for a collision partner in close proximity or adjacent sub-cells.

Finally, the author has investigated the aerothermodynamics over re-usable single-stage to orbit space-planes, called Skylon and CFASTT-1. The latter space-plane has been developed by the author and others from the research group called *Centre for Future Air-Space Transportation Technology* at the University of Strathclyde. Due to the length requirements the Skylon and CFASTT-1 investigations have not been considered in this thesis, however for more information on those studies the reader is referred to References [7–9].

6.2 Future work

The work presented in this theses will be carried forward and briefly explained in this section.

Firstly the parallel efficiency studies were presented of *dsmcFoam* in this theses. These studies were carried out on high performance computers at the University of Strathclyde and Argonne National Laboratory (U.S.) [11]. Up to two-billion DSMC particles and 1536 processors were used. In future work the number of particles will be increased and tested at the limits of processing capability at the Argonne National Laboratory (U.S.) [11]. The computing capability at Argonne National Laboratory is chosen for these studies because it is one of the most advanced computing power in the world.

A new domain decomposition method for parallel *dsmcFoam* simulations was presented in this theses and large savings in computational power was noticed. This new decomposition method for *dsmcFoam* was based on splitting the computational domain up in to sections such that all sections contained the same number of particles. And each section would then be processed by a computer processor. This work will be carried forward to accommodate for the mesh cells

of the computational domain. Therefore, there will be a weighting factor between the number of particles and mesh cells for each processor to deal with. This weighting factor will be investigated for even more savings in computational power.

Finally, the transient adaptive sub-cells and the dynamic wall temperature model will be used on large scale simulations such as investigating the aerothermodynamics of re-usable single-stage to orbit space-planes, mentioned in the previous section, at many different Knudsen numbers.

References

[1] J. N. Moss, C. E. Glass, and F. A. Greene. DSMC simulations of Apollo capsule aerodynamics for hypersonic rarefied conditions. *Proceedings of the ninth AIAA/ ASM thermophysics and heat transfer conference, San Francisco, U.S.A.*, AIAA Paper 2006-3577, 2006.

[2] G. A. Bird. Sophisticated DSMC. *Short course at the DSMC07 meeting, Santa Fe, U.S.A.*, 2007.

[3] J. Zhong, T. Ozawa, and D. A. Levin. Modeling of Stardust reentry ablation flows in the near-continuum flight regime. *AIAA Journal*, 46(10):2568–2581, 2008.

[4] G. A. Bird. *Molecular gas dynamics and the direct simulation of gas flows*. Oxford University Press Inc., New York, 1998.

[5] C. C. Su, K. C. Tseng, H. M. Cave, J. S. Wu, Y. Y. Lian, T. C. Kuo, and M. C. Jermy. Implementation of a transient adaptive sub-cell module for the parallel-DSMC code using unstructured grids. *Computers & Fluids*, 39(7):1136–1145, 2010.

[6] R. Coppinger. EU to fund hypersonic civil transport research. *Flightglobal, www.flightglobal.com/news/articles/eu-to-fund-hypersonic-civil-transport-research-218658*, 2007.

[7] A. O. Ahmad, T. J. Scanlon, and R. E. Brown. Aerodynamic environment of

the Skylon configuration under rarefied flow conditions. *Technical report to the German aerospace center (DLR) and Reaction Engines*, 2010.

[8] A. O. Ahmad, C. Maddock, T. J. Scanlon, and R. E. Brown. Prediction of the aerodynamic performance of re-usable single-stage to orbit vehicles. *Proceedings of the first international space access conference, Paris, France*, 2011.

[9] R. Wuilbercq, A. O. Ahmad, T. J. Scanlon, and R. E. Brown. Towards robust aero-thermodynamic predictions for re-usable single-stage to orbit vehicles. *Proceedings of the eighteenth AIAA/ 3AF international space planes and hypersonic systems and technologies conference, Tours, France*, AIAA Paper 2012-5803, 2012.

[10] P. Marks. Hypersonic instability may have doomed Beagle 2. *New Scientist*, 200 (2687), 2008.

[11] A. O. Ahmad and S. Aithal. Comparison of *dsmcFoam* efficiency on ARCHIE-WeSt at the University of Strathclyde and the high performance computer at the Argonne National Laboratory (U.S.A.). *Private communication*, 2012.

[12] F. Sharipov. Rarefied gas dynamics and its applications to vacuum technology. *Proceedings of CERN Accelerator School "Vacuum in Acceleratrs", Platja dAro, Spain*, 2006.

[13] W. D. Niven, editor. *Scientific papers of James Clerk Maxwell*. Dover Publications Inc., New York, 1965.

[14] L. Boltzmann. Weitere studien über das wärmegleichgewicht unter gasmolekülen. *Sitzung Berichte Kaiserl. Akad. der Wissenschaften*, 66:275–370, 1872.

[15] M. Knudsen. Die molekularströmung der gase durch offnungen und die effusion. *Annalen der Physik*, 333:999–1016, 1909.

[16] D. Enskog. Bermerkungen zu einer fundamentalgleichung in der kinetischen gastheorie. *Physikalische Zeitschrift*, 12:533–539, 1911.

[17] D. Hilbert. Grundüge einer allgemein theorie der linearen integralgleichungen. *Teubner, Leipzig*, 1912.

[18] S. Chapman. On the law of distribution of molecular velocities, and on the theory of viscosity and thermal conduction, in a non-uniform simple monatomic gas. *Philosophical Transactions of the Royal Society of London*, 216:279–348, 1916.

[19] P. L. Bhatnagar, E. P. Gross, and M. Krook. A model for collision processes in gases. I. Small amplitude processes in charged and neutral one-component systems. *Physical Review*, 94:511–525, 1954.

[20] P. Welander. On the temperature jump in a rarefied gas. *Arkiv Fysik*, 7:507–553, 1954.

[21] A. Krönig. Grundzüge einer theorie der gase. *Annalen der Physik*, 175:315–322, 1856.

[22] R. Clausius. Ueber die art der bewegung, welche wir wärme nennen. *Annalen der Physik*, 176:353–380, 1857.

[23] B. Mahon. *The man who changed everything: the life of James Clerk Maxwell*. John Wiley & Sons, 2004.

[24] T. Wilholt. When realism made a difference: The constitution of matter and its conceptual enigmas in late 19th century physics. *Studies in History and Philosophy of Science Part B: Studies in History and Philosophy of Modern Physics*, 39 (1):1–16, 2008.

[25] A. Einstein. Über die von der molekularkinetischen theorie der wärme geforderte bewegung von in ruhenden flüssigkeiten suspendierten teilchen. *Annalen der Physik*, 322:549–560, 1905.

[26] M. Smoluchowski. Zur kinetischen theorie der Brownschen molekularbewegung und der suspensionen. *Annalen der Physik*, 326:756–780, 1906.

[27] M. D. Haw. Colloidal suspensions, Brownian motion, molecular reality: a short history. *Journal of Physics: Condensed Matter*, 14(33):7769–7779, 2002.

[28] C. Bigg. *A visual history of Jean Perrins Brownian motion curves, in histories of scientific observation.* The University of Chicago Press, Ltd., London, 2011.

[29] C. Cercignani. *Mathematical methods in kinetic theory.* Plenum Publishing Inc., New York, 1990.

[30] A. L. Garcia. *Numerical methods for physics.* Prentice-Hall Inc, New Jersey, 2000.

[31] S. Luding. On the relevance of "molecular chaos" for granular flows. *ZAMM - Journal of Applied Mathematics and Mechanics/ Zeitschrift fr Angewandte Mathematik und Mechanik*, 80(S1):9–12, 2000.

[32] N. Dongari, Y. Zhang, and J. M. Reese. Molecular dynamics simulations of high speed rarefied gas flows. *Proceedings of the twenty-eighth international symposium on rarefied gas dynamics, Zaragoza, Spain*, 2012.

[33] W. D. Nicholls, M. K. Borg, D. A. Lockerby, and J. M. Reese. Water transport through (7,7) carbon nanotubes of different lengths using molecular dynamics. *Microfluidics and Nanofluidics*, 12(1-4):257–264, 2012.

[34] J. M. Reese and W. D. Nicholls. Perspectives on the simulation of micro gas and nano liquid flows. *Proceedings of the ninth ASME international conference on nanochannels, microchannels and minichannels, Edmonton, Canada*, 2011.

[35] W. G. Vincenti and C. H. Kruger. *Introduction to physical gas dynamics*. John Wiley, New York, 1965.

[36] I. D. Boyd, G. Chen, and G. V. Candler. Predicting failure of the continuum fluid equations in transitional hypersonic flows. *Physics of Fluids*, 7(210), 1995.

[37] M. Gad-el-Hak. The fluid mechanics of microdevices - the Freeman Scholar lecture. *Journal of fluids engineering*, 121:5–33, 1999.

[38] C. Greenshields and J. M. Reese. Rarefied high-speed flow simulations using both particle and continuum-fluid methods in OpenFOAM. *Presentation*, 2010.

[39] A. J. Lofthouse. *Nonequilibrium hypersonic aerothermodynamics using the direct simulation Monte Carlo and Navier-Stokes models, Ph.D. Thesis*. University of Michigan, U.S.A., 2008.

[40] M. Smoluchowski. Ueber wärmeleitung in verdünnten gasen. *Annalen der Physik*, 300:101–130, 1898.

[41] J. C. Maxwell. On stresses in rarefied gases arising from inequalities of temperature. *Proceedings of the Royal Society of London*, 27:304–308, 1878.

[42] H. Grad. On the kinetic theory of rarefied gases. *Communications on Pure and Applied Mathematics*, 2(4):331–407, 1949.

[43] P. Taheri, M. Torrilhon, and H. Struchtrup. Couette and Poiseuille microflows: Analytical solutions for regularized 13-moment equations. *Physics of Fluids*, 21, 017102, 2009.

[44] W. Wagner. A convergence proof for Birds direct simulation Monte Carlo method for the Boltzmann equation. *Journal of Statistical Physics*, 66(3-4):1011–1044, 1992.

[45] OpenFOAM. The open source CFD toolbox, user guide, version 1.6. *www.openfoam.com*, 2009.

[46] G. B. Macpherson. *Molecular dynamics simulation in arbitrary geometries for nanoscale fluid mechanics, Ph.D. Thesis.* University of Strathclyde, U.K., 2008.

[47] G. J. LeBeau, K. A. Jacikas, and F. E. Lumpkin. Virtual sub-cells for the direct simulation Monte Carlo method. *Proceedings of the forty-first AIAA aerospace sciences meeting and exhibit, Reno, U.S.A.*, AIAA Paper 2003-1031, 2003.

[48] J. S. Wu, K. C. Tseng, and F. Y. Wu. Parallel three-dimensional DSMC method using mesh refinement and variable time-step scheme. *Computer Physics Communications*, 162(3):166–187, 2004.

[49] C. C. Su, K. C. Tseng, J. S. Wu, H. M. Cave, M. C. Jermy, and Y. Y. Lian. Two-level virtual mesh refinement algorithm in a parallelized DSMC code using unstructured grids. *Computers & Fluids*, 48(1):113–124, 2011.

[50] D. F. G. Rault. Aerodynamics of the Shuttle Orbiter at high altitudes. *Journal of Spacecraft and Rockets*, 31(6):944–952, 1994.

[51] M. S. Ivanov, G. N Markelov, S. F. Gimelshein, L. V. Mishina, A. N Krylov, and N. V. Grechko. High-altitude capsule aerodynamics with real gas effects. *Journal of Spacecraft and Rockets*, 35(1):16–22, 1998.

[52] J. N. Moss. Direct simulation Monte Carlo simulations of ballute aerothermodynamics under hypersonic rarefied conditions. *Journal of Spacecraft and Rockets*, 44(2):289–298, 2007.

[53] J. N. Moss, C. E. Glass, B. R. Hollis, and J. W. Van Norman. Low-density aerodynamics for the inflatable reentry vehicle experiment. *Journal of Spacecraft and Rockets*, 43(6):1191–1201, 2006.

[54] G. A. Dahlen, M. N. Macrossan, C. L. Brundin, and J. K. Harvey. Blunt cones in rarefied hypersonic flow: Experiments and Monte-Carlo simulations. *Proceedings*

of the fourteenth International Symposium on Rarefied Gas Dynamics, Tskuba, Japan, 1:229–240, 1984.

[55] I. D. Boyd. Modeling of associative ionization reactions in hypersonic rarefied flows. *Physics of Fluids*, 19(9), 2007.

[56] R. C. Blanchard, R. G Wilmoth, and J. N. Moss. Aerodynamic flight measurements and rarefied-flow simulations of Mars entry vehicles. *Journal of Spacecraft and Rockets*, 34(5):687–690, 1997.

[57] J. N. Moss, R. C. Blanchard, R. G Wilmoth, and R. D. Braun. Mars Pathfinder rarefied aerodynamics: Computations and measurements. *Journal of Spacecraft and Rockets*, 36(3):330–339, 1999.

[58] R. Bur, R. Benay, B. Chanetz, A. Galli, T. Pot, B. Hollis, and J. Moss. Experimental and numerical study of the mars pathfinder vehicle. *Aerospace Science and Technology*, 7(7):510–516, 2003.

[59] D. F. G. Rault. Aerodynamic characteristics of the Magellan spacecraft in the Venus upper atmosphere. *Journal of Spacecraft and Rockets*, 31(4):537–542, 1994.

[60] C. Cai, I. D. Boyd, J. Fan, and G. V. Candler. Direct simulation methods for low-speed microchannel flows. *Journal of Thermophysics and Heat Transfer*, 14 (3):368–378, 2000.

[61] H. Xue, Q. Fan, and C. Shu. Prediction of micro-channel flows using direct simulation Monte Carlo. *Probabilistic Engineering Mechanics*, 15(2):213–219, 2000.

[62] W. W. Liou and Y. Fang. Heat transfer in microchannel devices using DSMC. *Journal of Microelectromechanical Systems*, 10(2):274–279, 2001.

[63] W. W. Liou and Y. Fang. *Microfluid mechanics: Principles and modeling*. McGraw-Hill, New York, 2005.

[64] C. White, M. K. Borg, T. J. Scanlon, and J. M. Reese. A DSMC investigation of gas flows in micro-channels with bends. *Computers & Fluids*, 71:261–271, 2013.

[65] G. A. Bird. Approach to translational equilibrium in a rigid sphere gas. *Physics of Fluids*, 6(10):1518–1519, 1963.

[66] G. A. Bird. Definition of mean free path for real gases. *Physics of Fluids*, 26(11): 3222–3223, 1983.

[67] G. A. Bird. Shock wave structure in a rigid sphere gas. *Proceedings of the fourth international symposium on rarefied gas dynamics, Toronto, Canada*, 1964.

[68] G. A. Bird. The velocity distribution function within a shock wave. *Journal of Fluid Mechanics*, 30(3):479–487, 1967.

[69] G. A. Bird. The structure of normal shock waves in a binary gas mixture. *Journal of Fluid Mechanics*, 31(4):657–668, 1968.

[70] G. A. Bird. Breakdown of translational and rotational equilibrium in gaseous expansions. *AIAA Journal*, 8(11):1998–2003, 1970.

[71] C. Borgnakke and P. S. Larsen. Statistical collision model for Monte Carlo simulation of polyatomic gas mixture. *Journal of Computational Physics*, 18(4): 405–420, 1975.

[72] G. A. Bird. Recent advances and current challenges for DSMC. *Computers & Mathematics with Applications*, 35(1-2):1–14, 1998.

[73] G. A. Bird. A comparison of collision energy-based and temperature-based procedures in DSMC. *Proceedings of the twenty-sixth international symposium on rarefied gas dynamics, Kyoto, Japan*, 2008.

[74] A. L. Garcia. Direct simulation Monte Carlo: Theory, methods, and open challenges. *Proceedings of the Models and Computational Methods for Rarefied Flows*, 2011.

[75] S. K. Stefanov. On DSMC calculations of rarefied gas flows with small number of particles in cells. *SIAM Journal on Scientific Computing*, 33(2):677–702, 2011.

[76] M. S. Ivanov and S. V Rogasinsky. Analysis of numerical techniques of the direct simulation Monte Carlo method in the rarefied gas dynamics. *Russian Journal of Numerical Analysis and Mathematical Modelling*, 3(6):453–465, 1988.

[77] G. A. Bird. Perception of numerical methods in rarefied gas dynamics. *Proceedings of the sixteenth international symposium on rarefied gas dynamics, Pasadena, U.S.A.*, 1988.

[78] A. Venkattraman, A. A. Alexeenko, M. A. Gallis, and M. S. Ivanov. A comparative study of no-time-counter and majorant collision frequency numerical schemes in DSMC. *Proceedings of the twenty-eighth international symposium on rarefied gas dynamics, Zaragoza, Spain*, 2012.

[79] E. Roohi. *Private communication*, 2013.

[80] I. D. Boyd. Direct simulation Monte Carlo for atmospheric entry. 1: Theoretical basis and physical models. *Notes for VKI shortcourse, nonequilibrium gas dynamics: From physical models to hypersonic flights*, 2008.

[81] J. Balakrishnan, I. D. Boyd, and D. G. Braun. Monte Carlo simulation of vapor transport in physical vapor deposition of Titanium. *Journal of Vacuum Science & Technology A*, 18(3):907–916, 2000.

[82] F. Bergemann and I. D. Boyd. New discrete vibrational energy method for the direct simulation Monte Carlo method. *Rarefied Gas Dynamics, Progress in Astronautics and Aeronautics, AIAA, Washington, U.S.A.*, 158:174–180, 1994.

[83] G. Zuppardi, L. Morsa, and F. Romano. Influence of chemical models on the computation of thermo-fluid-dynamic parameters in hypersonic, rarefied flows. *Pro-*

ceedings of the Institution of Mechanical Engineers, Part G: Journal of Aerospace Engineering, 224(6):637–646, 2009.

[84] R. C. Millikan and D. R. White. Systematics of vibrational relaxation. *Journal of Chemical Physics*, 39(12):3209–3213, 1963.

[85] G. A. Bird. Chemical reactions in DSMC. *Proceedings of the twenty-seventh international symposium on rarefied gas dynamics, Pacific Grove, U.S.A.*, 2010.

[86] G. A. Bird. The Q-K model for gas-phase chemical reaction rates. *Physics of Fluids*, 23(10), 2011.

[87] A. A. Alexeenko, S. F. Gimelshein, E. P. Muntz, and A. D. Ketsdever. Kinetic modeling of temperature driven flows in short microchannels. *International Journal of Thermal Sciences*, 45(11):1045–1051, 2006.

[88] DSMC Resources from Graeme Bird. *www.gab.com.au*, 2013.

[89] M. S. Ivanov, A. V. Kashkovsky, S. F. Gimelshein, G. N Markelov, A. A. Alexeenko, Y. A. Bondar, G. A. Zhukova, S. B. Nikiforov, and P. V. Vashenkov. SMILE system for 2D/3D DSMC computations. *Proceedings of the twenty-fifth international symposium on rarefied gas dynamics, St. Petersburg, Russia*, 2006.

[90] T. Bányai, E. Torres, T. E. Magin, A. V. Kashkovsky, P. V. Vashchenkov, M. S. Ivanov, and P. Rambaud. Evaluation of the aerodynamic properties of the Intermediate eXperimental Vehicle in the rarefied and transitional regime. *Proceedings of the fourth European conference for aerospace sciences, St. Petersburg, Russia*, 2011.

[91] S. Dietrich and I. D Boyd. Scalar and parallel optimized implementation of the direct simulation Monte Carlo method. *Journal of Computational Physics*, 126 (2):328–342, 1996.

[92] I. D. Boyd. Direct simulation Monte Carlo for atmospheric entry. 2: Code development and application results. *Notes for VKI shortcourse, nonequilibrium gas dynamics: From physical models to hypersonic flights*, 2008.

[93] MONACO. *www.ngpdlab.engin.umich.edu*, 2013.

[94] T. J. Scanlon, E. Roohi, C. White, M. Darbandi, and J. M. Reese. An open source, parallel DSMC code for rarefied gas flows in arbitrary geometries. *Computers & Fluids*, 39(10):2078–2089, 2010.

[95] Gambit. *www.ansys.com*, 2013.

[96] T. J. Scanlon, C. White, M. Schuebler, R. E. Brown, and J. M. Reese. Thermochemistry modelling in an open source DSMC code. *Proceedings of the twenty-eighth international symposium on shock waves, Manchester, U.K.*, 2011.

[97] ARCHIE-WeSt, high performance computer for the West of Scotland and based at the University of Strathclyde in Glasgow. *www.archie-west.ac.uk*, 2013.

[98] Comparison of Intel Xeon X5650 processor and Intel Xeon X5550 Nehalem processor. *www.cpu-world.com/Compare/852/Intel_Xeon_X5550_vs_Intel_Xeon_X5650*, 2013.

[99] G. A. Bird. *Visual DSMC program for three-dimensional flows. The DS3V program user's guide.* Version 1.2, March 2005.

[100] A. O. Ahmad, T. J. Scanlon, and J. M. Reese. Capturing shock waves using an open-source, direct simulation Monte Carlo (DSMC) code. *Proceedings of the fourth European conference for aerospace sciences, St. Petersburg, Russia*, 2011.

[101] K. Sutton. Air radiation revisited. *Proceedings of the nineteenth AIAA thermophysics conference, Snowmass, U.S.A.*, AIAA Paper 84-1733, 1984.

[102] M. S. Holden, T. P. Wadhams, G. V. Candler, and J. K. Harvey. Measurements in regions of low density laminar shock wave/ boundary layer interaction in hypervelocity flows and comparison with Navier-Stokes predictions. *Proceedings of the forty-first AIAA aerospace sciences meeting and exhibit, Reno, U.S.A.*, AIAA Paper 2003-1131, 2003.

[103] J. N. Moss, G. A. Bird, and G. N. Markelov. DSMC simulations of hypersonic flows and comparison with experiments. *AIP Conference Proceedings*, 762:547–552, 2004.

[104] J. Allègre, D. Bisch, and J. C. Lengrand. Experimental rarefied density flowfields at hypersonic conditions over 70-degree blunted cone. *Journal of Spacecraft and Rockets*, 34(6):714–718, 1997.

[105] J. Allègre, D. Bisch, and J. C. Lengrand. Experimental rarefied heat transfer at hypersonic conditions over 70-degree blunted cone. *Journal of Spacecraft and Rockets*, 34(6):724–728, 1997.

[106] J. Allègre, D. Bisch, and J. C. Lengrand. Experimental rarefied aerodynamic forces at hypersonic conditions over 70-degree blunted cone. *Journal of Spacecraft and Rockets*, 34(6):719–723, 1997.

[107] B. D. Stewart and F. E. Lumpkin. Axisymmetric plume simulations with NASA's DSMC analysis code. *Proceedings of the thirty-third exhanst plume and signatures (EPSS), Monterey, U.S.A.*, 2012.

[108] M. N. Macrossan. Searching for DSMC collision partners using pseudo-subcells. *DSMC09 meeting, U.S.A.*, 2009.

[109] M. A. Gallis, J. R Torczynski, D. J. Rader, and G. A. Bird. Accuracy and convergence of a new DSMC algorithm. *Proceedings of the fortieth AIAA thermophysics conference, Seattle, U.S.A.*, AIAA Paper 2008-3913, 2008.

[110] J. S. Wu, K. C. Tseng, U. M. Lee, and Y. Y. Lian. Development of a general parallel threedimensional direct simulation Monte Carlo code. *Proceedings of the twenty-fourth international symposium on rarefied gas dynamics, Bari, Italy*, 2004.

[111] A. J. Lofthouse, I. D. Boyd, and M. J. Wright. Effects of continuum breakdown on hypersonic aerothermodynamics. *Proceedings of the forty-fourth AIAA aerospace sciences meeting and exhibit, Reno, U.S.A.*, AIAA Paper 2006-993, 2006.

[112] H. M. Cave. *Development of modelling techniques for pulsed pressure chemical vapour deposition (PP-CVD), Ph.D. Thesis.* University of Canterbury, New Zealand, 2008.

[113] P. V. Vashchenkov and M. S. Ivanov. Numerical Analysis of high-altitude aerothermodynamics of EXPERT reentry vehicle. *International conference on the methods of aerophysical research, Russia*, 2002.

[114] P. A. C. Sampaio and W. F. N. Santos. Computational analysis of the aerodynamic heating and drag of a reentry Brazilian satellite. *Proceedings of the sixth national congress of mechanical engineering, Campina Grande, Brazil*, 2010.

[115] J. F. Padilla. *Assessment of gas-surface interaction models for compuation of rarefied hypersonic flows, Ph.D. Thesis.* University of Michigan, U.S.A., 2008.

[116] B. L. Haas. Models for dynamic surface temperatures during rarefied aeropass maneuvers. *Proceedings of the twenty-eighth AIAA thermophysics conference, Orlando, U.S.A.*, AIAA Paper 93-2765, 1993.

[117] U.S. standard atmosphere. *National oceanic and atmospheric administration. National aeronautics and space administration. United States Air Force.*, 1976.

[118] M. A. Covington, J. M. Heinemann, H. E. Goldstein, Y. K. Chen, I. Terrazas-Salinas, J. A. Balboni, J. Olejniczak, and E. R. Martinez. Performance of a low

density ablative heat shield material. *Journal of Spacecraft and Rockets*, 45(2): 237–247, 2008.

[119] J. D. Anderson. *Hypersonic and high-temperature gas dynamics, second edition.* American Institute of Aeronautics and Astronautics Inc., Virginia, 2006.

[120] M. S. Ivanov, G. N Markelov, and S. F. Gimelshein. Statistical simulation of reactive rarefied flows: Numerical approach and applications. *Proceedings of the seventh AIAA/ ASME joint thermophysics and heat transfer conference, Albuquerque, U.S.A.*, AIAA Paper 1998-2669, 1998.

[121] T. Ozawa, J. Zhong, and D. A. Levin. Development of kinetic-based energy exchange models for noncontinuum, ionized hypersonic flows. *Physics of Fluids*, 20, 046102, 2008.

[122] I. D. Boyd. *Private communication*, 2012.

Appendix A

Benchmarking *dsmcFoam* with an analytical solution and DSMC3

This appendix presents comparisons of *dsmcFoam* collision rates with an analytical solution of Bird [4]. Also in this appendix, *dsmcFoam* has been used to model the supersonic flow across two flat plates joined together which form a corner. The results are then compared against Bird's data [4] that was produced using the DSMC3 program - a three-dimensional DSMC program developed by Bird.

A.1 Verification of *dsmcFoam* collision rates

It is important to investigate the implementation of the collision sampling routine to determine if the DSMC code returns the correct collision rates. Predicting accurate collision rates is vital to any DSMC simulation, and the most common technique used is the no-time-counter (NTC) method as discussed in chapter 2.

This section verifies the NTC method, used in *dsmcFoam*, against an analyt-

ical solution. The test case considered for this investigation is a simple three-dimensional adiabatic box containing only one cell at an equilibrium state with no gradients of density, temperature and velocity. The volume of the test case is 1×10^{-9} m^3 and contains one million DSMC particles. Three setups are considered as outlined in table A.1 and their corresponding molecular properties are in table A.2. For each setup, a different wall temperature is used as outlined in table A.3. The collision rates are averaged over ten thousand time-steps and the time-step for each setup is fixed to 1×10^{-6} s.

Test case	n_{Ar}	n_{N_2}
A	1×10^{20}	0
B	0	1×10^{20}
C	0.5×10^{20}	0.5×10^{20}

Table A.1: Number densities of each test case used in determining the collision rates.

Parameter	Argon	Nitrogen
ω	0.81	0.74
d [m]	4.17×10^{-10}	4.17×10^{-10}
m [kg]	66.3×10^{-27}	46.5×10^{-27}

Table A.2: Variable hard sphere molecular properties, at a reference temperature of 273K, used in determining the collision rates. ω, d and m is the viscosity index, molecular diameter and mass, respectively.

Temperature [K]		
100	200	300
400	500	600
700	800	900
1000	2000	3500
5000	7500	10000

Table A.3: Gas temperatures used in each test case for determining the collision rates.

The number of collisions determined by *dsmcFoam* are modified to form the

number of collisions per unit time per unit volume (N_{CTV}) as

$$N_{CTV} = \frac{N_{RMDP} N_{coll}}{t_s V}, \tag{A.1}$$

where N_{RMDP} is the number of real molecules that one DSMC particle represents and N_{coll} is the number of collisions. t_s is the time-step and V is the volume. Equation A.1 is compared against the analytical solution, derived by [4] for the number of collisions per unit time per unit volume between molecules p and q in an equilibrium state,

$$((N_{CTV})_{pq})_{es} = 2\pi^{\frac{1}{2}} (d_{ref})_{pq}^2 n_p n_q \left\{ \frac{T}{(T_{ref})_{pq}} \right\}^{1-\omega_{pq}} \left\{ \frac{2k (T_{ref})_{pq}}{m_r} \right\}^{\frac{1}{2}}. \tag{A.2}$$

Where p and q represent different species and the subscript es indicates an equilibrium state. The macroscopic gas conditions, n and T represent the number density and temperature, respectively. Variable hard sphere parameters: d_{ref}, T_{ref} and ω represent the reference molecular diameter, reference temperature and the viscosity index, respectively. m_r is reduced mass and k is the Boltzmann constant. Note that equation A.2 counts all collision twice as it determines the number of collisions between p and q, and q and p. Therefore, it is necessary to add a symmetry factor of a half in order to recover the correct collision rate for a gas with only one species. In the case of two species, the total number of collisions per unit time per unit volume is,

$$((N_{CTV})_{pq,pp,qq})_{es} = ((N_{CTV})_{pq})_{es} + ((N_{CTV})_{pp})_{es} + ((N_{CTV})_{qq})_{es}. \tag{A.3}$$

The first term, $((N_{CTV})_{pq})_{es}$, from the right hand side of equation A.3 is calculated

using equation A.2 and the remaining second and third terms are calculated as,

$$((N_{CTV})_{pp})_{es} = \pi^{\frac{1}{2}} (d_{ref})_{pp}^{2} n_p^2 \left\{ \frac{T}{(T_{ref})_{pp}} \right\}^{1-\omega_{pp}} \left\{ \frac{2k (T_{ref})_{pp}}{m_r} \right\}^{\frac{1}{2}} \tag{A.4}$$

and

$$((N_{CTV})_{qq})_{es} = \pi^{\frac{1}{2}} (d_{ref})_{qq}^{2} n_q^2 \left\{ \frac{T}{(T_{ref})_{qq}} \right\}^{1-\omega_{qq}} \left\{ \frac{2k (T_{ref})_{qq}}{m_r} \right\}^{\frac{1}{2}}, \tag{A.5}$$

respectively.

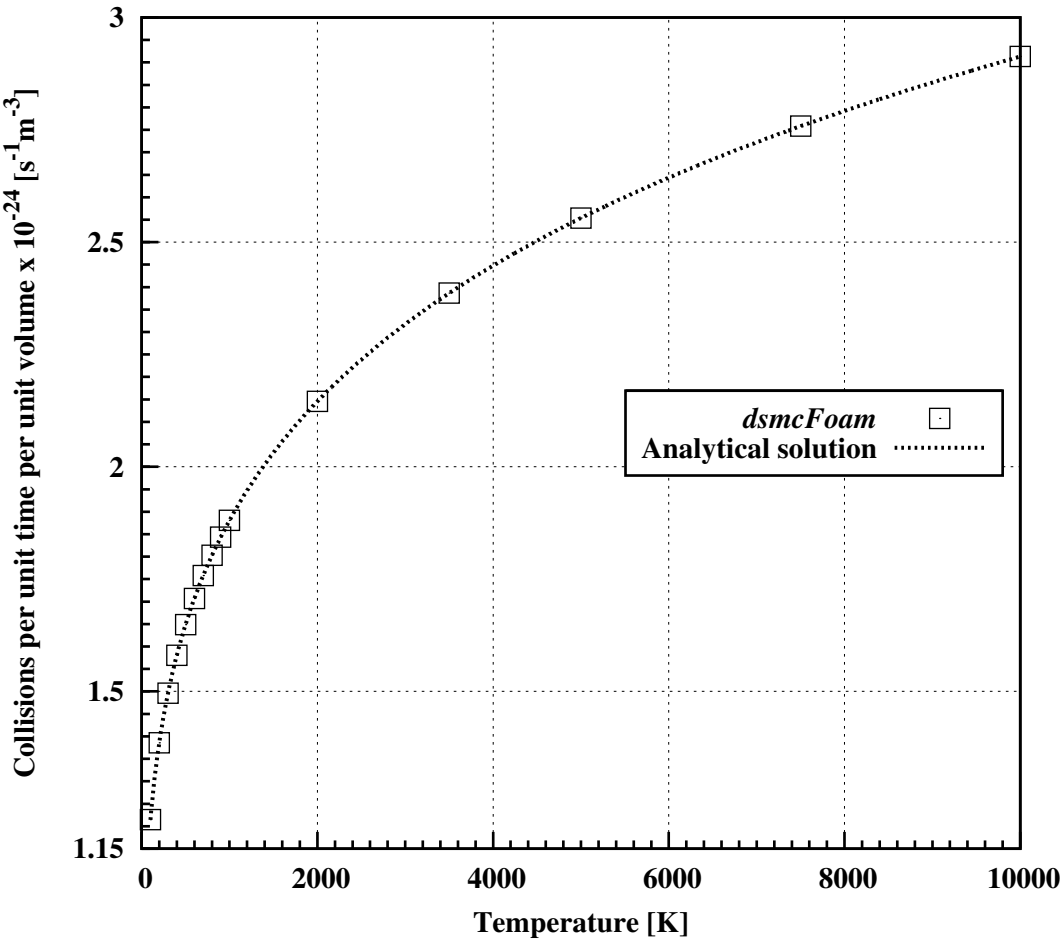

Figure A.1: Comparisons of the number of collisions per unit time per unit volume between *dsmcFoam* and the analytical solution of test case A at the temperatures in table A.3. The analytical solution is based on equation A.2 with a symmetry factor of a half.

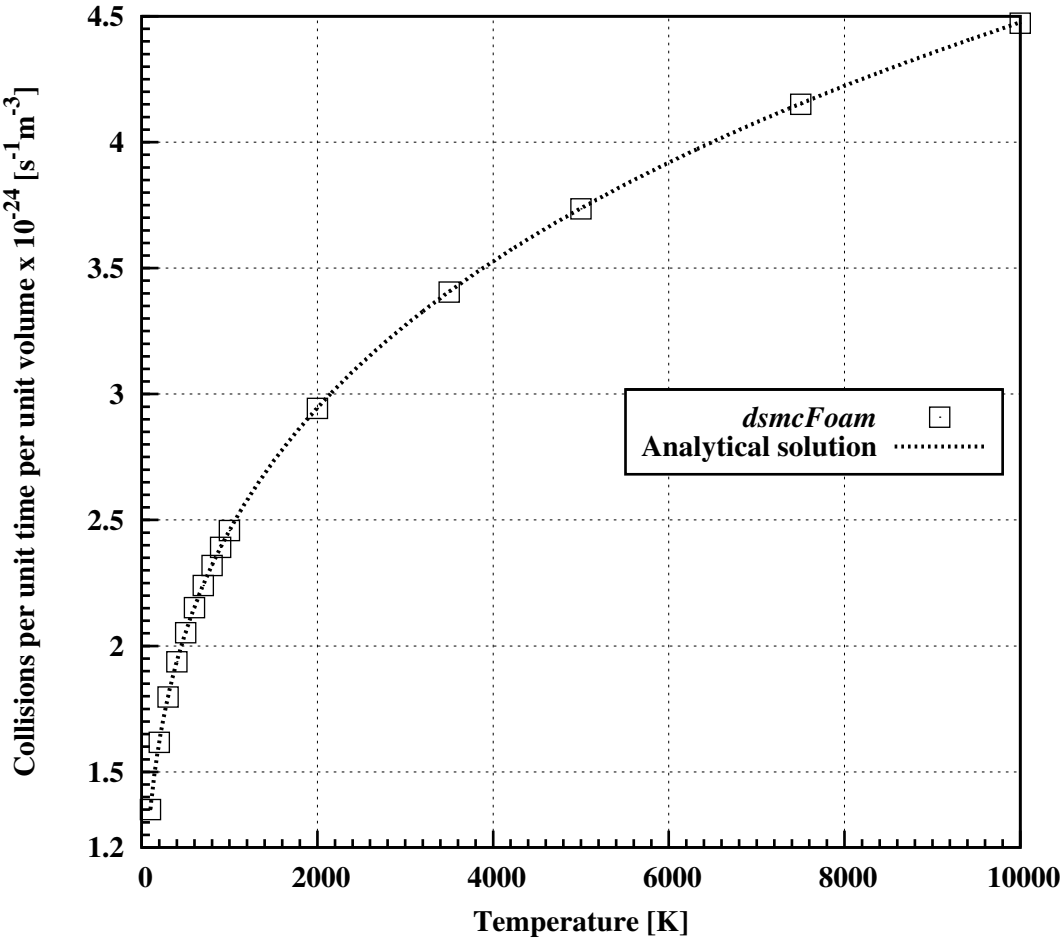

Figure A.2: Comparisons of the number of collisions per unit time per unit volume between *dsmcFoam* and the analytical solution of test case B at the temperatures in table A.3. The analytical solution is based on equation A.2 with a symmetry factor of a half.

Figures A.1, A.2 and A.3 show the comparisons between *dsmcFoam* and the appropriate analytical solutions of test case A, B and C, respectively. The comparisons are in excellent agreement and the percentage differences of test case A, B and C with the analytical solutions are illustrated in tables A.4, A.5 and A.6, respectively. The percentage difference is calculated as,

$$Difference\,(\%) = \left(\frac{dsmcFoam\ rate}{analytical\ rate} - 1\right) \times 100, \tag{A.6}$$

where the *dsmcFoam* rate represents the number of collisions per unit time per

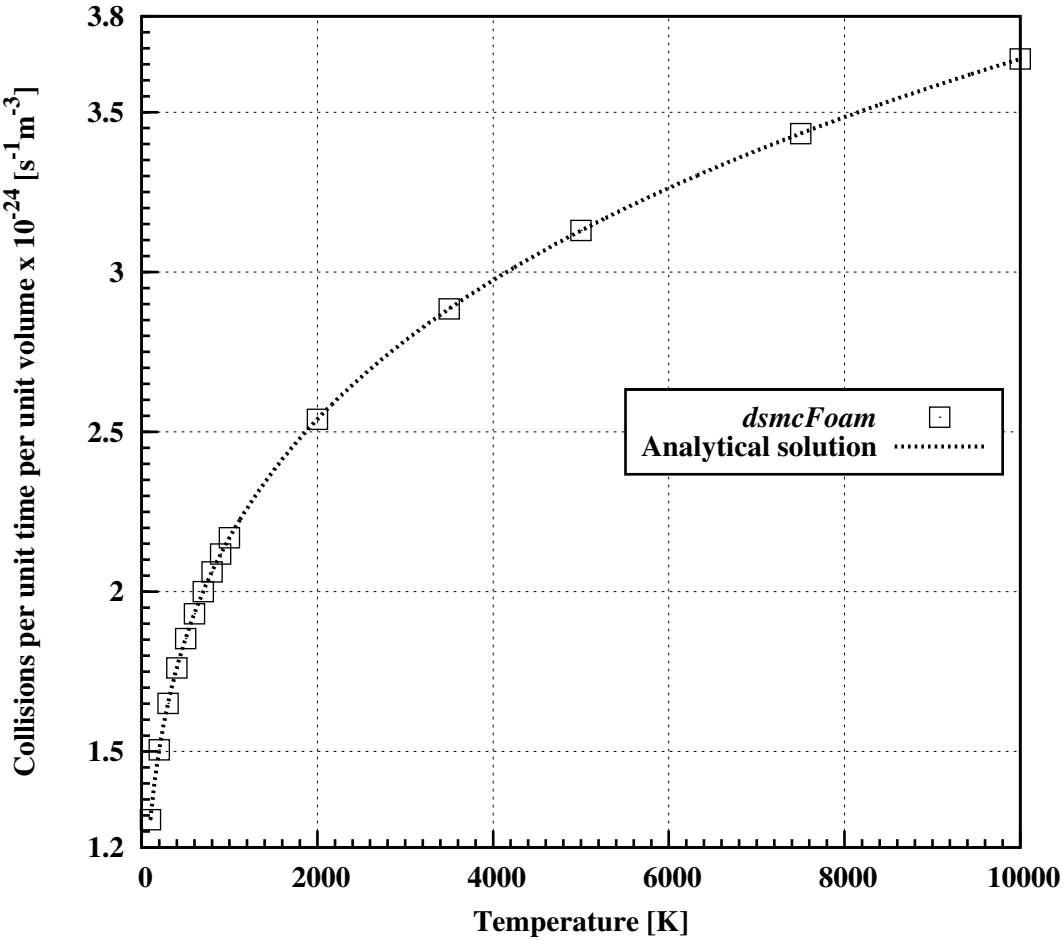

Figure A.3: Comparisons of the number of collisions per unit time per unit volume between *dsmcFoam* and the analytical solution of test case C at the temperatures in table A.3. The analytical solution is based on equation A.3.

unit volume of the simulation. The maximum difference of all three test cases is 0.06989% thus validating the *dsmcFoam* collision rates..

A.2 Supersonic gas flow over a corner

In this section, gas flow over a supersonic corner is investigated using *dsmcFoam*. The results from *dsmcFoam* are compared against Bird's results [4] at a body-length global Knudsen number of 0.0534 - based on the variable hard sphere mean free path and length (l) of the plate. The supersonic corner is constructed by two

Temperature [K]	Difference (%)
100	0.00795
200	0.00549
300	0.00088
400	0.00616
500	0.01118
600	0.00485
700	0.00716
800	0.00554
900	0.00585
1000	0.00533
2000	0.00691
3500	0.00397
5000	0.00243
7500	0.00438
10000	0.00855

Table A.4: Percentage differences between *dsmcFoam* and the analytical solution of test case A at the temperatures in table A.3. The analytical solution is based on equation A.2 with a symmetry factor of a half and the percentage differences are absolute values.

flat plates, perpendicular to each other as shown in figure A.4. The computational grid consists of 30×18×18 cells, where 30 cells are present in the x-direction, and each cell has dimensions of 0.01×0.01×0.01 m and contains no sub-cells. Also the leading edge of the two plates is five cells from the free-stream boundary, in the x-direction. The two flat plates are considered as fully diffuse at a temperature of 1000 K. The free-stream conditions consist of a Mach 6 Argon gas flow parallel to the x-axis with a temperature of 300 K and number density of 1×10^{20} m^{-3}. The simulation run-time was eighteen hours on a single processor and the results were sampled over 3×10^5 time-steps for a total number of particles of approximately 1.2×10^5. Contours of pressure coefficient (C_p), determined by *dsmcFoam* and Bird [4], on the surface of the flat plates are compared in figure A.5. The pressure

Temperature [K]	Difference (%)
100	0.06346
200	0.06920
300	0.06232
400	0.06295
500	0.06342
600	0.05967
700	0.06989
800	0.06316
900	0.06203
1000	0.06318
2000	0.06382
3500	0.06075
5000	0.06519
7500	0.06334
10000	0.06333

Table A.5: Percentage differences between *dsmcFoam* and the analytical solution of test case B at the temperatures in table A.3. The analytical solution is based on equation A.2 with a symmetry factor of a half and the percentage differences are absolute values.

coefficient is calculated as,

$$C_p = \frac{p - p_\infty}{\frac{1}{2}\rho_\infty U_\infty^2}, \tag{A.7}$$

where p is the surface pressure, and p_∞, ρ_∞ and U_∞ is the free-stream pressure, density and velocity, respectively. In theory, the contours should be matching on both plates as the flow is symmetrical with reference to an imaginary plane bisecting the angle between the two plates, and this is noticed in the figure. Furthermore, the contours of pressure coefficient determined by the two codes are in excellent agreement.

Contours of heat transfer coefficient (C_h), determined by *dsmcFoam* and Bird [4], on the surface of the flat plates are compared in figure A.6. The heat

Temperature [K]	Difference (%)
100	0.00319
200	0.01249
300	0.00530
400	0.00018
500	0.00689
600	0.00095
700	0.00152
800	0.00635
900	0.00222
1000	0.00095
2000	0.00301
3500	0.00511
5000	0.00274
7500	0.00325
10000	0.00024

Table A.6: Percentage differences between *dsmcFoam* and the analytical solution of test case C at the temperatures in table A.3. The analytical solution is based on equation A.3 and the percentage differences are absolute values.

transfer coefficient is calculated as,

$$C_h = \frac{q}{\frac{1}{2}\rho_\infty U_\infty^3}, \tag{A.8}$$

where q is the surface heat transfer. The contours of heat transfer coefficient determined by the two codes are in excellent agreement. Also, the figure shows the supersonic corner is subject to large heat transfers close to the leading edge and intersection of the plates. However, close to the leading edge the heat transfer reduces as the distance from the plate's intersection increases and behaves in an opposite fashion to this close to the trailing edge. Furthermore, the heat transfer reduces considerably at the trailing edge to less than 15% of the maximum heat transfer at the plate's intersection.

Contours of stream-wise (x-direction) skin friction coefficient ($(C_f)_x$), deter-

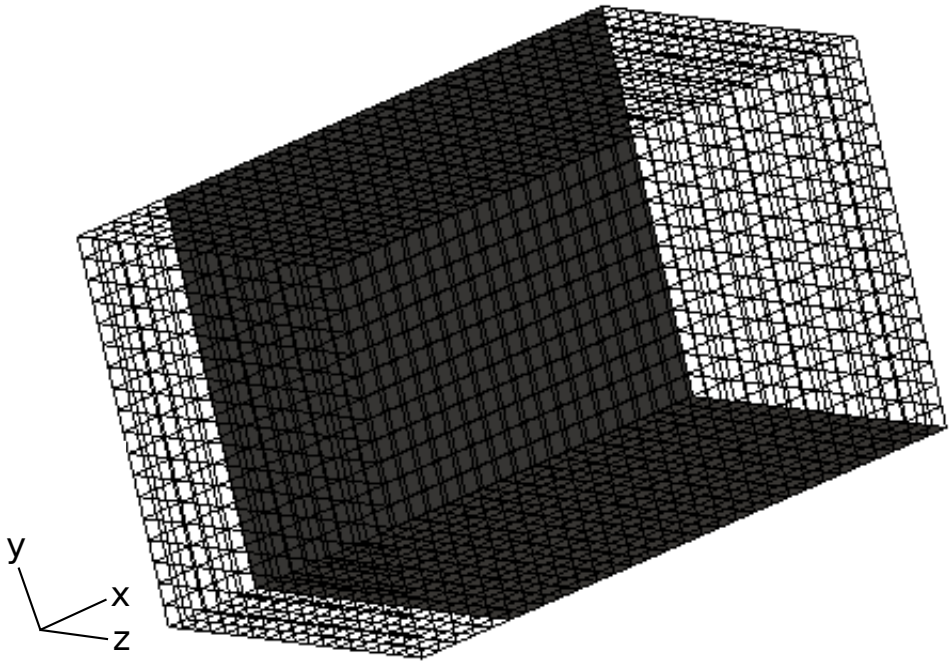

Figure A.4: The supersonic corner configuration. The gridlines represent the mesh.

mined by *dsmcFoam* and Bird [4], on the surface of the flat plates are compared in figure A.7. The stream-wise skin friction coefficient is calculated as,

$$(C_f)_x = \frac{\tau_x}{\frac{1}{2}\rho_\infty U_\infty^2}, \tag{A.9}$$

where τ_x is the shear stress in the stream-wise direction. The contours of surface friction coefficient determined by the two codes are in excellent agreement.

The previous results focused on surface properties over the two plates, figures A.8 and A.9 illustrate the contours of normalised temperature and normalised density, respectively, throughout the field. These figures are presented as slices from the supersonic corner's cuboid domain for both *dsmcFoam* and Bird [4]. The results between the two codes are in excellent agreement.

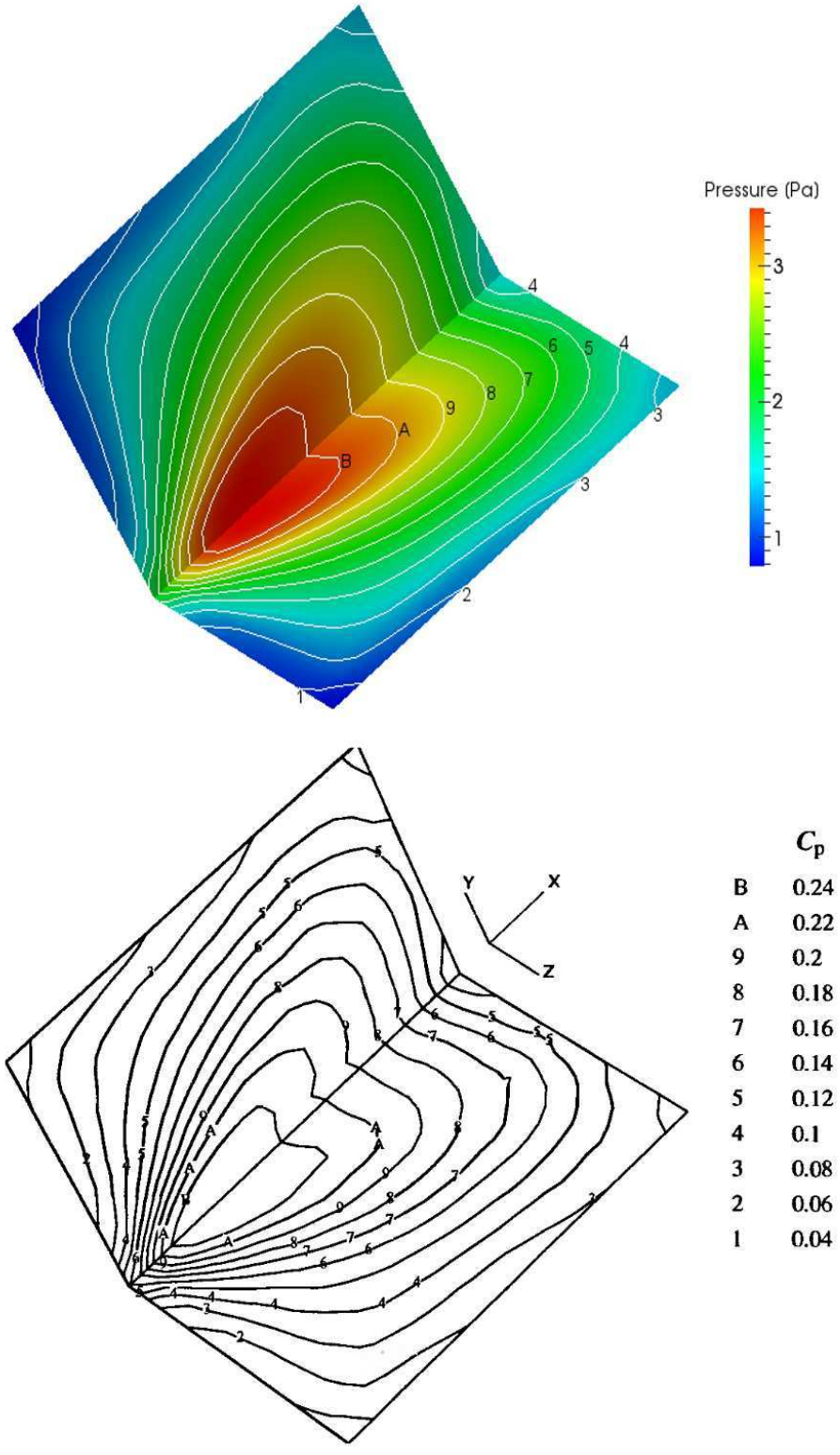

Figure A.5: Contours of pressure coefficient, determined by *dsmcFoam* (top) and Bird [4] (bottom), on the surface of the flat plates. The C_p key (bottom) is for the contours obtained from both codes and the pressure [Pa] key (top) is for the colour contours produced by *dsmcFoam*.

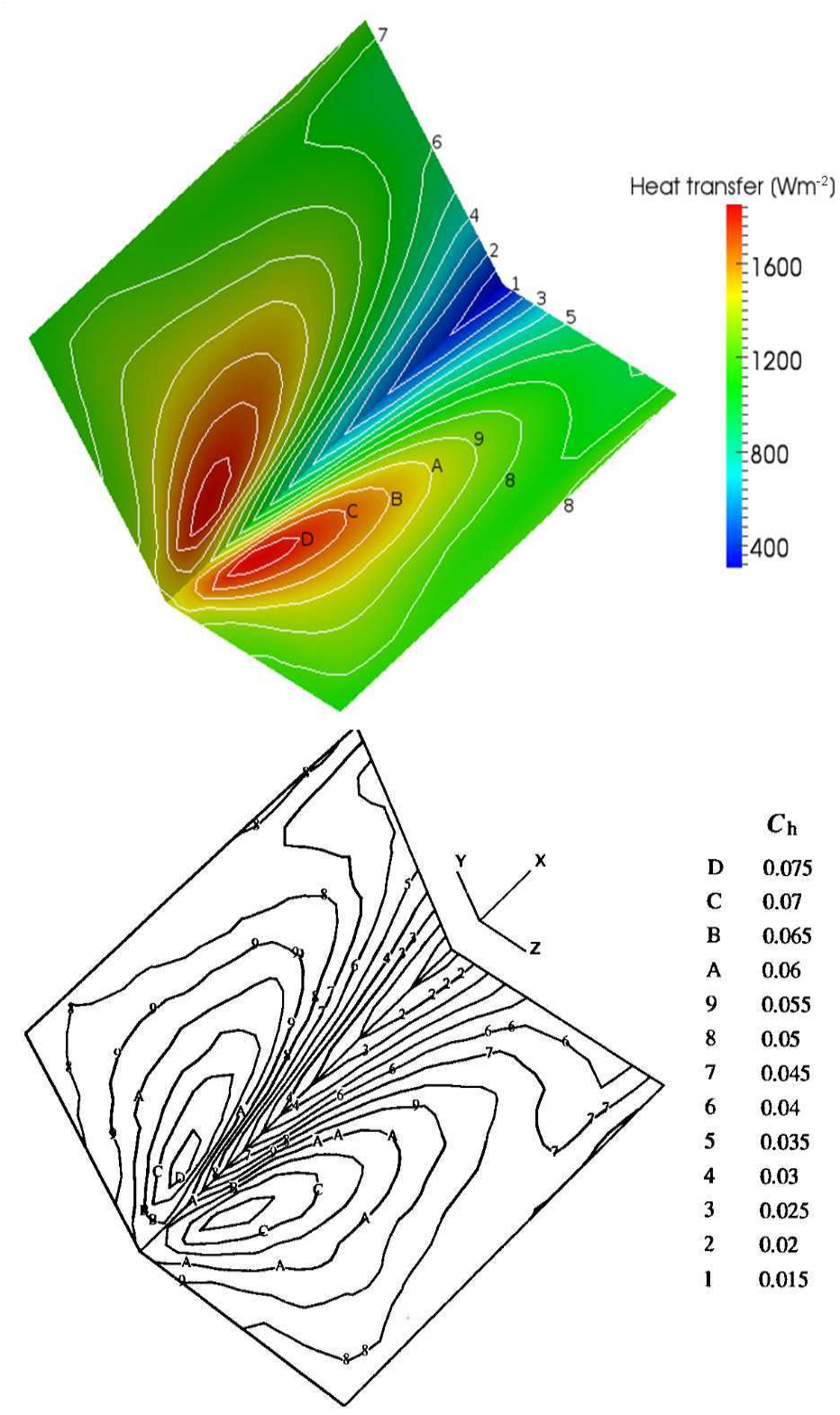

Figure A.6: Contours of heat transfer coefficient, determined by *dsmcFoam* (top) and Bird [4] (bottom), on the surface of the flat plates. The C_h key (bottom) is for the contours obtained from both codes and the heat transfer [Wm^{-2}] key (top) is for the colour contours produced by *dsmcFoam*.

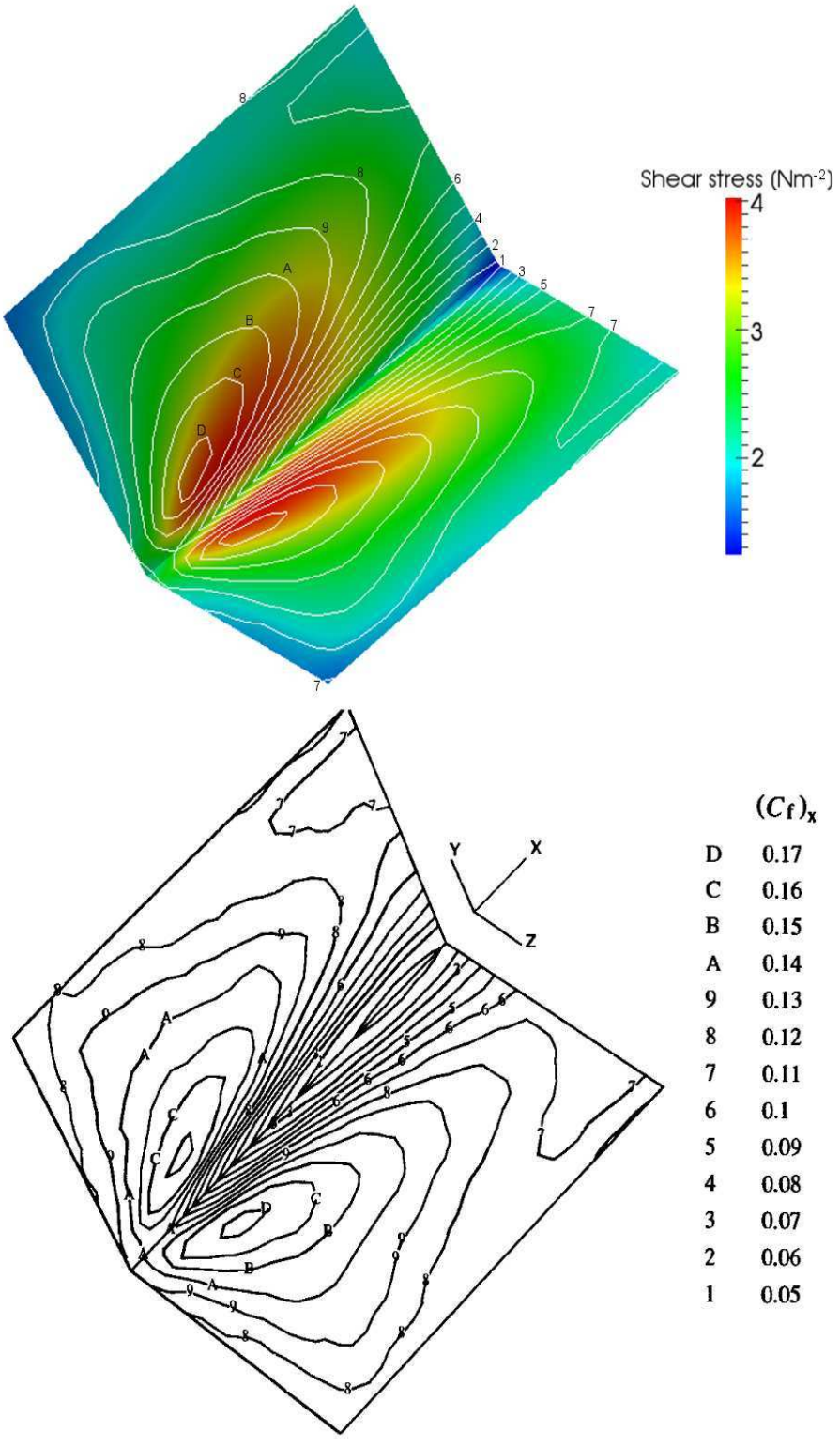

Figure A.7: Contours of stream-wise skin friction coefficient, determined by *dsmcFoam* (top) and Bird [4] (bottom), on the surface of the flat plates. The $(C_f)_x$ key (bottom) is for the contours obtained from both codes and the shear stress [Nm^{-2}] key (top) is for the colour contours produced by *dsmcFoam*.

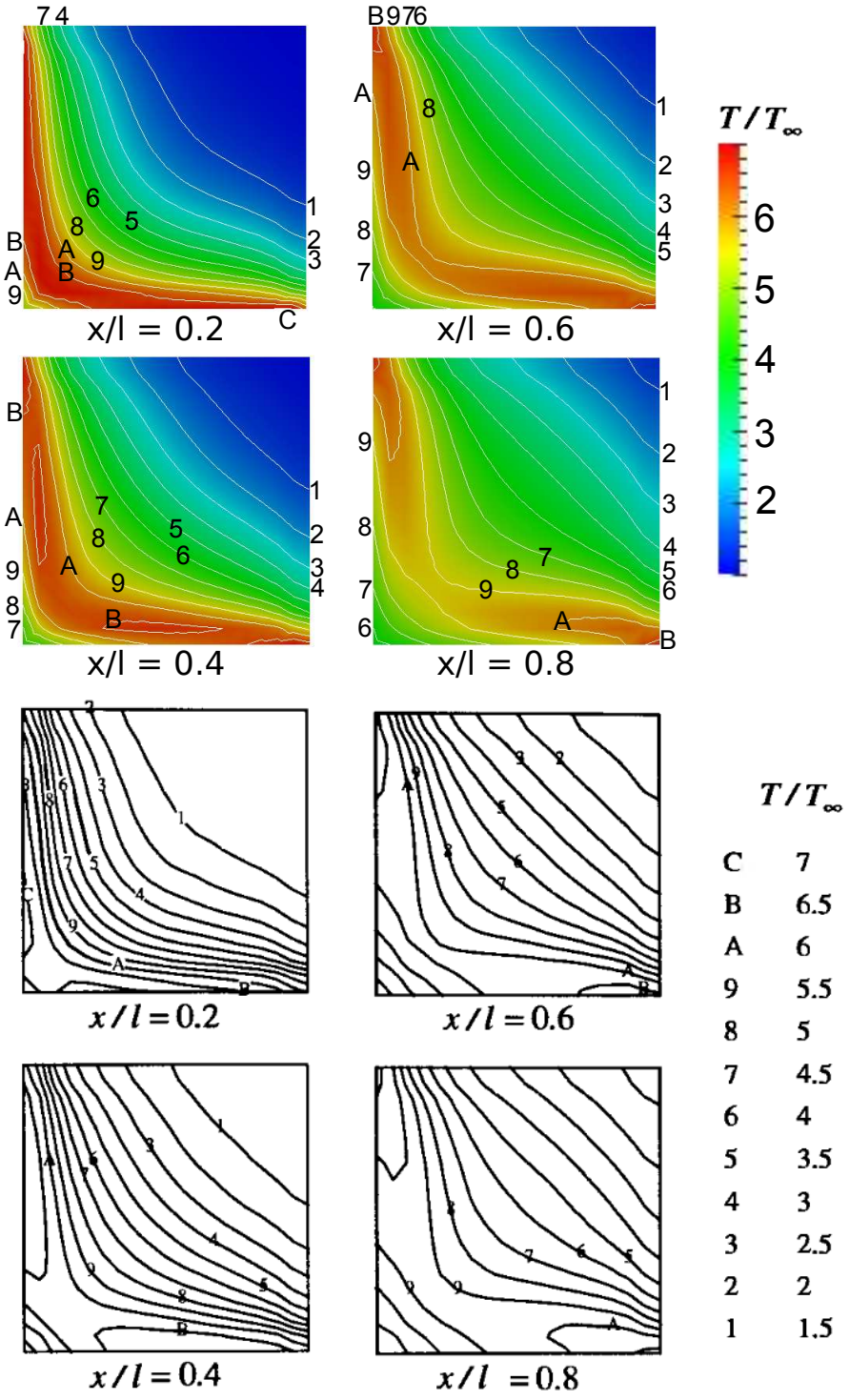

Figure A.8: Contours of non-dimensional temperature, determined by *dsmcFoam* (top) and Bird [4] (bottom), in planes normal to the plates. The bottom key is for the contours obtained from both codes and the top key is for the colour contours produced by *dsmcFoam*.

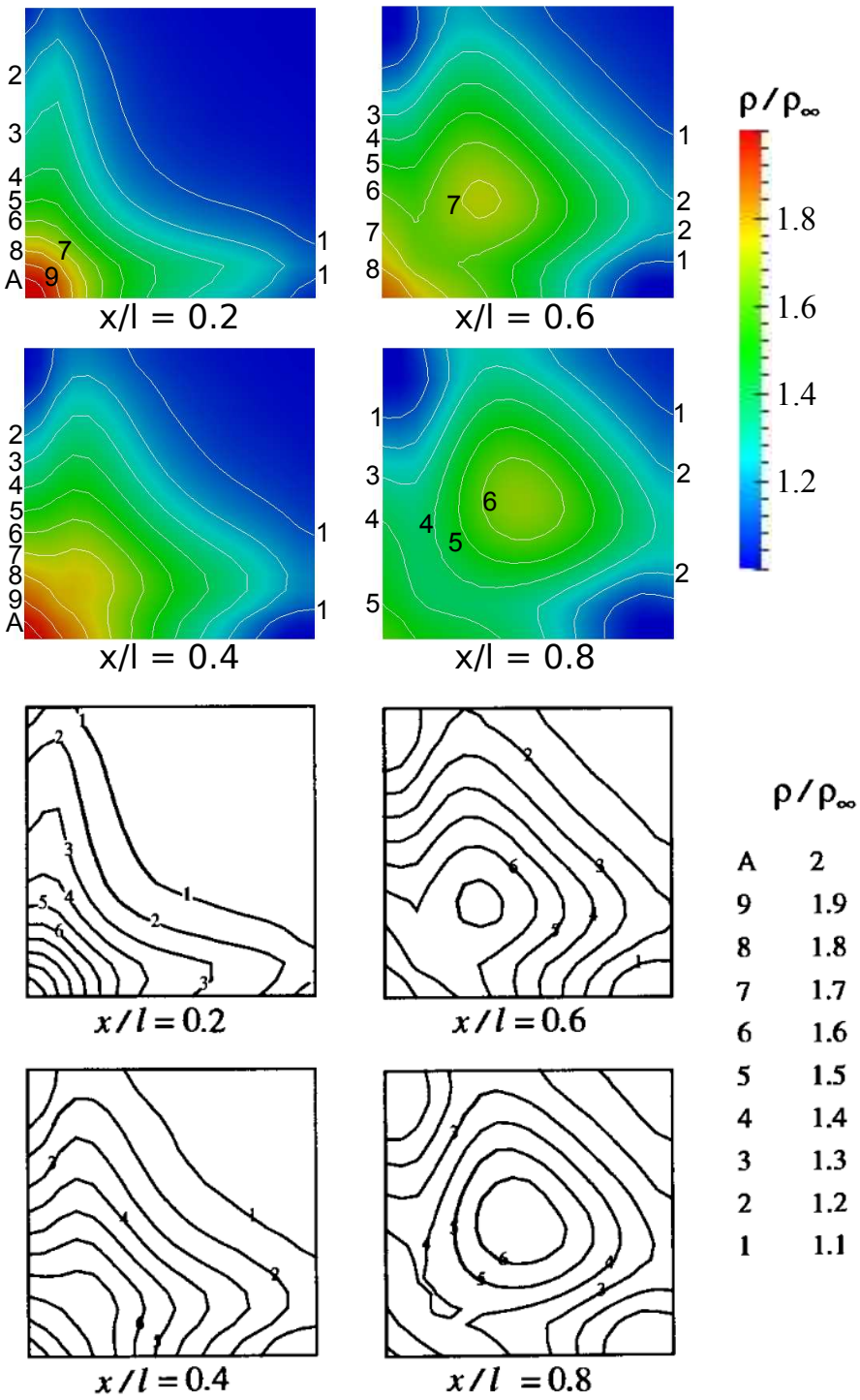

Figure A.9: Contours of non-dimensional density, determined by *dsmcFoam* (top) and Bird [4] (bottom), in planes normal to the plates. The bottom key is for the contours obtained from both codes and the top key is for the colour contours produced by *dsmcFoam*.

Appendix B

Free-molecular theory

Analytical solutions from free-molecular theory [122], discussed in this Appendix, are used to verify the dynamic wall temperature model of *dsmcFoam* in section 5.3.3. The analytical solutions are derived from equilibrium kinetic theory and they are commonly used to investigate spacecraft aerothermodynamics in free molecular, collisionless gas dynamics.

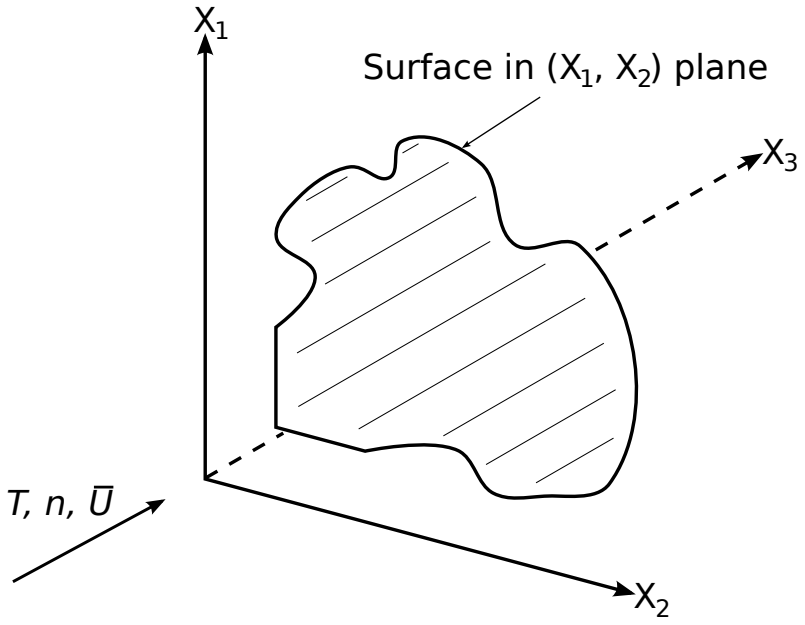

Figure B.1: Direction of the particle fluxes.

In order to derive the models, consider a gas flow with free molecular characteristics incident on an arbitrary surface section of area δA in the (X_1, X_2) plane as shown in figure B.1. The gas flow incident on the section is defined by an equilibrium velocity distribution function in the Maxwellian form with criteria: T_i, n_i, $\mathbf{U}_i = (U_1, U_2, U_3)$. Each particle has a velocity vector,

$$\overline{\mathbf{c}} = \overline{\mathbf{U}} + \overline{\mathbf{c}'}, \tag{B.1}$$

where $\overline{\mathbf{U}}$ is the free-stream velocity and $\overline{\mathbf{c}'}$ is the thermal velocity and thus,

$$f_{inc}\left(\overline{\mathbf{c}}\right) d\overline{\mathbf{c}} = \left(\frac{m}{2kT_{inc}\pi}\right)^{\frac{3}{2}} exp\left[-\frac{m}{2kT_{inc}}\left(\overline{\mathbf{c}} - \overline{\mathbf{U}_{inc}}\right)^2\right] d\overline{\mathbf{c}}, \tag{B.2}$$

where m, k and T_{inc} are the mass, Boltzmann constant and incident temperature, respectively. The incident flux of a particle property $\psi = \psi(\overline{\mathbf{c}})$ to the surface is given by,

$$\Gamma^{\psi}_{inc} = \int_{c_1=-\infty}^{\infty}\int_{c_2=-\infty}^{\infty}\int_{c_3=0}^{\infty} n_{inc} c_3 \psi\left(\overline{\mathbf{c}}\right) f_{inc}\left(\overline{\mathbf{c}}\right) d\overline{\mathbf{c}}, \tag{B.3}$$

where n_{inc} is the incident number density and if $\psi = \psi(c_3)$,

$$\Gamma^{\psi}_{inc} = n_{inc}\left(\frac{m}{2kT_{inc}\pi}\right)^{\frac{1}{2}} \int_{c_3'=-U_3}^{\infty}\left(U_3 + c_3'\right)\psi\left(U_3 + c_3'\right) exp\left(-\frac{mc_3'^2}{2kT_{inc}}\right) dc_3'. \tag{B.4}$$

Therefore, particles with velocities greater than -U_3 only reach the surface. The mass flux from the gas to the surface,

$$\phi_{inc} = mn_{inc}\left(\frac{m}{2kT_{inc}\pi}\right)^{\frac{1}{2}} \int_{-U_3}^{\infty}\left(U_3 + c_3'\right) exp\left(-\frac{mc_3'^2}{2kT_{inc}\pi}\right) dc_3', \tag{B.5}$$

is solved by considering the integral in two components, I_1 which accounts for

the U_3 term,

$$I_1 = \int_{-U_3}^{\infty} U_3 exp\left(-\frac{mc_3^{'2}}{2kT_{inc}}\right) dc_3^{'} \tag{B.6}$$

$$\Rightarrow\ I_1 = \int_{0}^{\infty} U_3 exp\left(-\frac{mc_3^{'2}}{2kT_{inc}}\right) dc_3^{'} + \int_{0}^{U_3} U_3 exp\left(-\frac{mc_3^{'2}}{2kT_{inc}}\right) dc_3^{'}. \tag{B.7}$$

And I_2 which accounts for the $c_3^{'}$ term as,

$$I_2 = \int_{-U_3}^{\infty} c_3^{'} exp\left(-\frac{mc_3^{'2}}{2kT_{inc}}\right) dc_3^{'} \tag{B.8}$$

$$\Rightarrow\ I_2 = \int_{0}^{\infty} c_3^{'} exp\left(-\frac{mc_3^{'2}}{2kT_{inc}}\right) dc_3^{'} + \int_{-U_3}^{0} c_3^{'} exp\left(-\frac{mc_3^{'2}}{2kT_{inc}}\right) dc_3^{'}. \tag{B.9}$$

By solving the first term of Equation B.7 using a standard integral and substituting

$$\eta^2 = \frac{mc_3^{'2}}{2kT_{inc}}, \tag{B.10}$$

equation B.7 becomes,

$$I_1 = U_3 \frac{1}{2}\left(\frac{2kT_{inc}\pi}{m}\right)^{\frac{1}{2}} + U_3 \int_{0}^{U_3\left(\frac{m}{2kT_{inc}}\right)^{\frac{1}{2}}} exp\left(-\eta^2\right)\left(\frac{2kT_{inc}}{m}\right)^{\frac{1}{2}} d\eta. \tag{B.11}$$

Using the speed ratio (ζ),

$$\zeta_3 \equiv \frac{U_3}{\sqrt{\frac{2kT_{inc}}{m}}}, \tag{B.12}$$

and applying the error function, equation B.11 becomes,

$$I_1 = \zeta_3 \frac{\sqrt{\pi}}{2} \frac{2kT_{inc}}{m} \left[1 + erf\left(\zeta_3\right)\right]. \tag{B.13}$$

Equation B.9 is solved using a standard integral for the first term and substituting

$$\iota = \frac{mc_3^2}{2kT_{inc}} \tag{B.14}$$

into the second term, thus,

$$I_2 = \frac{2kT_{inc}}{2m} + \frac{kT_{inc}}{m}\int_{\frac{mU_3^2}{2kT_{inc}}}^{0} exp\left(-\iota\right) d\iota = \frac{kT_{inc}}{m} exp\left(-\zeta_3^2\right). \tag{B.15}$$

Using equations B.13 and B.15 the mass flux from the gas to the surface becomes,

$$\phi_{inc} = \frac{1}{4} m n_{inc} \left(\frac{8kT_{inc}}{m\pi}\right)^{\frac{1}{2}} \left[exp\left(-\zeta_3^2\right) + \sqrt{\pi}\zeta_3 \left\{erf\left(\zeta_3\right) + 1\right\}\right], \tag{B.16}$$

with 2 bounds:

$$\phi_{inc} = \frac{1}{4} m n_{inc} < \mathbf{c}_{inc} > \tag{B.17}$$

and

$$\phi_i = \frac{1}{4} m n_{inc} \left(\frac{8kT_{inc}}{m\pi}\right)^{\frac{1}{2}} \sqrt{\pi} \frac{U_3}{\sqrt{\frac{2kT_{inc}}{m}}} 2 = m n_{inc} U_3 = \rho_{inc} U_3, \tag{B.18}$$

where ρ_{inc} is the incident gas density. Equation B.17 represents the mass flux when no free-stream velocity exits ($\zeta_3 = 0$) and the mass flux is caused by the thermal motion of the particles, and $< \mathbf{c}_{inc} >$ defines the average velocity of a particle at the free-stream (incident) temperature,

$$< \mathbf{c}_{inc} > = \sqrt{\frac{8kT_{inc}}{m\pi}}, \tag{B.19}$$

derived from the Maxwell-Boltzmann distribution. The upper bound, equation B.18, represents mass flux when the free-stream velocity is hypersonic ($\zeta_3 \rightarrow \infty$). By setting the energy flux (θ),

$$\theta = \frac{1}{2} m \mathbf{c}^2 = \frac{1}{2} m \left(c_1^2 + c_2^2 + c_3^2\right), \tag{B.20}$$

the incident heat transfer ($\dot{q}_{inc}$) is determined,

$$\dot{q}_{inc} = \Omega\Upsilon, \tag{B.21}$$

where,

$$\Omega = \frac{1}{2} m n_{inc} \left(\frac{m}{2kT_{inc}\pi} \right)^{\frac{3}{2}} and \tag{B.22}$$

$$\Upsilon = \left\{ \begin{array}{c} \int_{-\infty}^{\infty} c_1^2 exp\left(-\frac{mc_1'^2}{2kT_{inc}}\right) dc_1' \int_{-\infty}^{\infty} exp\left(-\frac{mc_2'^2}{2kT_{inc}}\right) dc_2' \int_0^{\infty} c_3 exp\left(-\frac{mc_3'^2}{2kT_{inc}}\right) dc_3' \\ + \int_{-\infty}^{\infty} exp\left(-\frac{mc_1'^2}{2kT_{inc}}\right) dc_1' \int_{-\infty}^{\infty} c_2^2 exp\left(-\frac{mc_2'^2}{2kT_{inc}}\right) dc_2' \int_0^{\infty} c_3 exp\left(-\frac{mc_3'^2}{2kT_{inc}}\right) dc_3' \\ + \int_{-\infty}^{\infty} exp\left(-\frac{mc_1'^2}{2kT_{inc}}\right) dc_1' \int_{-\infty}^{\infty} exp\left(-\frac{mc_2'^2}{2kT_{inc}}\right) dc_2' \int_0^{\infty} c_3^3 exp\left(-\frac{mc_3'^2}{2kT_{inc}}\right) dc_3' \end{array} \right\} \tag{B.23}$$

$$\Rightarrow \dot{q}_{inc} = \frac{\phi_{inc}}{m} \left\{ \frac{1}{2} m \mathbf{U}^2 + \frac{5}{2} kT_{inc} \right\} - \frac{1}{8} n_{inc} < \mathbf{c}_{inc} > kT_{inc} exp\left(-\zeta_3^2\right). \tag{B.24}$$

Equation B.24 has two bounds, the lower bound represents the heat transfer when no free-stream velocity exits ($\zeta_3 = 0$),

$$\dot{q}_{inc} = \frac{1}{4} n_{inc} < \mathbf{c}_{inc} > \left\{ \frac{1}{2} m \mathbf{U}^2 + 2kT_{inc} \right\}, \tag{B.25}$$

where the first term in the braces represents the kinetic energy of the free-steam flow and the second term the thermal energy. The upper bound represents the heat transfer when the free-stream velocity is hypersonic ($\zeta_3 \to \infty$),

$$\dot{q}_{inc} = \frac{\rho_{inc} U_3}{m} \left\{ \frac{1}{2} m \mathbf{U}^2 \right\} = \frac{1}{2} \rho_{inc} U_3 \mathbf{U}^2, \tag{B.26}$$

and the energy from the thermal motion is negligible relative to the kinetic energy.

Furthermore, the above derivations were for the incident fluxes to the surface but to determine the net fluxes of mass and energy the reflected fluxes have to be evaluated first. The reflected fluxes off the wall are assumed to originate from a hypothetical reservoir of gas beneath the surface of the wall. The reservoir of

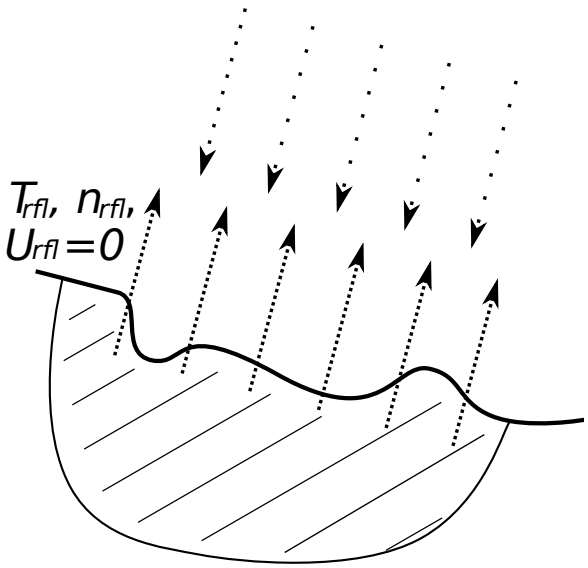

Figure B.2: Definition of incident and reflected surface fluxes.

gas is assumed to be in equilibrium and a representation of the reflected fluxes along with the incident fluxes are shown in figure B.2. The reflected portion is represented as

$$\Gamma^{\psi}_{rfl} = \int_{c_1=-\infty}^{\infty}\int_{c_2=-\infty}^{\infty}\int_{c_3=0}^{\infty} n_{rfl} c_3 \psi\left(\overline{\mathbf{c}}\right) f_{rfl}\left(\overline{\mathbf{c}}\right) d\overline{\mathbf{c}}, \tag{B.27}$$

and the reflected mass flux as,

$$\phi_{rfl} = \frac{1}{4} m n_{rfl} \left(\frac{8kT_{rfl}}{\pi m}\right)^{\frac{1}{2}}. \tag{B.28}$$

Equation B.28 is derived from equation B.16 with $(\zeta_3)_{rfl}$ equal to zero. In the case where no surface chemistry exists, the net mass flux to the surface is zero,

$$\phi_{net} = \phi_{rfl} - \phi_{inc} = 0, \tag{B.29}$$

therefore,

$$n_{rfl} = n_{inc}\left(\frac{T_{inc}}{T_{rfl}}\right)^{\frac{1}{2}}\left\{exp\left(-\zeta_3^2\right) + \sqrt{\pi}\zeta_3\left[1 + erf\left(\zeta_3\right)\right]\right\}, \tag{B.30}$$

where n_{rfl} is the number density of the hypothetical reservoir of gas beneath the surface of the wall. The reflected heat transfer is,

$$\dot{q}_{rfl} = 2kT_{rfl}\frac{\phi_{rfl}}{m}, \tag{B.31}$$

this is based on equation B.24 but with the incident terms replaced with the reflected ones and the speed ratio equal to zero as the reflected $\boldsymbol{U}$ is zero. Since the net mass flux to the surface is zero, equation B.31 becomes,

$$\dot{q}_{rfl} = 2kT_{rfl}\frac{\phi_{inc}}{m}. \tag{B.32}$$

Finally, the net heat transfer is determined as,

$$\dot{q}_{net} = \dot{q}_{inc} - \dot{q}_{rfl}, \tag{B.33}$$

where $\dot{q}_{inc}$ and $\dot{q}_{ref}$ are calculated from equations B.24 and B.32, respectively.